Advanced Myocontrol for Hand and Wrist Prostheses

handed in
MASTER'S THESIS

B.Eng. Thomas Eiband

born on the 28.11.1987
living in:
Eduard-Schmid-Str. 24
81541 Munich
Tel.: 0160 4833661

Human-centered Assistive Robotics
Technical University of Munich

Univ.-Prof. Dr.-Ing. Dongheui Lee

Supervisor:	Prof. Dongheui Lee, Ph.D.
	Markus Nowak, M.Sc., German Aerospace Center (DLR)
Start:	01.01.2017
Intermediate Report:	03.04.2017
Delivery:	15.07.2017

TECHNISCHE UNIVERSITÄT MÜNCHEN
LEHRSTUHL FÜR STEUERUNGS- UND REGELUNGSTECHNIK
UNIV.-PROF. DR.-ING./UNIV. TOKIO MARTIN BUSS

December 2, 2016

MASTER'S THESIS

for

Thomas Eiband
Student ID 03668558, Degree EI

Advanced Myocontrol for Hand and Wrist Prostheses

Problem description:

In the context of prosthetic control (myocontrol), the aim is to practically let the user (amputee) control a multi-DOF prosthetic hand/wrist. This requires a certain calibration/training process, which need to be shortened as much as possible to ease the daily use of the prosthesis.
Therefore, surface electromyography (sEMG) as well as force myography (FMG) sensors are applied and a strategy called LET (Linearly Enhanced Training) [1] is used. LET works by creating artificial data on top of the data gathered using the aforementioned sensors. This artificial data represents an approximation of combined DOF data based on single DOF data. The goal of this process is to shorten the training time and, at the same time, give the user a better control experience.
So far, multimodal sensing and LET only have worked to a certain extent. The main task is to try and enforce optimizations, techniques and tricks to improve the situation and finally have a working system, at least on intact subjects. If this works well, the system could be tested on amputees, too.

Tasks:

- literature analysis: machine learning, multimodal sensing for myocontrol, LET, user studies, statistical analysis
- getting confident with HW and SW and with the experimental procedure
- studying one or more strategies to improve the current system
- enforcing multimodal learning and optimized LET
- comparing the systems
- online experiment on intact subjects / on amputees

Bibliography:

[1] Markus Nowak and Claudio Castellini. The let procedure for prosthetic myocontrol: Towards multi-dof control using single-dof activations. *PloS one*, 11(9):e0161678, 2016.

Supervisor:	M.Sc. Markus Nowak, Ph.D. Claudio Castellini, Prof. Dongheui Lee
Start:	01.01.2017
Intermediate Report:	03.04.2017
Delivery:	14.07.2017

(D. Lee)
Univ.-Professor

Abstract

Myocontrol is the use of a human machine interface based on muscle signals in order to control a robotic or prosthetic device. A challenging problem in research is the simultaneous and proportional (s/p) control of multiple degrees of freedom (DOF). Besides the common sensing technique of surface electromyography (sEMG), force myography (FMG) is additionally enforced to improve the control experience. Machine learning approaches are employed to map the input of different sensor modalities onto continuous control signals of a prostheses. Throughout this work, four experiments have been conducted with the goal to reduce the training time and to improve the control experience of such devices.

In the first experiment we showed that for a fusion of both signal modalities the offline performance is invariant for different sensor placements on the forearm. The second experiment evaluated the online performance using different machine learning approaches where either one or both signal modalities were employed. The best results were achieved with a combination of both signal types and with FMG only. As part of this work, an existing method called linearly enhanced training (LET) is adapted to the multi-modal sensory input. This method creates artificial training data for combinations of defined hand and wrist actions and dismisses their explicit recording as training data, which usually cannot be achieved by amputees. It follows that the training time is significantly reduced. In the related experiment, data has been gathered from 10 healthy subjects in order to find a generalized set of parameters for LET. Once determined, these parameters can be the basis for LET for new users.

In the last experiment, the set of generalized parameters has been used for nine healthy subjects to evaluate the performance of the approach involving LET data. We showed that with LET the subjects performed equally well compared to the approach which required the execution of all combined activations during training time. This qualifies LET as a valid extension to existing control methods as the training time is drastically reduced and no combined activations need to be executed. The goal is to use the same set of parameters and algorithm for amputees, which may not be able to produce combined activations during training time.

Contents

Chapter 1

Introduction

There are various types of limb amputations at different severity levels. To recover the lost functionality, a variety of technical systems is available. Several of these systems are not naturally accepted by an affected person when it comes to an evaluation of the benefit [ØLF+12]. A fraction of amputees even prefers to live with their deficiency instead of using a prostheses, as they regard the offered system as inconvenient and less useful [PVdDVL+99] [BC08] [BC07b]. Causes can be the unreliability, the weight or the appearance [BC07a].

This project focuses on the field of upper limb prosthetics, where a number of technical systems is available. These systems try to substitute lost functionality of the forearm, the wrist and the hand. Technically simple but effective solutions are body-powered prostheses, where the shoulder movement is used to actuate a gripper via a cable [MHH86] [ZO14]. Body-powered systems are still widely used and accepted [ØLF+12]. A big advantage is the force feedback, as the grip force is fed back via the cable to the shoulder. A drawback is the availability of only one continuous Degree of Freedom (DOF), which is usually the gripper state.

However, daily live situations may require more dexterous control opportunities where the simultaneous and proportional (s/p) control of multiple DOFs is required. This can be achieved by myocontrol, in which the residual muscle activity in a limb is sensed to control a prosthetic system according to the user's intent. The sensing is based on biosignals, whereas myoelectric signals are most commonly used as signal source in modern prostheses. This sensing technique is called electromyography (EMG) and if the signals are only sensed non-invasive on the surface of the skin, it is termed surface electromyography (sEMG). In addition to that, it is possible to sense another biosignal at the residual limb, which is force-myography (FMG). Hereby, the change in shape of a muscle under contraction is measured through pressure sensors on top of the skin.

1.1 Problem Statement

To bring prosthetic systems and their human machine interfaces from research institutes closer to the daily life application with amputees, a number of problems still need to be solved, e.g. the socket design, the weight, the control capabilities and other inconvenient properties of such systems. In this work, two major problems of myocontrolled hand and wrist prostheses are targeted, which are the shortening of the training phase and an improvement of the control experience.
For a dexterous control system, a certain training phase is required before the use of the prosthesis. This training phase need to be as short as possible in order to allow a frequent usage. Otherwise, the amputee could permanently reject the prosthesis because of an inconvenient daily training procedure. Therefore, techniques need to be employed which reduces the amount of training time and simplify the training phase. Amputees have only a limited controllability of their residual muscles, which makes it hard to simultaneously contract muscles in charge of different DOF. Especially this restriction needs to be bypassed as good as possible by the technical system.
The second targeted problem is to make the behavior of a s/p controlled system as intuitive as possible. Less physical and less mental demand should be required during usage. The independent activation of different degrees of freedom (DOFs) should be possible at the desired level. This accounts for single DOFs as well as for combinations of them. Hereby, a prosthesis should provide a set of DOFs which are purposeful in daily life. These are actions such as the forearm rotation, namely wrist pronation and supination, wrist flexion and extension and at least one or more different types of grasp. Further actions could be the wrist abduction and adduction or even single finger movements.
This work will extend techniques which already use two different biosignals, namely surface electromyography (sEMG) and force myography (FMG), which will be explained in the following section.

1.2 Related Work

The term myocontrol is mostly related to EMG controlled systems, using either sEMG or implanted electrodes sensing the electric field of the muscle fibers innervated by a motor neuron. This electric field is strongest in a region where the concentration of nerve fibers innervating a muscle is high. As an example, a good region for sensing sEMG signals is above the muscle belly, which can be found best at maximum muscle contraction.
Applicable commercial myoelectric systems became available in the 80's, using EMG signals to control prosthetic devices [PS85] [SP88]. The control scheme was the classification of intended actions, for instance using artificial neural networks (ANN) in [HPS93]. Evans et. al. already focused on proportional control of selected DOF in the 80's [EPPS84].

As s/p control is a dexterous problem in inferring the human intend, there are still some reasons why it is not the standard solution for amputees. Causes can be an unstable, unreliable or non-intuitive control output or the learning phase for these systems. By contrast, classification based control of a prosthesis is a widespread technique, accepted by many amputees. The research in this field has not stopped until today.
In this work, s/p control of multiple DOFs is targeted. In the following, some works are introduced which directly focus on s/p control of upper limb prosthesis.
In [NHJ+09], four signal features in time-domain were extracted from the sEMG signals. These were used to build pairs with the measured forces at different wrist contractions to train a multilayer perceptron (MLP).
The authors of [NTIS15] propose the use of a Gaussian Process latent variable model, which learns the dynamical model between finger postures and the EMG data. The model is capable of predicting the continuous movements of a five-finger hand model with 69 DOFs.
In Tab 1.1, a summary of papers from the latest research interests about sEMG based myocontrol can be found.
In contrast, force-myography is the sensing of the force which a muscle belly exerts on a sensor at different contraction levels. The sensor is pressed against the muscle belly and its force sensing axis is oriented perpendicular to the muscle tension axis. Despite the fact that force sensors are used to measure the muscle activity, the measurement is strongly influenced by the characteristics of the skin and the sensors head geometry and contact area. Hence, some authors talk about sensing a pressure rather than a force. For clearance, this sensed force is not the muscular force or any joint force exerted by such muscle.
Table 1.2 summarizes some works, where FMG based myocontrol is addressed, using different sensor types such as strain gauge sensors (SGS), optical fibre specklegram sensors or force sensing resistors (FSR).
In [CCM+16], a bracelet was equipped with 8 force sensing resistors (FSRs) which are evenly spaced on the bracelets inner surface. A wearable Bluetooth device is used to transmit the signals to a computer. A classification algorithm infers the different gestures.
An approach of massive use of FMG sensors is shown in [RSE16], where an array of 126 pressure sensors is employed. A significant difference in the classification error of gestures over different sensor selections could be observed. The classification accuracy could be improved through a sensor selection pattern, consisting of two areas around the forearm compared to a configuration, where the whole sensor array is used.
In a relaxed hand and wrist state, FMG signals are more sensitive to changes in the arm posture than EMG signals. Rasouli et. al. [RCCK16] simply call this the limb position effect, when they investigated the influence of the arm pose on their classification results. They used a 16×8 force taxels array attached to the forearm by a blood pressure measurement cuff. This cuff applied a permanent pressure on

Table 1.1: Overview of current research interests based on sEMG. * Data from the second version of the *NinaPro* database [AGK+15].

Ref.	Sensors	Trained Actions	Methods	Subjects
[PSL16]	8 sEMG	wrist fle./ ext., pro./ sup.	ensemble learning (arm pos. changes + LR), p control	10 healthy
[EYkA16]	1 pair of sEMG	elbow fle./ ext.	2 step approach: 1st step: LDA, 2nd step: TDANN, p control	1 healthy
[EP09]	8 sEMG	wrist fle./ ext., radial/ ulnar deviation, pro./ sup.	NMF, s/p control	12 healthy
[GKAM15]	12 sEMG	wrist sup./ pro., fle./ ext., radial/ ulnar deviation	GRNN, s/p control	40 healthy*
[KVN15]	12 sEMG	hand kinematics (not further specified)	comparing RR with KRR	40 healthy*
[MTM15]	8 sEMG	hand open/ close, wrist pro./ sup.	NMF, s/p control	10 healthy
[JRV+14]	16 sEMG	wrist flex./ ext., pro./ sup.	NMF, s/p control	7 healthy, 7 amputees
[JVR+14]	16 sEMG	wrist fle./ ext., pro./ sup.	comparison of NMF, LR and ANN, s/p control	9 healthy
[NC15]	10 sEMG	wrist fle./ext, pro., power grasp	RR-RFF with LET, offline evaluation	6 healthy
[NC16]	10 sEMG	thumb opposition, thumb fle., index fle., little finger fle.	RR-RFF with LET, s/p control	10 healthy
[NAC16]	*Thalmic Labs' Myo*-bracelet (8 sEMG)	power grasp, wrist pro., fle./ext	RR-RFF with LET, s/p control	16 healthy, 1 amputee

Table 1.2: Overview of current research interests based on FMG.

Ref.	Sensors	Trained Actions	Methods	Subjects
[SM16]	16 FSR	wrist pron./ sup., flex./ ext., radial/ ulnar deviation	comparing SVR (with RBF kernel) and ANN, offline eval.	5 Healthy
[FJM+16]	7 SGS placed on wrist	16 grasp gestures	comparing LDA and SVM for gesture classification, offline eval.	3 Healthy
[FWS+15]	1 optical fiber speck-legram sensor	indiv. flexion of all fingers	ANN with backpropagation, offline eval.	3 Healthy
[YMGY16]	3 FSR	wrist flex./ ext., finger flex./ ext. (palmar grasp)	MLP as supervised classifier, real-time classification	3 Healthy
[RGL+15]	16x8 tactile sensors array	hand open/ closed, pinch grasp, wrist flex./ ext.	ELM and OSELM allowing different arm postures, real-time classification	2 Healthy
[RSE16]	array of 126 FSR	rest, wrist flex./ext., pron./sup., power grip, pinch grip, hand open	informed channel reduction, real-time LDA classification in different arm postures	10 Healthy
[RCCK16]	16x8 force taxel array & IMU	wrist flex./ext., pron./sup., open hand, power/pinch grip, rest	ANN (2 layer-FFNN (feed-forward neural network)) as position aware ensemble classifier.	3 Healthy
[KJM16]	8 FSR	grasps: power, tripod pinch, index pinch	SVR with RBF-kernel, s/p control of thumb, middle and index finger	10 Healthy

the sensor array which was tried to be kept constant over the different arm positions. They use an ANN with a position aware ensemble classifier to predict the hand state. Hereby, they take the arm position obtained by an IMU into account. They reached a prediction accuracy of $30.9 \pm 4.1\%$ when the classifier was trained at one position and tested with data from other positions. An accuracy of $89.4 \pm 4.2\%$ was achieved when they used the position aware classifier. In this example, the authors focused on different positions of an arm with extended elbow and different upper arm angles relative to the shoulder. This completely neglects the effect of elbow angle changes, which could have a similar strong effect on the results. Another example is found in [RSE16], where an array of FSRs is used to classify hand postures under varying arm positions as they occur in daily life. Again, the prediction performance drops significantly when the system is required to work under daily live conditions.

These are two causes for the influence of the arm position and pose on the prediction results. First, looking at the musculoskeletal system of the elbow joint [SSS11], the forearm circumference at its proximal end is influenced by a number of muscles related to the elbow flexion. *Musculus* (M.) *biceps brachii* and *M. brachialis* contract and pull on the tendons *Tuberositas Radii* and *Tuberositas Ulnae* respectively in order to flex the elbow or support the forearm rotation. Sensors located in this region will be actuated by the lifted skin and the resulting rise in forearm circumference. At the same time, skin accumulates on the upside of the forearm which further influences the measurements.

Second, looking at the prosthesis or sensing setup hardware weight, the sensors and the arm socket change their weight force vector depending on the arm pose. Therefore, the normal forces onto the sensors changes. An even bigger effect is involved when the user lifts a payload with his or her prostheses and therefore changes the load between prosthesis socket and arm.

Very few references can be found in the latest research interests of combined approaches for sEMG and FMG. Table 1.3 summarizes some approaches, which also includes the work at German Aerospace Center (DLR) about a first assessment and a combination of both signal modalities. Sanford et. al. [SPP15] only uses one sEMG electrode and places a FSR on top of the electrode as a link to the socket. The FSR is then intended to increase the reliability of the prostheses when a socket shift occurs. Yetkin [Y+16] examined different setups for sEMG and FMG based intent classification but gives just an outlook of future sensor fusion possibilities. One interesting fact about the approach is that if the user comes with one healthy hand, it is used with a tracking glove to create the ground truth for the missing hand on which arm the training data is recorded.

At DLR, a prototype of a multi-modal sensing device has been developed with the ability to sense both sEMG and FMG signals from the muscles of the forearm [CRVC16]. The sensor data is gathered at 100 Hz and transmitted to a computer using a Bluetooth connection.

Table 1.3: Overview of current research interests of fusing EMG and FMG.

Ref.	Sensors	Trained Actions	Methods	Subjects
[SPP15]	1 FSR on top of 1 sEMG	wrist extension	classification with MLP, simulating socket shift	1 Healthy
[Y+16]	different setups	different setups	tracking glove on contra-lateral hand for ground truth, NN classification	1 Healthy, 1 with congenital hand defect
[CRVC16]	10 FSR, 10 sEMG	rest, wrist flex./ext., pron./sup., power grasp	data acquisition and offline analysis	10 Healthy
[RR16]	10 FSR, 10 sEMG	rest, wrist flex./ext., pron./sup., power grasp	RR-RFF in different configurations	12 Healthy

The sEMG and FMG signals recorded with this hardware has already been analyzed and compared in [CRVC16]. A comparison of the online performance of each sensor modality using 12 healthy subjects has been done in [RR16].

1.3 Machine Learning in Myocontrol

The main goal of myocontrol is to find a mapping between the biosignals of an intended action and its respective ground truth. This mapping can be achieved through classification for discrete state predictions or through regression for continuous state predictions. Beside the discrete or continuous domain, it needs to be distinguished between single and simultaneous control of the available DOFs.

1.3.1 Classification

As summarized in the current research interests in section 1.2, classification approaches are quite popular as the classification error can be driven to almost zero if the experiment is designed accordingly, e.g. restrict the arm movements, use a small number of classes or a high number of training repetitions. But also in daily life applications, classification is the main technique for commercially available myoelectric upper limb prosthesis.
For classification, different artificial neural networks (ANN) are employed, mainly multi-layer perceptrons (MLPs) as feed-forward NNs as well as back-propagation ANNs. Other popular classification algorithms in myocontrol are linear discriminant analysis (LDA) and support vector machines (SVM).

1.3.2 Regression

Regression is a method to find a continuous mapping between input signals and desired output signals. This is required if the DOFs of a prosthesis need to be controlled proportionally to the intended movements of its user. This mapping between the user's biosignals and the ground truth of the human joint state can be modeled in a linear or non-linear manner. Defining the ground truth is an issue in case of an amputee with a missing limb. For people with sound limbs, it can be either the joint angle or the exerted torque on this joint. For amputees, this kind of ground truth is not available. Nevertheless, an amputee might be still able to control a small set of his or her muscles at different levels of contraction (to control different forces).
In the training phase, a certain level of contraction might be difficult to hold. The amputee may not have any sensorimotor capability to execute a small level of contraction, as there is neither visual nor a clear proprioceptive feedback available. It is simpler to hold the maximum contraction during the data acquisition at each of the desired activations. The rest position of the targeted joint needs to be recorded additionally, where no muscular activity should take place. Using this training data allows the shaping of a regression model which delivers a continuous output also for the intermediate states, where no training took place.
With a high number of sensors and a number of available prosthesis DOFs, the method is basically a multiple linear or non-linear regression. In the case of biosignals, non-linear methods enjoy the capability of more dexterous mappings between sensors signals and the desired output.
As the sEMG and FMG sensors are mostly related to the muscular activity, a relation between signal and muscular contraction force is most presumable. Despite this relation, these sensors react also on changes in placement, when the skin slides above the muscles caused by joint angle changes of other muscles. An example is the elbow flexion, which affects the spacial arrangement between the skin and muscles in the forearm.
Most popular regression algorithms in myocontrol are still linear regression (LR), ridge regression (RR), generalized linear regression (GLR), non-negative matrix factorization (NMF) and support vector regression (SVR) with radial basis function (RBF) kernels. Further, different kinds of NNs are used, e.g generalized regression NNs (GRNN) and time delayed NNs (TDNN).
From this huge variety of regression algorithms, one has shown its advantages in myocontrol in a number of studies [GM11], [GBSG+14],[CR14], which is Ridge Regression with Random Fourier Features (RR-RFF).

Ridge Regression with Random Fourier Features

This algorithm belongs to the class of generalized linear regression. The regression model is non-linear but linear in its coefficients. Therefore, the model coefficients

$\boldsymbol{W}$, also called weights, can be calculated through a least squares approach as it is known from linear regression.
A multiple linear regression model is given by

$$\boldsymbol{Y} = \boldsymbol{X}\boldsymbol{W} + \boldsymbol{t} \tag{1.1}$$

where $\boldsymbol{X} \in \mathbb{R}^{N_s \times d}$ is the design matrix with N_s samples and d input dimensions.. The given target values $\boldsymbol{Y} \in \mathbb{R}^{N_s \times N_{\text{out}}}$ define the ground truth related to each observation, where N_{out} is the number of output dimensions, e.g. one for each DOF in a prostheses. The parameter $\boldsymbol{t}$ is used for the y-intercepts of the regression lines, which can be transferred to the matrices

$$\tilde{\boldsymbol{X}} = \begin{bmatrix} \boldsymbol{X} & \mathbf{1} \end{bmatrix} \qquad \text{and} \qquad \tilde{\boldsymbol{W}} = \begin{bmatrix} \boldsymbol{W} \\ \boldsymbol{t} \end{bmatrix} \tag{1.2}$$

enabling a constant term as a column of ones. As a result, the model can be rewritten as

$$\boldsymbol{Y} = \tilde{\boldsymbol{X}}\tilde{\boldsymbol{W}}. \tag{1.3}$$

Further, it is assumed that the calculations are based on a model without a constant term and a y-intercept parameter $\boldsymbol{t}$, as it is no longer required in this algorithm. Solving the least squares problem of

$$\boldsymbol{W}^* = \underset{W}{argmin} \left\| \boldsymbol{X}\boldsymbol{W} - \boldsymbol{Y} \right\|_2^2 \tag{1.4}$$

results in the optimal closed form solution

$$\boldsymbol{W}^* = (\boldsymbol{X}^{\boldsymbol{T}}\boldsymbol{X})^{-1}\boldsymbol{X}^{\boldsymbol{T}}\boldsymbol{Y}. \tag{1.5}$$

Potential instability in the least squares estimator and problems of over-fitting can be reduced by adding a small constant value λ to the diagonal entries of the matrix $\boldsymbol{X}^T\boldsymbol{X}$ before taking its inverse. This results in the ridge regression estimator (1.6), where the matrix $\boldsymbol{I}$ is the identity matrix with the same dimensionality as $\boldsymbol{X}^T\boldsymbol{X}$. This extension to the least squares problem is called regularization, as the model coefficients are constrained in their size and is further known as *Tikhonov Regularization.*

$$\boldsymbol{W}^*_{\text{ridge}} = (\boldsymbol{X}^{\boldsymbol{T}}\boldsymbol{X} + \lambda\boldsymbol{I})^{-1}\boldsymbol{X}^{\boldsymbol{T}}\boldsymbol{Y} \tag{1.6}$$

Now, as a non-linear model is required, extending the linear model to a generalized linear model is done by exchanging the design matrix $\boldsymbol{X}$ with a non-linear mapping function, which projects each training sample into a higher dimensional space. This space is often referred to as feature space in machine learning applications. The mapping function is defined as

$$\varphi(\boldsymbol{X}) = cos(\boldsymbol{X}\Omega^T + \mathbf{1}_{N_s}\boldsymbol{\beta}^T). \tag{1.7}$$

In this regression algorithm, random Fourier features are used for the feature space mapping, which are constructed through randomly drawn cosine functions in (1.7). One property of this algorithm is that no parameter for the y-intercept is required. Through the linear combination of the basis functions, an arbitrary shift in the y-axis is achievable.
To obtain random properties, a parameter $\boldsymbol{\Omega}_1$ is initially drawn from a normal distribution in

$$\boldsymbol{\Omega}_1 \sim \mathcal{N}(0,1) \in \mathbb{R}^{D \times d}, \tag{1.8}$$

and determines the frequencies of the cosine functions. It is later scaled by a hyper-parameter σ to optimize the regression model.
The dimensions of this parameter $\boldsymbol{\Omega}_1$ are $D \times d$, where D denotes the feature space dimensionality and d denotes the number of signals in the input space. The feature space dimensionality can be found by a cross-validation where the feature space dimensions are increased in every iteration until the decrease in the model error is small enough.
A second parameter $\boldsymbol{\beta}$ is drawn from a uniform distribution

$$\boldsymbol{\beta} \sim \mathcal{U}(-\pi, \pi) \in \mathbb{R}^{D} \tag{1.9}$$

to determine the phase shift of a cosine function between $-\pi$ and π.
The random parameter $\boldsymbol{\Omega}_1$ can be scaled by the hyper-parameter σ to obtain a scaled parameter given by

$$\boldsymbol{\Omega} = \sigma\, \boldsymbol{\Omega_1}. \tag{1.10}$$

To fit the model, a hyper-parameter search is conducted based on the root mean squared error (RMSE). The best parameter can be found by cross-validation of each model in the parameter search.
These random properties of the cosine functions allow a good approximation of different features of the training samples as the obtained cosine functions differ in frequency and phase shift.
In fact, there is a second hyper-parameter λ, which is the regularization parameter of the linear model coefficients. To further improve the model, this parameter could be also found in a parameter search. Nevertheless, adding a second hyper-parameter into the parameter search ends up in a computationally expensive grid search.
It has been shown that the hyper-parameter σ has a larger influence on the model properties than λ, which is best used at a standard value of 1.
Now, the model coefficients $\boldsymbol{W}$ are obtained by

$$\boldsymbol{W}^* = (\varphi(\boldsymbol{X})^T)\varphi(\boldsymbol{X}) + \lambda \boldsymbol{I}_D)^{-1}(\varphi(\boldsymbol{X})^T \boldsymbol{Y}), \tag{1.11}$$

where $\boldsymbol{I}_D$ is the square identity matrix with the dimensionality of the feature space. It is required to have a feature space dimensionality higher than the number of columns in $\boldsymbol{X}$ to enable a projection from a lower into a higher dimensional space.

To obtain a prediction $\widehat{\boldsymbol{y}}$ of the trained model, employ

$$\widehat{\boldsymbol{y}} = \varphi(\boldsymbol{x})\, \boldsymbol{W}^* \tag{1.12}$$

with a given test sample $\boldsymbol{x}$, where $\varphi(\boldsymbol{x})$ is again the mapping function between input and feature space.
One property of this algorithm is that the feature space dimensionality can be kept constant with a growing number of samples, which keeps the learning effort limited. Since a closed form solution for the model coefficients exists, an efficient computation is possible. The prediction is then just a linear combination of cosine functions, which can be efficiently calculated by modern computers.
Summarizing, the implementation is comparable to a simple linear regression algorithm with the addition of drawing two parameters from random distributions and introducing a simple mapping function $\varphi(\boldsymbol{x})$. The ease of implementation and small computational requirements are the main advantages in using this algorithm. Another advantageous feature is the possibility of using incremental learning within this framework [GM11], which is not exploited throughout this thesis.

1.4 Contributions

This work contributes to the field of myocontrol, where the simultaneous and proportional (s/p) control of multiple DOF is achieved. The fusion of the signal modalities sEMG and FMG is exploited with a number of up to 10 sensors per modality, which is novel in prosthetic control algorithms. The primary objective of this thesis is to test the hypothesis that:

1. the prediction performance is invariant from different sensor placements of sEMG and FMG sensors on a defined region of the forearm.

2. a combination of both signal modalities leads to a better prediction performance compared to the use of only one signal modality.

3. a method to enhance training data can substitute real data from multiple-DOF hand and wrist actions, based on data from single-DOF actions only.

4. this method achieves the same performance compared to the usage of real multiple-DOF action data.

The first part of the thesis consists of a literature review of myocontrol approaches based on either sEMG, FMG or combined modalities.
Chapter 2 focuses on the evaluation of different sensor placements and the assessment of methods using either single or combined signal modalities. The different regression based machine learning methods are introduced here, which are used in the conducted experiments. In a first experiment, an offline analysis evaluates

the sensor placement and the performance of the employed machine learning approaches In the second online experiment, different approaches involving single and multi-modal sensor input are compared in a goal reaching task.
In Chapter 3, further properties of the signal modalities are outlined and the control schemes of healthy subjects and amputees are discussed. Since data is available from the previous experiment in this work, a probabilistic sensor fusion approach could be parameterized. A single user study enables a preliminary assessment of this approach also in comparison to a purely regression based approach from the previous chapter.
Chapter 4 describes the strategy of artificially enhancing training data for multiple-DOF hand and wrist actions. The underlying method is applied for the first time to multi-modal sensor data. This technique drastically reduces the training time as the training of multiple-DOF hand and wrist actions becomes unnecessary. In section 4.3, the design of a novel test setup is described. It emulates some properties of a transradial amputation at healthy subjects and contributes to the following two applications: First, training data from healthy subjects can be recorded and analyzed in order to transfer the knowledge to amputees. Second, the test setup can be used for online performance evaluations where novel analyses become possible due to the recorded signals. Beside the sEMG and FMG signals, these are upper arm and forearm pose, elbow angle as well as exerted forces and torques at the wrist and hand. Section 4.4 and 4.5 describe the experiments for the data acquisition and online performance evaluation.
It should be noted that testing and assessing novel methods on amputee subjects underlies limitations. Throughout this thesis, no amputees participated in the experiments. One problem is the limited availability of amputee subjects when conducting experiments which require a high number of participants in order to generalize parameters. The data acquisition experiment for the method of training data enhancement cannot be carried out with amputees because a reliable ground truth is necessary where the torques of an intact limb need to be measured.
Chapter 5 presents a summary of the thesis where the results are discussed. Chapter 6 lists the conclusions drawn from this work and outlines future work and related research recommendations.

Chapter 2

Multi-Modal Machine Learning

This chapter introduces the system used for the data acquisition and state prediction and describes the applied machine learning approaches. A comparison of the signal characteristics between sEMG and FMG has already be done in [CRVC16]. A first online performance comparison using the different sensor signals has been conducted in [RR16].
In the following experiments, the effect of different placements of the available sensors on the forearm is examined. It is further explored how the combination of both sensor types improves the overall prediction performance compared to just one sensor type. Hereby, the same number of sensors for each approach is employed, which is different to [RR16]. This was done to enable a fair comparison of different approaches using the same amount of information.
The following two hypotheses are made and examined by experimental evaluations:

1. Different placements of sEMG and FMG sensors on a selected area of the subjects forearm does not significantly influence the performance of the prediction.

2. The online prediction performance of a combination of sEMG and FMG sensors is significantly better than using the sensors of one modality only.

Section 2.1 introduces the different machine learning approaches and the hardware. In section 2.2, an offline experiment is conducted, evaluating different sensor placements an machine learning approaches. The online performance comparison is described in section 2.3. A conclusion is made, summarizing both experimental results in section 2.4.

2.1 Materials and Methods

As outlined in the introduction, it is advantageous to employ a non-linear model for myocontrol to transform the biosignals into meaningful control signals for a

prosthetic device. The method of choice throughout this work is Ridge Regression with Random Fourier Features (RR-RFF) with the capability to provide non-linear regression models at low computational costs.
Throughout the following experiments, the characteristics of the different sensor signals, namely sEMG and FMG are outlined. Four types of learning machines were used, which all use the RR-RFF algorithm with different input spaces and configurations. The approaches are denoted in italics as followed and can be found in Fig. 2.1.

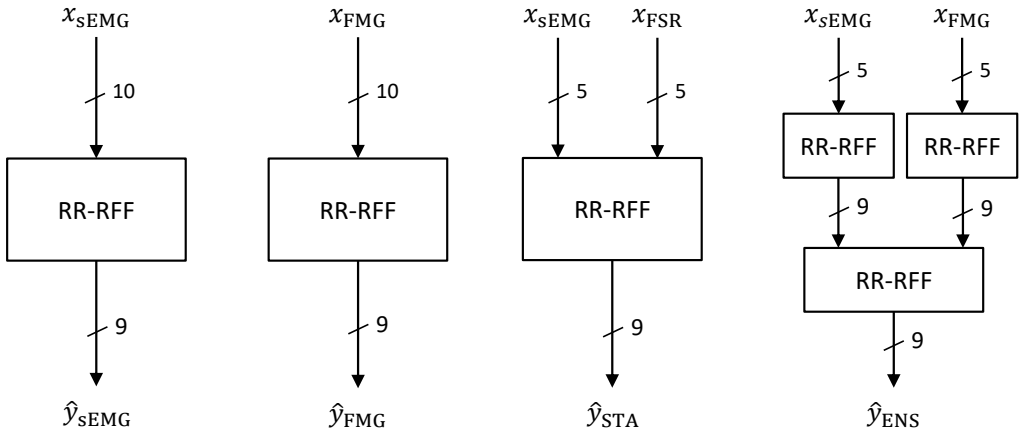

Figure 2.1: Machine learning approaches throughout the experiments. From left to right: *sEMG, FMG, STA, ENS*. Numbers next to signal flow arrows display their dimensionality.

sEMG: Using the surface electro-myogram of a subject as the input into a RR-RFF learning machine. A number of 10 sEMG sensors is employed, distributed over the subject's forearm on two bracelets.
FMG: Using the force-myogram, which is a physical property of the muscle contraction level, as input of a RR-RFF learning machine. A number of 10 FMG sensors is used, placed in the same constellation as the sEMG sensors
STA: Stacking sensor signals of five sEMG and five FMG sensors in the same input space of a RR-RFF learning machine. A feature of this methods is that hyper-parameters still can be chosen independently for each sensor, which enables enhanced model tuning possibilities.
ENS: An ensemble learning configuration, where the output of two low-level learning machines are used as input of a high-level LM. The two low-level machines are configured as the approaches *sEMG* and *FMG* but each using five of their related sensor channels as input. These low-level LM provide their stacked output as input into a high-level learning machine, which is again of type RR-RFF. This enables the use and optimization of different hyper-parameters for each of the three machine learning components. The described configuration has been introduced in [RR16]. A feature of this algorithm is, that the training set of both low-level LM is split in

a leave-one-repetition-out manner into a training and test set. Each of the training sets is used to train the LM and each of the test sets is used to generate a set of low-level predictions. This prediction set is then used as the training set of the high-level LM. The high-level machine learns the variations, or in other words, the prediction errors of the low-level LM in order to fuse both sensor modalities.
All approaches use the same input space dimensionality of 10 sensors in order to have a fair method comparison assuming that every approach is provided with the same amount of information coming from the selected sensors. Figure 2.1 outlines the signal flow between sensors x and prediction $\widehat{y}$ for each approach and denotes the number of signal channels next to the signal flow arrows.

2.1.1 System Overview

The data acquisition system consists of 20 sensors, which are fitted on two Velcro straps, depicted in Fig. 2.2. These straps are used as bracelets to fit the sensors on the subject's forearm. One sensor type is an Otto Bock sEMG sensor with internal filtering electronics, supplying an amplified, rectified and band-pass filtered sEMG signal. The other sensor type is a force sensing resistor (FSR) with simple voltage divider electronics to sense the FMG signals. The FSR module is embedded in a flexible 3-D printed housing. The housing has a ball shaped pressure point using the flexible housing as a mechanical spring onto the sensor plate of the FSR.
In this setup, both sensor types are mixed on the same bracelet, which is different to [CRVC16]. The original holders for the sEMG sensors were to flat such that the contact with the skin was not ensured when a sEMG sensor was placed next to a FSR sensor. These holders were adapted and again 3-D printed, such that the height of both sensor types matches. In this case, the pressure on both sensors surfaces should be approximately equal and the effect of sensor liftoff is minimized.
The analogue sensor signals are acquired by the analogue digital converter (ADC) of a micro-controller and are then transmitted over a wireless Bluetooth connection to a Windows computer. See the block diagram in Fig. 2.3 for more details. The C# application *interactiveMyocontrol* does all the data pre-processing, including an offset removal (x_{offset}) and inversion of the FMG signals. This step in the software is not mandatory for the machine learning part as the algorithm would adapt to the signal characteristics but is advantageous for display purposes and signal analysis. The inversion and offset removal is done as the FMG signal is defined by a voltage divider circuit, where zero force is related to a high signal and vice versa. The electrical circuit can be found in [CRVC16].
A first order low-pass Butterworth is applied on each of the signal types. The filtered signals are fed into the machine learning algorithm for the training data acquisition as well as for the online prediction. The output of the learning machine is fed into a limiter as predictions above or below the system limits are not desired, which accounts for simulation as well as for real hardware purposes. After limiting, the output is again filtered by a first order Butterworth to enable a smooth prediction,

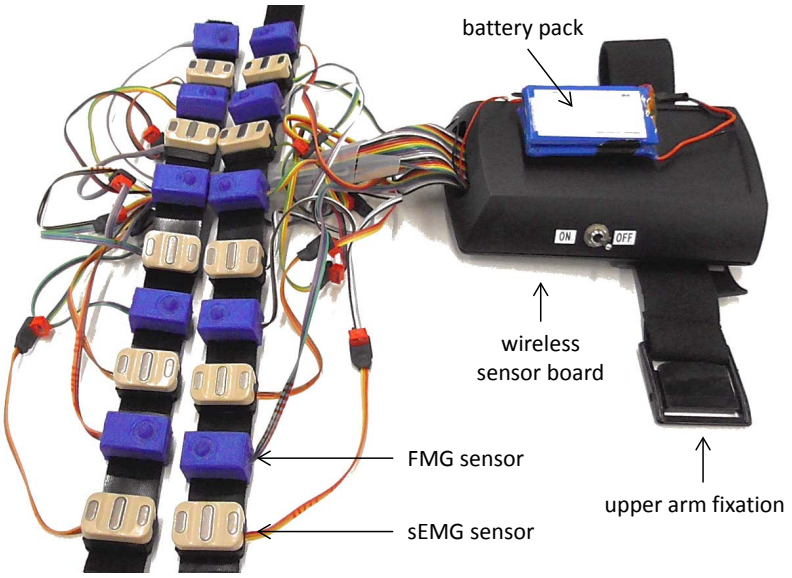

Figure 2.2: Data acquisition hardware.

and then sent to a visual hand model by an UDP connection in this case. Controlling a prosthetic hand is further possible over a Bluetooth connection. The software has the capability to control any number of DOF regarding the ML algorithm and the data processing and is usually configured to nine DOF. These are the five individual finger flexions, the thumb rotation, the wrist flexion/extension, the wrist pronation/supination and the wrist adduction and abduction. Throughout the following experiments, only three DOF are used.

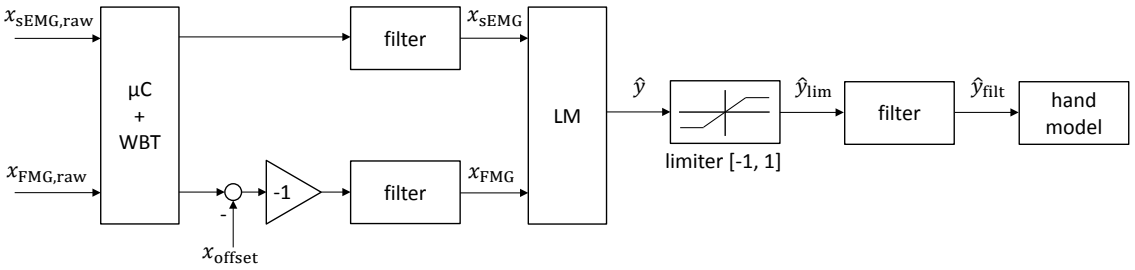

Figure 2.3: Block diagram of the data acquisition and online control system with micro-controller (μC), wireless bluetooth (WBT) unit and learning machine (LM).

2.1.2 Signal Filtering

Both signal types are filtered with a 1st order Butterworth low pass with a cut-off frequency of 1 Hz. This parameters has shown good filtering results for an online monitoring of the sensor signals, to collect the training data and for usage during

the prediction. A preliminary offline analysis has shown that the effect of filtering on the training data is negligible in the model prediction error.

The raw FMG signals are first filtered in the software *interactiveMyocontrol*, the sEMG signals are already pre-processed in the hardware of the sensors, manufactured by *OttoBock*. A band-pass filtering and a rectification is applied here. The resulting sEMG signal is then again filtered in the software by the previously described Butterworth filter.

The prediction filter after the LM uses the same filter characteristics and enables a smooth control behavior in simulation as well as for real hardware. Further filter configurations have been tested offline and with a human in the loop. Butterworth filters of orders higher than 1 showed noticeable overshooting at high signal slopes for both sensor and prediction signals. A Butterworth filter of 1st order does not overshoot in its step response because of its pole constellation and is hence beneficial for both filtering sensor and prediction signals. Another advantage of this filter type is the monotonic amplitude response in both pass-band and stop-band.

2.1.3 Sensor Attachment and Movement Execution

This section describes the characteristics of the sensor fixation on the subjects forearm and how the different movements need to be executed in the training phase. The fixation quality has strong effect on the signal properties, as sensors could be too loose and slip from their initial position or too tight to wear them for the required time.

All sensors need to be distributed over the bracelet with equidistant positions. The first and last sensor of the bracelet meet at the closure, where the same sensor distance as between other sensors is kept. The proximal bracelet is positioned approximately 8 cm above the elbow. This can be measured when the elbow is in an perpendicular orientation to the table plane. The sensors were placed that the sensor housings do not touch the upper arm, when the elbow is flexed to angles larger than 90 °. The orientation of the bracelet is determined by the sensor with channel zero of the hardware, which is visibly marked. This sensor must lie on the *Ulna* in line with the elbow pit, when the forearm is in a relaxed position. The distal bracelet is directly positioned next to the proximal bracelet on the forearm. Again, this bracelet is oriented such that the marked sensor lies in line with the one of the proximal bracelet.

The bracelets are tightened at the closure, such that all sensors stay in touch with the skin during all possible movements of the hand and wrist. The tightness should be limited at some point to avoid strong pressure marks on the skin. Further, the bracelet should not influence the muscle activity negatively. The tightness should be within the limit, such that the bracelet can be worn without any discomfort for at least the duration of the experiment. After attaching both bracelets, each sensor is optically inspected if its bottom side is fully covered with skin. If any sensor is

tilted sideways after tightening and closing of the bracelet, its position is manually corrected.
The subject is instructed to execute the rest position as followed: Keep the forearm with minimal muscular contraction perpendicular to the table plane. The individual fingers are flexed to a certain degree without muscle contraction. The hand remains inline with the vertically oriented forearm. The wrist rotation is approximately in the middle of the angular space between the joint limits to allow a clear pronation and supination of this degree of freedom (DOF). The rest state is shown in Fig.2.5, where both bracelets are attached onto the forearm.
An action is the activation of one or more DOF of the human hand and wrist. The selected DOF are defined by a target vector, containing target values of all available DOFs in the system. A full activation is executed at about 40% of the maximum voluntary contraction (MVC) and is related to a target value of 1.
The wrist flexion (*fle*) and wrist extension (*ext*) shall be made with relaxed finger muscles. This can improve the distinctness between the wrist flexion and a flexion of individual fingers. The same accounts for the wrist extension, distinguished from an extension of individual fingers. The wrist pronation (*pro*) and wrist supination (*sup*) is a rotation of the *Ulna* around the *Radius* in the forearm. For simplification, these actions are related to as wrist rotations. The power grasp (*gra*) is the full flexion of all fingers, pressing against the palm. The thumb supports this grasp type by pressing on top of these fingers. The muscle force in each finger should be naturally distributed.
After the subject gets a stimulus, it is instructed to hold the action with a constant force level against the joint limit at 40% of the MVC until the end of the stimulus. The stimulus of the required actions throughout this work are shown in Fig. 2.4 with the left (grey) hand. The right (golden) hand is used to show the model prediction when the online performance needs to be evaluated. The visualization is realized using the modeling software *Blender*.

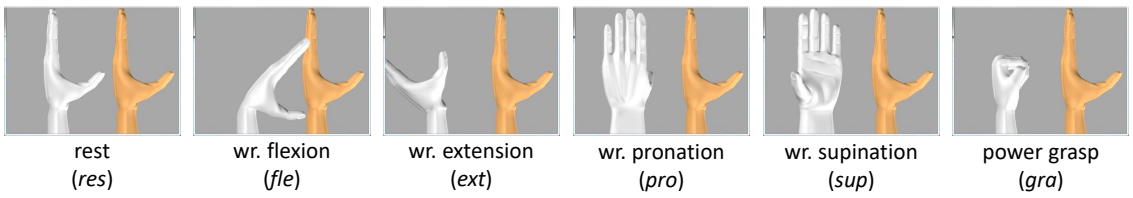

Figure 2.4: Visualization of stimulus and prediction with abbreviations in parenthesis. Left (grey) hand: stimulus. Right (golden) hand: prediction

2.2 Sensor Placement Experiment

To evaluate the effect of different placings of both sensor types on the forearm, the following experiment has been designed. A number of 20 available sensors is

placed on two individual Velcro straps to fit the resulting bracelets next to each other on the forearm. The region of interest is close to the proximal end of the forearm because of two reasons. First, transradial amputees have still an intact elbow joint with different forearm lengths. Prostheses are attached to the most distal possible position of the extremity, enabling the amputee to use the elbow joint as usual and use the forearm rotation to some extent. Second, the muscle bellies of the major forearm and hand muscles lie close to the proximal end of the forearm. Especially finger flexors and extensors as well as some forearm rotation muscles, e.g. *M. brachioradialis, M. supinator, M. pronator teres*, can be best interfaced here.
The sEMG and FMG sensors were placed in alternating order on the straps, which makes it possible to select single sensors in different patterns from both straps.

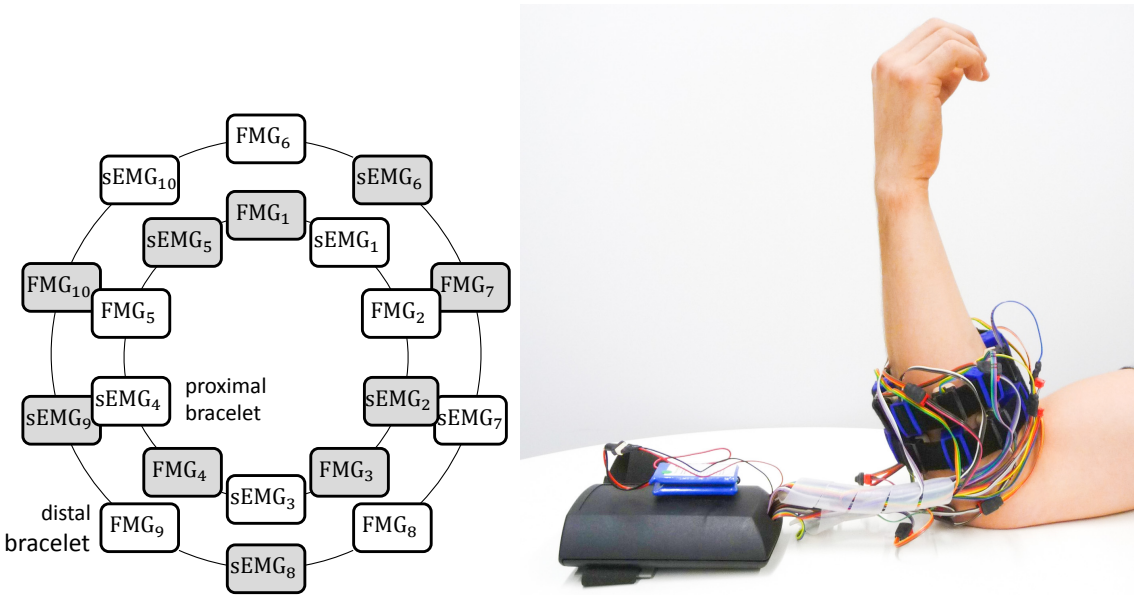

Figure 2.5: Sensor configuration on both bracelets and sensors attached on the forearm. Left: sensor configuration on both bracelets, where fields in grey are the selection for configuration *c3*. Right: sensors attached to the forearm.

2.2.1 Procedure

All subjects receive a written description of the experiment as well as an oral explanation about the procedure. Prior to their participation, the subjects sign a written consent form after all questions are answered. The experiment is approved by the work council of the DLR and conducted in accordance with the Declaration of Helsinki.
The subjects are asked for their preference of using their left or right arm during the experiment and the appropriate hand model is started. The hand model is shown in full-screen mode such that the subject can concentrate on the visual stimulus. The

elbow of the chosen arm is put on a soft pad on the table such that the forearm can rest in an upright position over the elbow. The chair height is adapted to a convenient and upright position in front of the monitor.
Both bracelets are adjusted to the circumference of the subject's forearm such that an equidistant positioning between all sensors can be ensured. The attachment onto the forearm is made as described in the previous section 2.1.3.
The data acquisition software is started and configured with an ID of the current subject, to enable an assignment of all data files and to anonymize the data. After asking the subject for his or her convenience, the stimulus and the corresponding data acquisition is started. Five repetitions of six actions have to be performed in accordance to the visual stimulus, which are given in Fig. 2.4.

2.2.2 Parameter Search

After collecting data from 10 subjects, a one dimensional parameter search has been conducted to optimize the RR-RFF regression model. The hyper-parameter σ is varied over a defined set of values. The chosen set has small increments related to small values with increased step size related to larger values. The second hyper-parameter λ, which penalizes large coefficients in the regression model, is constantly set to $\lambda = 1$. This parameter has only minor effect on the model properties compared to the influence of σ. The random feature properties of the algorithm enables already a good model fit, where the major model characteristics are shaped by the parameter σ.
First, the random parameters $\boldsymbol{\Omega}_1$ and $\boldsymbol{\beta}$ of the RR-RFF algorithm are drawn from a normal distribution

$$\boldsymbol{\Omega}_1 \sim \mathcal{N}(\mathbf{0}, \mathbf{1}) \in \mathbb{R}^{D \times d} \tag{2.1}$$

and an uniform distribution

$$\boldsymbol{\beta} \sim \mathcal{U}(-\pi, \pi) \in \mathbb{R}^{D}. \tag{2.2}$$

The number of chosen sensors is defined by d, which is the 10-dimensional input space in this experiment. The feature space dimensionality is set to $D = 300$, which is a trade-off between model accuracy and computational means. The random parameters are drawn $N_\mathrm{i} = 10$ times and stored in files before the data analysis. This enables multiple iterations of the grid search, which reduces the randomness of only one cross validation based on random parameters. This set of parameters is used for all subjects to further eliminate the randomness among subjects. A number of $N_\mathrm{i} = 10$) iterations has been selected.
Second, the random parameter $\boldsymbol{\Omega}_1$ is scaled by the hyper-parameter σ, found in the grid search. Hence, we obtain $\boldsymbol{\Omega} = \sigma\boldsymbol{\Omega}_1$ as parameter for the regression model, as a realization of $\mathcal{N}(0, \sigma)$
The training is based on the captured sensor data, stored in the design matrix $\boldsymbol{X} \in \mathbb{R}^{N_\mathrm{s} \times d}$ and the corresponding target values $\boldsymbol{Y} \in \mathbb{R}^{N_\mathrm{s} \times N_\mathrm{DOF}}$, where N_s is the

number of samples, N_{DOF} the number of DOFs and d the number of sensors. A sEMG and FMG sensor reading of the k-th sensor and the i-th sample is denoted by $x^{(i)}_{\mathrm{sEMG}k}$ and $x^{(i)}_{\mathrm{FMG}k}$. The sensor channels are stored column-wise in the full design matrix

$$\boldsymbol{X} = \begin{bmatrix} x^{(1)}_{\mathrm{sEMG1}} & \cdots & x^{(1)}_{\mathrm{sEMG10}} & x^{(1)}_{\mathrm{FMG1}} & \cdots & x^{(1)}_{\mathrm{FMG10}} \\ \vdots & \ddots & \vdots & \vdots & \ddots & \vdots \\ x^{(N_\mathrm{s})}_{\mathrm{sEMG1}} & \cdots & x^{(N_\mathrm{s})}_{\mathrm{sEMG10}} & x^{(N_\mathrm{s})}_{\mathrm{FMG1}} & \cdots & x^{(N_\mathrm{s})}_{\mathrm{FMG10}} \end{bmatrix} \tag{2.3}$$

and the corresponding design matrices of each sensor type are hence sub-matrices of $\boldsymbol{X}$, given by

$$\boldsymbol{X} = \begin{bmatrix} \boldsymbol{X}_{\mathrm{sEMG}} & \boldsymbol{X}_{\mathrm{FMG}} \end{bmatrix}. \tag{2.4}$$

For the training of the RR-RFF model for each configuration, the appropriate columns of the design matrix $\boldsymbol{X}$ are selected from Tab. 2.2 and Tab. 2.3 and put in

$$\boldsymbol{W} = (\varphi(\boldsymbol{X})^T)\varphi(\boldsymbol{X}) + \lambda \boldsymbol{I}_D)^{-1}(\varphi(\boldsymbol{X})^T \boldsymbol{Y}) \tag{2.5}$$

to calculate the model coefficients, where $\varphi(\boldsymbol{X})$ is the mapping function onto the higher-dimensional feature space, given by

$$\varphi(\boldsymbol{X}) = cos(\boldsymbol{X}\boldsymbol{\Omega}^T + \mathbf{1}_D \boldsymbol{\beta}^T), \tag{2.6}$$

where $\mathbf{1}_D$ is the column unit vector with D dimensions.
To obtain a prediction $\widehat{\boldsymbol{y}}$ of the trained model, employ

$$\widehat{\boldsymbol{y}} = \varphi(\boldsymbol{x})\, \boldsymbol{W} \tag{2.7}$$

with a given test sample $\boldsymbol{x}$, where $\varphi(\boldsymbol{x})$ is again the mapping function between input and feature space.
The model is trained with each hyper-parameter from the set of 55 σ-values over $N_i = 10$ iterations of the random parameter sets. The nRMSE is obtained by a five-fold leave-one-repetition-out cross-validation, where $N_r = 5$ is the number of repetitions for each action. The mean nRMSE for each $\mathrm{nRMSE}_{r,i}$ of repetition r and iteration i is given by

$$\mathrm{nRMSE} = \frac{1}{N_i N_r} \sum_{i=1}^{N_i} \sum_{r=1}^{N_r} \mathrm{nRMSE}_{i,r}. \tag{2.8}$$

The normalization is already achieved as the absolute maximum of each target value is 1.
An optimal parameter σ_s for each subject s can be found, which minimizes the nRMSE of this model. The parameter search took about 10 min. per subject (*Intel Xeon* CPU @ 2.80GHz).
This process has been conducted for the approaches *sEMG*, *FMG* and *ENS*. Table 2.1 summarizes these values.

Table 2.1: Individual sigma parameters for subject 1 to 10 and mean value over subjects.

Approach	1	2	3	4	5	6	7	8	9	10	σ_{mean}
sEMG	1.80	2.50	2.50	0.90	1.50	0.85	2.20	0.55	1.60	1.60	1.600
FMG	1.80	2.20	3.00	3.20	2.70	3.40	1.90	2.30	2.30	2.80	2.560
ENS	0.35	0.05	0.05	0.65	0.60	0.90	0.45	0.45	0.65	1.20	0.535

The hyper-parameters for method *STA* are already defined by the hyper-parameters of *sEMG* and *FMG* as their σ values can be directly used for the respective sensor types. This is achieved by defining a vector $\boldsymbol{\sigma}_{\text{STA}}$ in (2.9), which contains the already found hyper-parameters of the previous parameter search related to five sEMG and five FMG sensors. Differing from the other approaches, a hyper-parameter vector is used to scale the random values in $\boldsymbol{\Omega}_1$ instead of a scalar.

$$\boldsymbol{\sigma}_{\text{STA}} = \left[\sigma_{\text{sEMG}}, \cdots, \sigma_{\text{sEMG}}, \sigma_{\text{FMG}}, \cdots, \sigma_{\text{FMG}}\right]^T \in \mathbb{R}^d \tag{2.9}$$

2.2.3 Comparing Sensor Placement Configurations

To compare different sensor placements, three configurations have been defined in table 2.2, namely *c1, c2 and c3*. The sensor placement pattern over both bracelets is designed such that either one of the three placement configurations or one of the four approaches can be selected. It prevents a constellation, where two sensors of the same type lie next to each other for all made selections. In every selection, an alternating arrangement of both sensor types is desired. At the same time, the distribution of both sensor types around the forearm should be equal.

Table 2.2: Configurations of sensor placement

Config.	Description	Input
c1	proximal bracelet	$\boldsymbol{x}_{\text{c1}} = [\, x_{\text{sEMG1}}, \cdots, x_{\text{sEMG5}}, x_{\text{FMG1}}, \cdots, x_{\text{FMG5}} \,]$
c2	distal bracelet	$\boldsymbol{x}_{\text{c2}} = [\, x_{\text{sEMG6}}, \cdots, x_{\text{sEMG10}}, x_{\text{FMG6}}, \cdots, x_{\text{FMG10}} \,]$
c3	mixed selection (grey fields in Fig. 2.5)	$\boldsymbol{x}_{\text{c3}} = [\, x_{\text{sEMG2}}, x_{\text{sEMG5}}, x_{\text{sEMG6}}, x_{\text{sEMG8}}, x_{\text{sEMG9}}, x_{\text{FMG1}}, x_{\text{FMG3}}, x_{\text{FMG4}}, x_{\text{FMG7}}, x_{\text{FMG10}} \,]$

The sensor channels and their respective columns are selected from the design matrix for each configuration. The resulting nRMSE is again obtained by a five-fold leave-one-repetition-out cross-validation over 10 iterations. Figure 2.6 on the left contrasts the nRMSE of the different configurations.

2.2.4 Comparing Machine Learning Approaches

To compare the offline performance of the employed machine learning approaches, the input space of each approach is configured as in Tab. 2.3. The models are

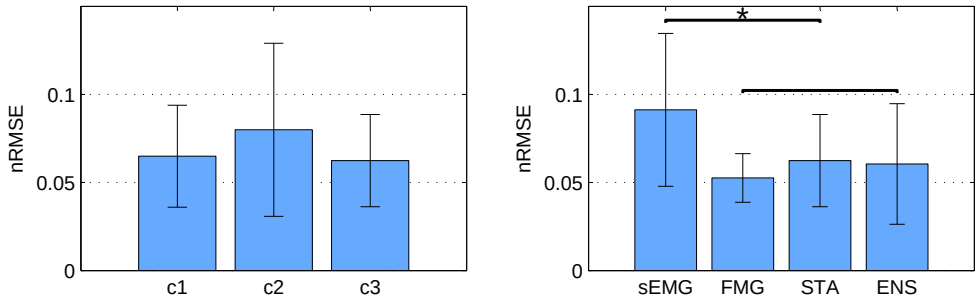

Figure 2.6: Results of the sensor placement experiment (with individual sigmas per subject). Left: comparison of configurations. Right: comparison of approaches.

evaluated based on the σ_s values individually per subject as described in section 2.2.2. A five-fold (leave-one-repetition-out) cross-validation has been performed over 10 realizations of the random parameter set to obtain the nRMSE of each approach. The results with standard deviations among the subjects are visualized in Fig. 2.6.

Table 2.3: Sensor selection for machine learning approaches.

ML Approach	Description	Input
sEMG	selecting 10 sEMG sensors, five per bracelet	$\boldsymbol{x} = [x_{\text{sEMG1}}, \cdots, x_{\text{sEMG10}}]$
FMG	selecting 10 FMG sensors, five per bracelet	$\boldsymbol{x} = [x_{\text{FMG1}}, \cdots, x_{\text{FMG10}}]$
STA	five sEMG and five FMG sensors in common input space	$\boldsymbol{x}_{\text{c3}}$ (see Tab. 2.2)
ENS	five sEMG and five FMG sensors in ensemble hierarchy	$\boldsymbol{x}_{\text{c3}}$ (see Tab. 2.2)

All tested approaches use a sensor selection which comes from both bracelets. This is naturally given for *sEMG* and *FMG* as their 10 related sensors are distributed over both bracelets. In the case of *STA* and *ENS*, the configuration *c3* has been selected, which expands the selection over both bracelets. This selection criterion makes the four approaches more comparable. It has already been shown in the comparison of the sensor placement configurations, that the effect is not significant in the offline analysis.

2.2.5 Offline Results

For the statistical evaluation of both sensor placement configurations and machine learning approaches, a repeated measures ANOVA is employed.

No significant difference between the three sensor placement configurations has been found ($F(2, 18) = 1.337, p = 0.287$). Pairwise interactions have been determined using the Tukey-test with $p = 0.397$ for *c1-c2*, $p = 0.975$ for *c1-c3* and $p = 0.285$ for *c2-c3*.
A significant difference between the four approaches has been found ($F(3, 27) = 7.05105, p = 0.0012$). The post-hoc Tukey-test showed that the approach *sEMG* is significantly worse than any other tested approach with p between < 0.001 and 0.00784. The remaining three approaches show no significant difference with p between 0.693 and 0.997.

2.2.6 Discussion

The statistical analysis shows no significant difference between the three sensor placement configurations. This deviates from [RSE16] where the classification error could be minimized by trying different sensor patterns out of an array of 126 pressure sensors. The different number of employed sensor and their placement density on the skin might cause this effect compared to this work.
Configuration *c2*, which are sensors from the distal bracelet, shows a higher nRMSE compared to the other approaches. This might be influenced by sensor alignment problems of this bracelet. The anatomy of the forearm shows a conical form between elbow and wrist. Starting at the elbow, the arm is more cylindrical but going further to the wrist, the arm gets more conical. As the bracelet is fixed at that transition area, it is problematic to properly place all sensor surfaces on the skin. The whole bracelet tends to slip towards the distal end of the arm, as the arm circumference decreases in that direction. In this region, sensor lift-off or shift might occur more often than in the region of the proximal bracelet.
The offline evaluation gives just a limited insight of the performance of each machine learning approach. The control loop involving subject and the machine learning algorithm is not closed and the online performance of the approach is unclear because the adaptive behavior of the human is neglected here. However, the results of the approaches involving sEMG all show a lower nRMSE than the approach, using sEMG only. This can point to positive properties of the FMG signals but also to meaningful combinations of sEMG and FMG. The combined sensors approaches *ENS* and *STA* show almost the same low nRMSE than *FMG*.

2.3 Online Performance Comparison

For the online evaluation, conducting a hyper-parameter search after the training phase of each subject is too time consuming. The subject would need to wait for the parameter search with the technical equipment fixated at his or her body. Hereby, using a general σ parameter for all subjects is desirable. First, the parameter selection process is described, which has a strong influence on the online performance

of each approach. Then the procedure of the experiment is outlined. In the end, the results are presented and discussed.

2.3.1 Parameter Selection

The intuitive first approach was to use σ_{mean} for future models. This was obtained by defining a σ_{mean} as mean value over all subjects. After testing the resulting model in an online scenario, it becomes evident that this parameter causes over-sensitive behavior for intermediate activations and hard to reach full activations. An explanation is that the variance of the normal distributed $\mathbf{\Omega}$ values is scaled by this parameter and larger values in $\mathbf{\Omega}$ lead to higher frequencies in the drawn cosine functions. It follows that higher frequencies enable steeper gradients and oscillations on the regression function.
The parameter search has been further explored to examine this behavior. Figure 2.7 shows a histogram of the σ values, which are obtained when a threshold of +5% is applied on the minimum nRMSE in the parameter search. Then, the minimum σ-parameter is selected with the maximum number of occurrences, indicated by the left red bar in the histogram. This value is termed as σ_{min} and for each approach, the values $\sigma_{\text{min}}^{\text{sEMG}} = 0.7$, $\sigma_{\text{min}}^{\text{FMG}} = 0.5$ and $\sigma_{\text{min}}^{\text{ENS}} = 0.15$ are obtained.

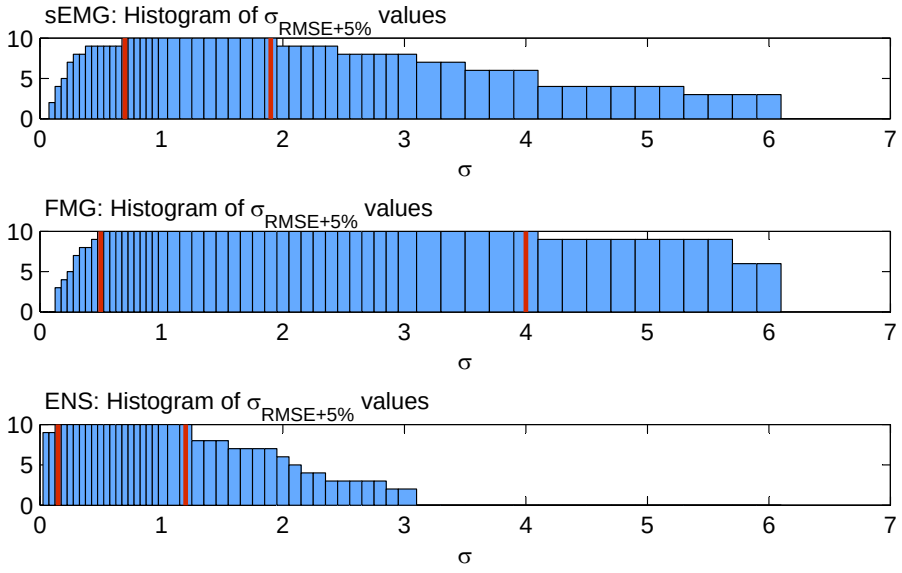

Figure 2.7: Histogram of sigma values where the nRMSE lies in an error threshold of +5%. Red bars indicate the interval of maximum occurrences among subjects.

As in the offline experiment, the hyper-parameter vector for *STA* is again constructed by the values from *sEMG* and *FMG*, resulting in

$$\boldsymbol{\sigma}_{\text{min}}^{\text{STA}} = \left[\sigma_{\text{min}}^{\text{sEMG}}, \cdots, \sigma_{\text{min}}^{\text{sEMG}}, \sigma_{\text{min}}^{\text{FMG}}, \cdots, \sigma_{\text{min}}^{\text{FMG}}\right] \in \mathbb{R}^d. \tag{2.10}$$

One could easily argue that the best parameter is selected where the model error is minimal. Problems arise if this argumentation is taken into to online case. In this special application, the regression is built only on three different target values, which are $\{-1, 0, 1\}$. A single activation (SA) is built on two target values only, which are either $\{0, 1\}$ or $\{0, -1\}$. In the online case, intermediate values are queried for regions where no training data was available. This differs from the offline case, where the model could be only tested with the available training data from rest position or full activation. The whole shape of the regression function is defined by two things: The selection of the hyper-parameters and the constellation of the training samples collected for a certain target value.

Paying attention to the hyper-parameters, Fig. 2.8 shows the model prediction of *STA*, when the input is linearly interpolated between rest cluster and each of the activation clusters. The left columns shows the case, where σ_{min} is used to train the model, the middle column shows the model, using σ_{mean} and the right column compares the output to a multiple linear regression model including a parameter for the y-intercept. The linear model gives an impression of where the cluster centers lie and how a linear connection between rest and the specific activation looks like.

The inner-cluster variance of an action and the inter-cluster variance between different actions in the input space play a major roll. For instance, collecting data for one action with a number of repetitions can result in a wide spread of the samples among the repetitions, if the subject performed with poor repeatability. This will result in a digressive curve between rest cluster X_0 and the desired target value, which causes a high sensitivity for intermediate activation levels. On the other hand, a low sensitivity to reach full activation levels can be achieved. See Fig. 2.9 for an example using a one-dimensional input x and simulated training data for the targets $y = 0$ and $y = 1$.

The simulated training data is drawn from a normal distribution with variance 0.04 for X_{good} and a variance 0.2 for X_{bad}. The linear input for x results in the model predictions y_{good} and y_{bad}. The left plot shows models which allow only a smooth regression function which corresponds to a smaller σ-parameter. The right plot shows models which allows smaller periods in the cosine base functions, corresponding to a larger σ-parameter. This models tends to overfit the training data. Both model types are trained on the same data. The slope of the regression curves is generally steeper for the training data X_{bad}. For the models using larger σ-values, the slope is further increased as already the first data samples between rest and full activation show a good approximation. Steep regression functions make the control highly sensitive for intermediate activations and are hence disadvantageous for proportional control.

We showed in a preliminary online experiment that the parameter type σ_{min} for the specific approach led to an intuitive behavior and a good control experience [NEC17]. These parameters are selected for the further online evaluation in this work.

2.3.2 Procedure

All subjects receive oral and written explanation of the experiment. A number of 12 subjects is engaged. Every participant receives a written consent form, as in the previous experiment. The duration of the experiment is about 45 min and it is split in two parts.

The first part, about 10 min, is the training phase where subjects need to follow a repetitive stimulus of hand and wrist actions. Again, five repetitions of six actions are recorded (including the rest position *res*).

The second part, about 35 min, is the online performance phase. The subjects need to follow a visual stimulus in order to reach targets with a virtual hand on the screen. Hereby, not only full activations as they occur during the training are tested. Intermediate activations at levels of 33% and 66% of all SA are also part of the target set. A total of 120 targets has to be reached, consisting of 40 full activations and 80 intermediate activations. Each target has to be reached twice. Reaching a target means to stay inside a bounded window of less than 1% of the full workspace for a holding time of $t_h = 1.5$s. If this requirement is fulfilled, the target is counted as *success*. If the subject is not able to accomplish the target within a timeout of $t_t = 15$s, it is counted as *no success*.

2.3.3 Workspace and Target Space Definition

The whole workspace is expanded between the limits of each DOF. The limits are $[-1, 1]$ for opposite actions *fle/ext* and *pro/sup* and $[0, 1]$ for the action *gra*. The limits -1 and 1 corresponds to a full activation of the related action. This leads to a workspace volume of $V_w = (1 - (-1))^2 \cdot (1 - 0) = 4$. For further DOF, the workspace volume would be calculated by a hyper-cuboid.

The target space is the space which needs to be entered in order to achieve a successful goal as described before. A target space V_t can be defined by an error margin ϵ on each DOF, which expands to both sides. This leads to a target space of $V_t = (2\epsilon)^{N_{\mathrm{DOF}}}$, where $N_{\mathrm{DOF}} = 3$ is the number of DOF in this experiment. The threshold is set to $\epsilon = 0.15$. This value represents a good balance of the success rate according to the abilities of the subject and to prevent frustration caused by low success rates.

The ratio between the target space and the whole workspace is given by

$$r_w = \frac{V_t}{V_w} = \frac{(2\epsilon)^{N_{\mathrm{DOF}}}}{V_w}. \tag{2.11}$$

This leads to a target space to workspace ratio of $r_w = 0.00675$ and shows that the probability to enter the goal randomly is quite low.

2.3.4 Online Results

The performance has been evaluated mainly on the success rate (SR)

$$SR = \frac{N_{\mathrm{SG}}}{N_{\mathrm{AG}}}, \tag{2.12}$$

which is the ratio between successful goals (N_{SG}) and all goals (N_{AG}).
This is used as the strongest measure of the performance of an approach. Values between $[0, 1]$ are possible.
Another metric is the task completion time (TCT), which is the average time of completing a successful goal (SG). Unsuccessful goals are excluded here. The TCT is a measure of time it took the subject to reach the goal starting at the rest position until entering the SG. The holding time of $t_h = 1.5$s is not included and values between $[0, t_t[$ are possible, because the timeout is not active at holding a SG. This metric also helps to evaluate the stability of an approach. An unstable or non-intuitive approach requires the subject more time to reach the goal or instability causes the prediction to leave the target space again. The TCT_i values for each goal i are averaged over all successful goals by

$$TCT = \frac{1}{N_{\mathrm{SG}}} \cdot \sum_{i=1}^{N_{\mathrm{SG}}} TCT_i, \tag{2.13}$$

where N_{SG} is the number of successful goals.
As a third metric, the in-goal-time (IGT) is used, given by (2.14). This is the sum of each period the subject stays inside the target space. Therefore, only unsuccessful goals with a sum larger than zero are taken into account. The number of these unsuccessful, reachable goals (URG) is termed as N_{URG}. A total time inside the target of zero is counted as an unreachable goal and excluded in this metric. As a stable holding time inside the target space of 1.5 seconds is required, this metric identifies mostly unstable approaches. For example, the target space of a goal is entered multiple times but the holding time is never reached. This leads to a high IGT compared to an approach which enables a stable prediction inside the target space.

$$IGT = \frac{1}{N_{\mathrm{URG}}} \cdot \sum_{i=1}^{N_{\mathrm{URG}}} \sum_{k=1}^{N_{i,K}} t_{i,k} \tag{2.14}$$

Each IGT_i for an URG i is a sum of a number $N_{i,K}$ of periods $t_{i,k}$, while the target space is entered. These values are averaged over all URG. The number of $N_{i,K}$ periods can be between $[1, \infty[$. Each single period $t_{i,k}$ can be within $[0, t_h[$ seconds. For longer periods, the goal would be counted as successful as the holding time is fulfilled.
Figure 2.10 shows the results using the three metrics on the left. A repeated measures ANOVA has been conducted for all metrics. A significant difference for the

SR between the four approaches has been found ($F(3, 33) = 23.536, p < 0.0001$). A post-hoc Tuckey test is used to test the pairwise interactions. It shows that all approaches are significantly different from each other (all $p < 0.01$) except the comparison of *STA* and *FMG* with $p = 0.996$. The highest SR can be found for *STA* and *FMG* which shows that the approach using only FMG signals performed as good as a mixture of both signal types.

Analyzing the TCT, a significant difference has been found ($F(3, 33) = 3.630, p = 0.0228$). The post-hoc Tuckey test reveals a significant difference only for the approaches *sEMG* and *FMG* ($p = 0.0167$). All other interactions were not significant. This shows that the sEMG signals might have introduced more instability into the system which would require more time to reach a goal in average.

Evaluating the IGT statistically, the repeated measures ANOVA shows a significant difference ($F(3, 33) = 11.003, p < 0.0001$). The post-hoc Tuckey test shows significant difference between the groups *FMG-ENS*, *sEMG-FMG* and *STA-FMG* with all $p < 0.01$. All approaches involving sEMG signals show a significantly higher IGT than the approach *FMG*. The approach *sEMG* shows the highest IGT. This could be again caused by the signal instability. In that case, the subjects could reach many of the goals but the holding time was never exceeded. Hereby, the goals were reentered multiple times until the timeout occurs.

Looking at the right plots of Fig. 2.10, the SR for full (SR_{full}) and for intermediate activations (SR_{int}) is plotted independently. Full activations are the same as they occurred during the training phase. Hence, training data for these activations has been collected. Intermediate activations are goals, where 33% or 66% of the full activation level is targeted. These activations are predicted based on the regression curve between rest and full activation where no training data is available.

There is no significant difference between the approaches for SR_{full} ($F(3, 33) = 0.6166, p = 0.6092$). For SR_{int}, there is a significant difference over the approaches ($F(3, 33) = 31.165, p < 0.0001$). The post-hoc Tuckey test reveals that all approaches are significantly different from each other (all $p < 0.01$) except *STA* and *FMG* ($p = 0.998$). The independent analysis of full and intermediate activations SR shows again that *STA* and *FMG* are the two most successful approaches without a significant difference in their performance.

Comparing only *STA* and *FMG*, the SR for all, full and intermediate activations is not significantly different. Also the TCT is not significantly different. Only the IGT shows a significantly higher mean value for *STA* compared to *FMG*. If the IGT is regarded as a stability measure for the online control, higher IGT indicates a more unstable approach *STA*.

As a last analysis, the SR of each approach is examined action-wise as well as DOF-wise. This means that a SR for each specific action can be determined. Further, it is possible to determine a SR for each available DOF. As some of the actions lie on opposite directions on the same DOF, there are more groups for the actions than for the DOF. This analysis is shown in Fig. 2.11.

A two-way repeated measures ANOVA for the factors approach and action shows a significant effect of the factor approach ($F(3, 33) = 23.54, p < 0.0001$) and a significant effect of the factor action ($F(4, 44) = 3.363, p = 0.0174$) but no significant interaction effect between approach and action ($F(12, 132) = 1.352, p = 0.197$).
The same statistical analysis for the DOF-wise SR shows a significant effect of the factor approach ($F(3, 33) = 20.49, p < 0.0001$) but neither significant effects for the factor action ($F(2, 22) = 2.912, p = 0.0755$) nor for the interaction effect between approach and action ($F(6, 66) = 0.855, p = 0.533$).

2.3.5 Discussion

A few subjects complained about the tightness of the bracelets, which felt increasingly inconvenient towards the end of the experiment. All of these subjects decided to finish the experiment after the experimenter asked about their condition. This shows that the sensor tightening is a crucial process which leads to problems if the bracelet is tightened by a third person and if the subject has little knowledge about the required tightness. A initial good feeling about the tightness can later on lead to discomfort, as the sensors deform the skin for a long time. As a solution, a procedure for inexperienced users could be applied, where for instance the sum of the FMG signals need to be at a defined level during bracelet fitting. This signal sum is then related to the pressure of the sensors on the skin and a measure for the bracelet strength. During the experiment, only a vague visual inspection of the FMG signals took place during the bracelet fitting, as it was considered as more important that the surface of all sensors fully covers the skin and no tilting occurs.
The results emphasize the stability and the good performance of using only FMG signals for human intend inference. The performance of *STA* is comparable in the SR and the TCT. The results of the IGT can be interpreted differently. If a high IGT is interpreted as measure for instability, *STA* performed worse than *FMG*. It is emphasized that the signal filtering characteristic has strong influence on the online performance of an approach. Low-pass filters with very low cutoff frequencies enable a smooth control, which can be unnecessarily slow and frustrating for the user. Low-pass filters with a higher cutoff frequency might let pass to much noise and a stable control of the user's intent is hard to achieve. In this experiment, both signal type filters are configured the same. For both signal types, a responsive system was desired. If the low-pass signal filter for sEMG would have been configured with a lower cutoff frequency, the approaches using this signal type could have possibly performed better. This would only affect failures due to instability but would introduce further delay into the prediction system.
The action-wise and DOF-wise analysis could be helpful, if there is a superiority of a certain approach related to a certain action or DOF. As it is unclear which action is the intent of the user in the online case and some actions lie on the same DOF, the online selection of a certain approach is a difficult problem. A simpler solution

could be a static configuration of which approach is related to which DOF. Opposite actions on each DOF would then be executed with the same approach.

2.4 Conclusion

The two conducted experiments evaluated the effect of different sensor placements in an offline experiment and the effect of different machine learning approaches in both offline and online experiments. It has shown that the performance of a LM using only FMG sensors is similar to the approach of stacking both sensor types into the same input space. The effect of the sensor placements on different defined regions of the forearm is not significant. Although the compared nRMSE were not significantly different, the proximal bracelet selection led to the largest nRMSE. This could be caused by the forearm anatomy causing a worse sensor fit and possibly sensor lift off. The mixed selection of both bracelet showed a comparable nRMSE as the proximal bracelet selection. For future experiments, a random sensor placement of both sensor types can be regarded as uncritical.
The offline performance of machine learning approaches differs usually from the online performance. In this case, high nRMSE values from the offline analysis corresponds to low SR in the online analysis. This shows at least that the offline and online analysis are in relation among the approaches.
The initially defined hyper-parameters σ_{mean} from the offline-analysis did not lead to promising results in the online case. The intuitiveness of an approach and the control experience are rather subjective feelings of the user. The hyper-parameters σ_{min} for the online experiment could be selected after an extended analysis of the offline data and with the help of preliminary online tests, where different parameter sets were employed.
Future experiments can be grounded on the hyper-parameters found in the offline experiment which were used in the online experiment. The results of the action-wise and DOF-wise performance analysis can be possibly used in novel approaches.

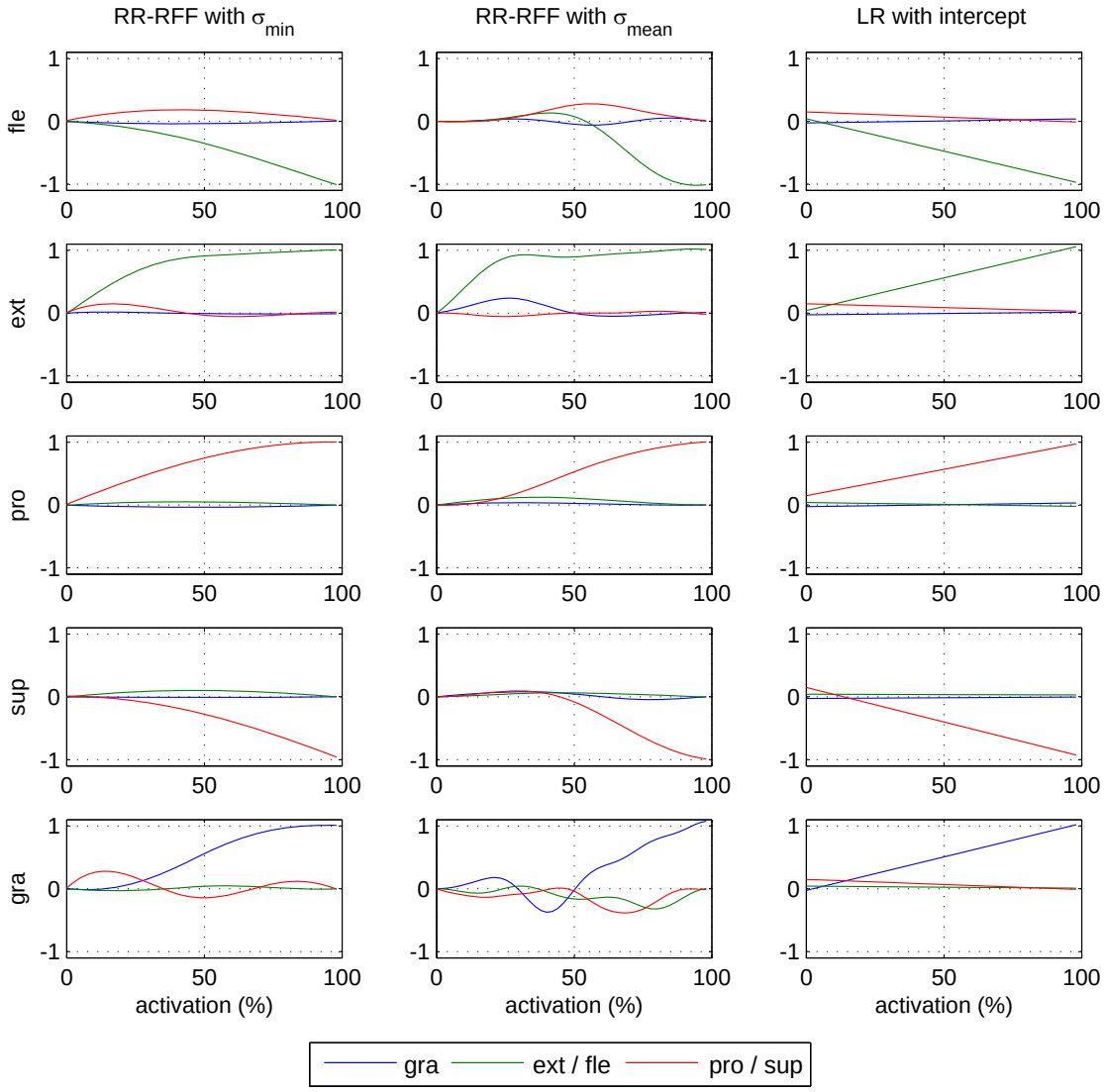

Figure 2.8: Model prediction of *STA* for an interpolated linear input between rest and the full activation. Left: predictions of RR-RFF model trained with $\sigma_{\min}$. Middle: predictions of RR-RFF model trained with σ_{mean}. Right: prediction of LR model with intercept.

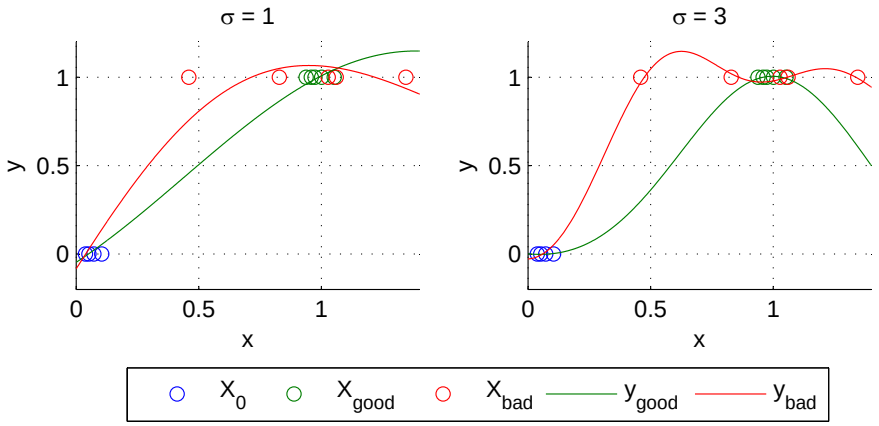

Figure 2.9: Comparison between good and bad repeatability for a constant target value, with data clusters X_{good} and X_{bad}. Left and right plots show the prediction $\widehat{y}$ of differently parameterized regression models trained on the respective cluster.

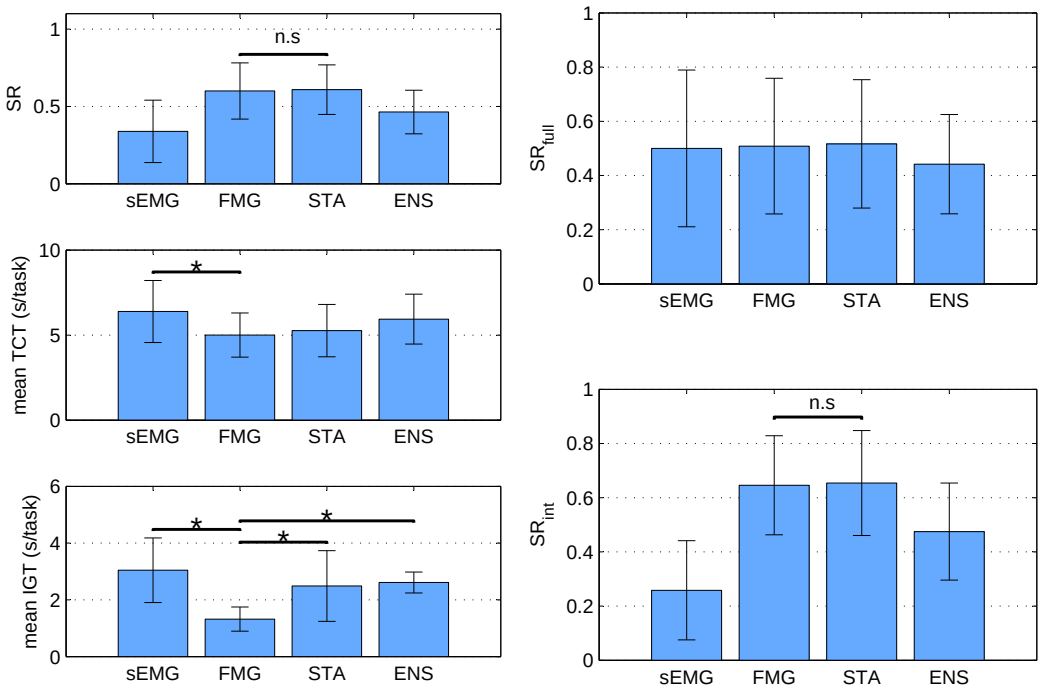

Figure 2.10: Results of the online experiment with common sigmas. Plots with horizontal bar captioned *n.s* denote the only non-significant difference between all pairs. Left: success rate (SR) over all tasks, mean task-completion-time (TCT) and mean in-goal-time (IGT). Right: Comparison of approaches for full activations (SR_{full}) and intermediate activations (SR_{int}).

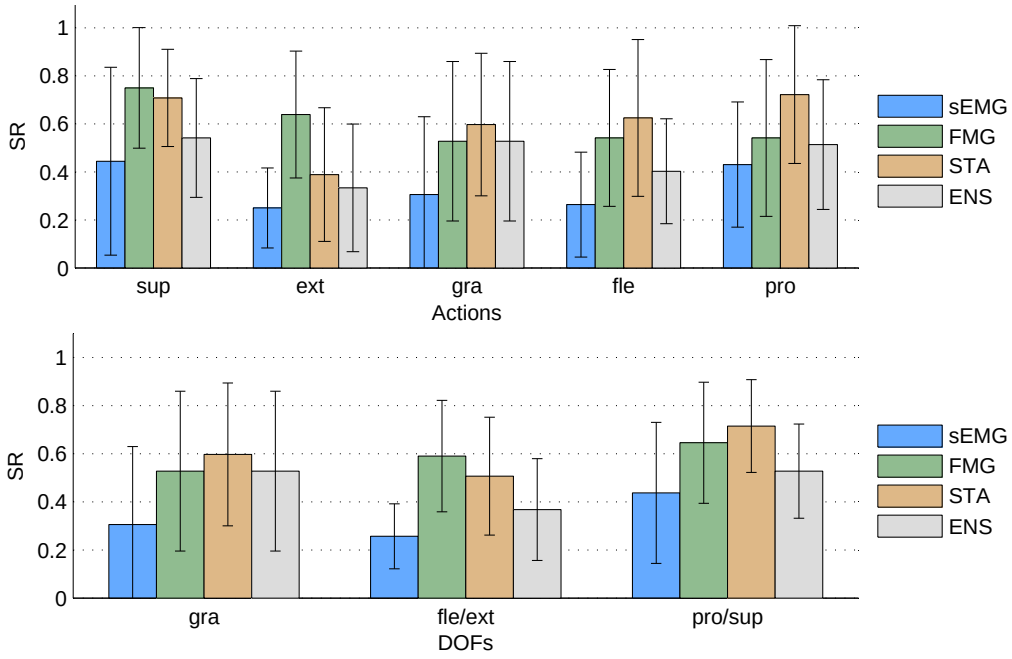

Figure 2.11: Results of the online experiment with common sigmas. Top: Action-wise comparison. Bottom: DOF-wise comparison.

Chapter 3

Sensor Fusion Study

In this chapter, the physical properties behind the produced sensor signals are shortly described. The signal characteristics of both sEMG and FMG sensors are outlined and how they are affected by different disturbances. The Kalman filter is introduced as an probabilistic sensor fusion approach and employed in a single-subject study to evaluate its performance.

3.1 Physical Properties

Humans control the unloaded position of their intact hand and wrist by exerting very sensitive muscle contractions. In an unloaded scenario, the muscle contractions need to be strong enough to overcome the friction of the gliding tendons in their channels as well as the internal tissue frictions of the muscle deformations and joint friction of the actuated limb. Further, the weight of the actuated limb itself need to be compensated, which is comparably low for the hand related to the wrist joint. Higher muscle forces for unloaded scenarios can occur at the elbow joint, depending on the elbow joint position, as the forearm and the hand act as a leverage. For position control of the hand and wrist, both proprioception and visual feedback is used to close the human control loop. At the point, where a joint reaches its limits, further torque can be applied through muscle contraction, where the joint limit acts as an compliant hard stop. This hard stop allows only small compression and the joint torque can be raised until the maximum contraction of the user.
This behavior shows basically to stages, starting from the limbs rest position:
Stage one: The user actuates the limb with minimal force due to free movement in position control using proprioception and visual feedback. During free movement, a displacement of the muscle and its contraction belly occurs even for minimal forces.
Stage two: The user has reached the joint limit and increases the muscular force, mainly in force control using proprioception to regulate the muscle strength. In this state, an isometric contraction is applied, as the muscle length is kept almost constant.

The different stages in control of intact human limbs produce different signal features at the employed sensors. A problem for the transfer of the control strategy to an amputee is seen in the different physical properties and the probable different control scheme than intact subjects. If the residual tendons in the stump are fixated at the bone, the amputee would only act in isometric contraction. This hypothesis affects the control strategy in myocontrol with either two control strategies of intact subjects compared to an assumed single control strategy of amputees.

In loaded scenarios, where the subject bears a weight, grasped with his or her fingers, the force in the moving DOF of the forearm is related to that weight. For an amputee, these forces are not related to the object weight lifted with the prosthesis. In the experiments of this work, only unloaded scenarios are considered. The effects of different weight in the hand of the subjects are so far not considered.

3.2 Sensor Characteristics

The sEMG sensors placed on top of the skin are subjected to different time-dependent effects. Humidity strongly influences the signal strength. Sweating is mainly caused by covering the skin with the sensors. Rising humidity usually increases the signal levels and reduces the noise, which leads to better training data. If training data is collected shortly after the sensor attachment, the signal levels tend to be smaller compared to a later state. The signal levels rise and the signal noise is reduced after a while by the rising skin conductance. This is problematic as the training signals differ from the later online signals. One solution can be to moisturize the skin with water before attaching the sensors or simply wait some time after attaching the sensors in order to let the sensor characteristics settle.

The FSR sensors, which are embedded in a rubber casing have a spherical head to sense the muscle deformation through the tissue and skin layers between muscle and skin surface. After wearing these sensors for a certain time, the skin shows a reversible plastic deformation relative to the ball shaped sensor head. These can be seen after removing the sensors from the forearm. A slight indentation of a depth of around 1 mm remains, which is surrounded by a small elevation of skin. These indentations vanish after one minute. This leads to the assumption that the tissue behaves like a semi-flexible material with changing characteristics over time. As the pressures onto the sensor surface are relatively small, the semi-flexible behavior might cause a time dependent change in the signal characteristics of the FSR sensors.

Both sensor types are affected by the body temperature and the ambient temperature. Changes can influence the electronics. As both sensor types are arranged on two bracelets, bracelet or individual sensor slippage needs to be prevented during the whole wearing time.

3.3 Kalman Filtering

As an alternative approach of fusing different sensor signals, the Kalman filter (KF) is shortly introduced here. The filter comes with the property that the process noise and the observation noise can be modeled. This allows a definition of different observation noises for the employed sensor types. With a proper weighting of the observation noise of a certain sensor modality, a probabilistic fusion approach of a multi-modal sensor input becomes possible. In relation to the *STA* approach, where only different hyper-parameters could be set for different sensor types, the Kalman filter enables either a static observation model for the fusion of both sensor types as well as an adaptive observation model with an online varying sensor confidence.
The state-space model of the prosthesis DOF positions y_k at timestep k can be modeled by

$$\boldsymbol{y}_k = f(\boldsymbol{y}_{k-1}, \boldsymbol{u}_k) + \boldsymbol{w}_k \ , \qquad \boldsymbol{w}_k \sim \mathcal{N}(\boldsymbol{0}, \boldsymbol{Q}_k) \tag{3.1}$$

as a function of the previous state $\boldsymbol{y}_{k-1}$ and a control input $\boldsymbol{u}_k$ with additive process noise $\boldsymbol{w}_k$
The non-linear observation model is given by

$$\boldsymbol{z}_k = h(\boldsymbol{y}_k) + \boldsymbol{v}_k \ , \qquad \boldsymbol{v}_k \sim \mathcal{N}(\boldsymbol{0}, \boldsymbol{R}_k), \tag{3.2}$$

which is a function of the current state $\boldsymbol{y}_k$ with additive observation noise $\boldsymbol{v}_k$. The observation model describes a sensor reading $\boldsymbol{z}_k$ at state k.
The problem with this formulation is that a mapping between the d-dimensional measurement vector $\boldsymbol{z}_k \in \mathbb{R}^d$ and the current state $\boldsymbol{y}_k \in \mathbb{R}^{N_{\text{DOF}}}$ with a number of N_{DOF} output DOF is required. This mapping is learned through RR-RFF in the previous experiments, which has been shown to be a good algorithm in the regression problem of myocontrol. In the notation of the observation model (3.2), this mapping of the RR-RFF model would need to be inverted. The multiple input and multiple output (MIMO) system has a number of 20 sensors as input (10 sEMG, 10 FMG) and a number of $N_{\text{DOF}} = 3$ as output. To find an inverse mapping from output to input, a under-determined non-linear equation system needs to be solved which has infinite solutions. No unique solution exists for a model inversion of the RR-RFF model. Therefore, including the regression model directly into the Kalman filter state space models is problematic.
A simplified problem can be obtained when the Kalman filter is used to fuse the output of two independent regression models, one for each sensor type. This yields to a linear state space observation model, where no inversion of a regression model is required. Hereby, the confidence can be modeled for each sEMG and FMG related DOF. The confidence per DOF can be defined through the previously conducted analysis of the success rates per DOF in section 2.3.4. A system block diagram can be found in Fig. 3.1.
The new state of the process can be simply modeled by its old state and as there is no further control input, a simple *random walk* model is defined by

$$\boldsymbol{y}_k = \boldsymbol{y}_{k-1} + \boldsymbol{w}_k \ , \qquad \boldsymbol{w}_k \sim \mathcal{N}(\boldsymbol{0}, \boldsymbol{Q}), \tag{3.3}$$

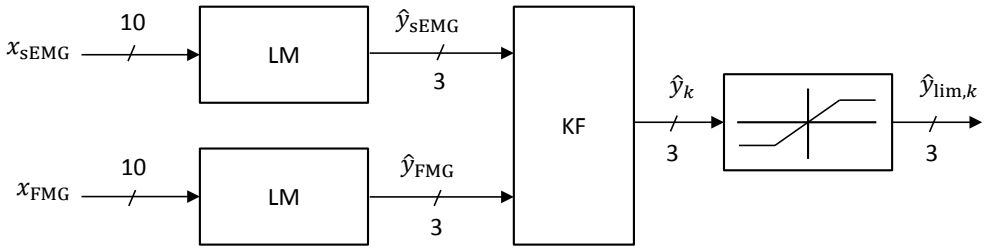

Figure 3.1: Kalman filter system block diagram

where $\boldsymbol{y}_k \in \mathbb{R}^{N_{\text{DOF}}}$ is the current state in three DOF.
The linear observation model is given by

$$\boldsymbol{z}_k = \boldsymbol{H}\boldsymbol{y}_k + \boldsymbol{v}_k \ , \qquad \boldsymbol{v}_k \sim \mathcal{N}(\boldsymbol{0}, \boldsymbol{R}), \tag{3.4}$$

where $\boldsymbol{z}_k \in \mathbb{R}^{2N_{\text{DOF}}}$ is the measurement vector containing both model predictions $\hat{\boldsymbol{y}}_{\text{sEMG}},\ \hat{\boldsymbol{y}}_{\text{FMG}} \in \mathbb{R}^{N_{\text{DOF}}}$

$$\boldsymbol{z}_k = \begin{bmatrix} \hat{\boldsymbol{y}}_{\text{sEMG}} \\ \hat{\boldsymbol{y}}_{\text{FMG}} \end{bmatrix}. \tag{3.5}$$

The measurement matrix $\boldsymbol{H}$ contains the mapping between system state and both of the LM prediction outputs and is simply constructed by

$$\boldsymbol{H} = \begin{bmatrix} \boldsymbol{I}_{N_{\text{DOF}}} \\ \boldsymbol{I}_{N_{\text{DOF}}} \end{bmatrix}, \tag{3.6}$$

where $\boldsymbol{I}_{N_{\text{DOF}}}$ is the square identity matrix of size N_{DOF}. The observation noise covariance matrix $\boldsymbol{R}$ is kept constant based on the online analysis per DOF.
In this approach, the confidences for the observation noise covariance matrix $\boldsymbol{R}$ are directly related to the DOF-based success rates from the previous experiment. A normalized success rate $\widetilde{SR}$ is obtained by

$$\begin{aligned} \widetilde{SR}^{(l)}_{\text{sEMG}} &= \frac{SR^{(l)}_{\text{sEMG}}}{max\{SR^{(l)}_{\text{sEMG}}, SR^{(l)}_{\text{FMG}}\}} \\ \widetilde{SR}^{(l)}_{\text{FMG}} &= \frac{SR^{(l)}_{\text{FMG}}}{max\{SR^{(l)}_{\text{sEMG}}, SR^{(l)}_{\text{FMG}}\}} \end{aligned} \tag{3.7}$$

for each DOF l and for both sensor modalities. The SR of the approaches *sEMG* and *FMG* are normalized by the maximum SR over both approaches.
A value for the uncertainty of a specific DOF is obtained by

$$\begin{aligned} V^{(l)}_{\text{sEMG}} &= \frac{1}{\widetilde{SR}^{(l)}_{\text{sEMG}}} \\ V^{(l)}_{\text{FMG}} &= \frac{1}{\widetilde{SR}^{(l)}_{\text{FMG}}} \end{aligned} \tag{3.8}$$

for both approaches, where the value $\widetilde{SR}$ is inverted such that high values are related to low variances and vice versa.

Table 3.1: Uncertainty of a DOF w.r.t normalized success rate ($\widetilde{SR}$).

l	DOF Name	$\widetilde{SR}^{(k)}_{\text{sEMG}}$	$\widetilde{SR}^{(k)}_{\text{FMG}}$	$V^{(k)}_{\text{sEMG}}$	$V^{(k)}_{\text{FMG}}$
1	*gra*	0.578	1	1.727	1
2	*fle/ext*	0.435	1	2.297	1
3	*pro/sup*	0.677	1	1.476	1

With the values for the DOF-wise uncertainty, the observation noise covariance matrix is modeled by

$$\boldsymbol{R} = diag(\ V^{\text{gra}}_{\text{sEMG}}, V^{\text{fle/ext}}_{\text{sEMG}}, V^{\text{pro/sup}}_{\text{sEMG}}, V^{\text{gra}}_{\text{FMG}}, V^{\text{fle/ext}}_{\text{FMG}}, V^{\text{pro/sup}}_{\text{FMG}}\ ). \tag{3.9}$$

Only the diagonal elements are used to define the uncertainty of each DOF. Each DOF occurs twice, one for each prediction output of the two regression algorithms. The process noise σ^2_Q is chosen, such that the relation between trusting the process and trusting the observations shows good controllability in the online case. For the simple *random walk* state space model, influencing the process noise behaves like tuning a low pass filter's characteristics of the prediction. The process should not be modeled unnecessarily slow but slow enough to filter out noisy observations. The process noise covariance matrix is defined as diagonal matrix $\boldsymbol{Q} = \sigma^2_Q \cdot \boldsymbol{I}_{N_{\text{DOF}}}$, where $\boldsymbol{I}_{N_{\text{DOF}}}$ is the square identity matrix of size N_{DOF}. For the following study, a value of $\sigma^2_Q = 0.01$ has been chosen. This value has been found in preliminary experiments as a trade-off between smoothing of the prediction and a reactive behavior as in approach *STA*.
The filter output $\hat{\boldsymbol{y}}_k$ at each timestep k is calculated by the well known equations for the update and correction step of a simple Kalman filter.

3.3.1 Study Design

This study is rather a feasibility analysis of a possible sensor fusion algorithm and does not involve a variety of human subjects.
The hypothesis is that the Kalman filter approach (*KF*) reaches a comparable success rate (SR) as the approach *STA*. For the approach *KF*, further knowledge has been provided in form of the previously determined DOF-wise SR. This SR are used as a confidence measure for each DOF and gives a level of confidence to the *sEMG* or to the *FMG* approach.
As the KF is applied in discrete time domain, a direct online evaluation of the approach is necessary. A number of 120 goals has been created, consisting of full and intermediate activations. The goal reaching task is designed as in the previous experiment, using a visual stimulus. To evaluate the online results, the approach is

compared to the already known stack method, which can be regarded as the simplest sensor fusion algorithm in this application.
The sequence of active approaches as well es the queried goals are in a random order and unknown to the subject. Temporal learning effects or temporally changing signal characteristics are neglected in the comparison as both methods occur in a random sequence, where the chance to hit the same method again after another is 50%. Each goal occurs twice for each method, which results in 60 tasks per method.
In this study, a number of 20 sensors, 10 sEMG and 10 FMG is used, which are distributed over two bracelets in alternating order. The σ_{min}-parameter vector for the approach *STA* has been chosen from the previous experiment.

3.3.2 Results

The SR and the TCT of both approaches were compared, shown in Fig. 3.2.

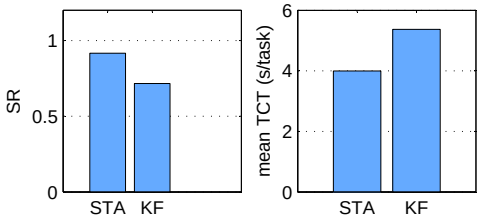

Figure 3.2: Kalman filter performance results. Left: SR per approach. Right: TCT per approach.

As the results come from one subject only, they were not statistically evaluated. The absolute SR is 20% lower for the KF and the TCT is 1.37 s higher, which is an increase of 34% compared to *STA*.
The prediction outputs of all involved learning machines are shown in Fig. 3.3 for the DOF of *fle/ext*. The goals at this time window were a full *fle* (target value -1 until 1 s) and the rest position (target value 0 at 3 s) followed by a full *ext* (target value 1 from 3 s to 6 s) at the active output of the KF. The outputs of the learning machines for sEMG and FMG act as the inputs of the KF. The KF trusts the FMG modality more as it is configured and the filter output is shifted towards the FMG prediction. It successfully filters out noisy sEMG predictions, noticeable at 3 s . The output of the KF is also compared to the *STA* prediction and differs only slightly in this DOF. The output comparison of different approaches is problematic as only one approach can be active at a time and the subject closes the control loop using this specific approach. The resulting output of other approaches is biased as the subject does not perceive their prediction. Regardless the output of the shown DOF, other DOF can strongly deviate from the goal requirement. Cross-activations of other DOF cannot be evaluated in such plots.

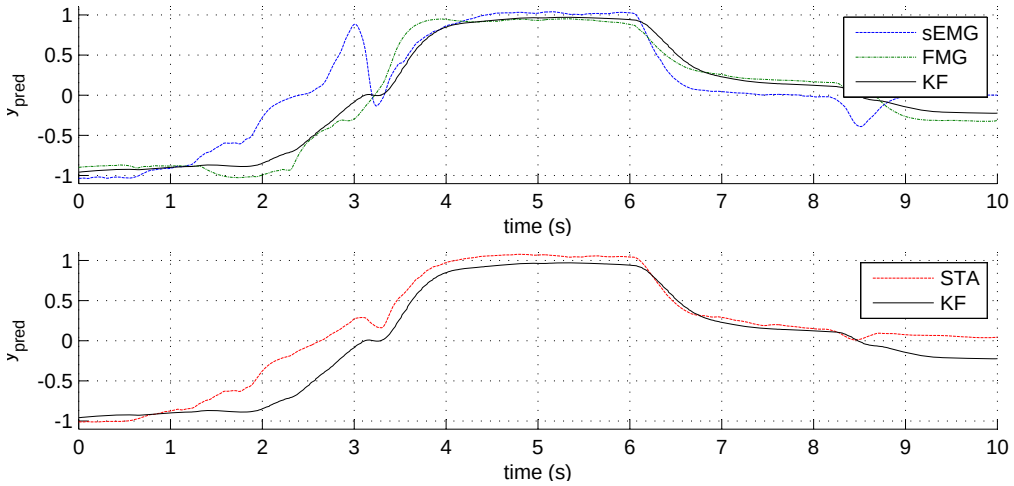

Figure 3.3: Kalman filter prediction output for DOF *fle/ext* compared to other LM predictions.

3.3.3 Discussion and Conclusion

With the approach *STA* using all 20 sensors, a SR of 92% could be reached, compared to an average SR of 61% reached in the previous experiment. The higher SR can be caused by the increased number of sensors but also through the influence of a more experienced subject. The KF using 20 sensors reached a SR of 72% which is also noticeable higher as all other approaches in the previous experiment, where the two best approaches were *STA* ($SR = 61\%$) and *FMG* ($SR = 60\%$).

In this experiment, an approach acting in discrete time domain has been compared with a regression based algorithm. In the regression algorithm, two low-pass filters are used, one for the sensor input and one for the prediction output. As the Kalman filter considers the parameterized process noise, additional filtering of the output is unnecessary.

The results for the KF show a worse performance as the approach *STA*. The KF fuses the information from two different regression models online with only the knowledge about the signal noise of a channel but without any noise correlations. In comparison, the regression algorithm for *STA* uses training data, where both signal modalities are in a relation for the specific target values. This additional knowledge about the signal relation might improve the prediction compared to the unrelated signals in the KF. Furthermore, the noise occurring at the signal readings, which is assumed to be Gaussian is further transformed using the non-linear regression functions of the LM. This may introduce further errors as the assumption is made that the noise on the predictions of the LM is also Gaussian. This is technically impossible as a non-linear transformation of a Gaussian random variable will not result in a Gaussian random variable. Nevertheless, this assumption has been made

as the full observation model between sensor and model prediction could not be inverted and has been excluded from the filter.
As there is a possibility to define the correlation of the noise in the observations between different channels of the KF, further knowledge could be provided to the system. This information could come from an online noise estimation of the different input signals and their possibly correlated noise. The values for the confidence of the different input signals can be potentially improved. Further experiments could provide better values, where the focus is on the interactions between different activations.
The KF performed worse as the so far best sensor fusion approach *STA*. Although its worse performance, it comes with the possibility to configure process and observation noise and facilitates an online adaption of these values. Furthermore, a probabilistic approach like this could handle the change in signal characteristic in the future, caused by sweating or muscle fatigue. If the confidence of the inputs can be determined online, less confident signals can be neglected for the prediction. On the one hand, this is mostly perceivable for the sEMG prediction at activation of different actions, when strong noise occurs compared to the FMG prediction. On the other hand, the LM using sEMG shows a perfect rest position as the muscles are relaxed but the FMG prediction is noticeable off the rest position.
In conclusion, only modeling the confidence for different DOF of each modality may be problematic as the KF tries to predict a system state in discrete time domain using a noisy process model and a noisy observation model. The noise on this signals can be differentiated from unintended activations of DOF which may occur at the activation of a specific action. This unintended activations could either come from a ill-formed regression model or from anatomical properties. Therefore, modeling the noise in discrete time domain does not represent the unintended activations, which are time invariant and rather dependent on the activation level of a certain DOF.

Chapter 4

Applying Linearly Enhanced Training (LET)

4.1 Motivation and Problem Description

In simultaneous and proportional myocontrol it is desirable to combine different hand and wrist movements. A good prediction model can be achieved if training data of the required SA as well as training data of their related combinations, which are termed multiple activations (MA), is available. For example, training a machine learning method on the data of wrist flexion, power grasp and the combination of them.

Training on SA only will in general not correctly predict simultaneous activations of multiple DOFs. For a set of SA, the number of possible MA quickly raises and becomes infeasible during the training with a subject. Furthermore, the combination of SA during training can be an impossible task for an amputee. This can be due to the lack of visual feedback, missing proprioception and less imagination about the motor control of the required SA.

Therefore, a method of creating artificial training data for the MA has been proposed in [CN14], namely Linearly Enhanced Training (LET). This method has been first applied to single finger activations to predict multiple finger activations. Therein, the data for MA has not been collected but has been artificially created through LET, based on the data of single finger activations. This technique has been also applied to hand and wrist movements, based on sEMG data [CBNvdS16].

LET is not a machine learning method, but a way of building an augmented training data set in order to improve the prediction capability of MA. In a technical view, LET could provide data for any type of regression algorithm but is used together with RR-RFF within this work. Some advantages of RR-RFF compared to other regression algorithms are exposed in [GBSG+14].

4.2 LET Method Description

4.2.1 Algebraic Interpretation

In the previous experiments, only SA were recorded and used to train the regression model. LET is a method which adds artificial training data to the input space. This artificial data consists of the combination of two SA, e.g. wrist flexion combined with power grasp. The resulting data is a linear combination of both SA clusters, using one ore more parameters to scale it. The scaling is either based on the coordinate origin or based on the center of the rest cluster, recorded at the rest position of the hand and wrist.
Given a SA dataset, which includes the training data of the rest cluster $\boldsymbol{X}_0$ and two SA clusters $\boldsymbol{X}_i$ and $\boldsymbol{X}_j$ in (4.1). Each training data cluster has a target vector associated to it, which is the ground truth for the specific action. For example, the target vector for the rest position is $(0, 0)$, for the action i it is $(1, 0)$ and for the action j it is $(0, 1)$.

$$D_{ij}^{\mathrm{SA}} = \{(\boldsymbol{X}_0, (0,0)), (\boldsymbol{X}_i, (1,0)), (\boldsymbol{X}_j, (0,1))\} \tag{4.1}$$

Given an extended dataset, including the MA cluster $\boldsymbol{X}_{ij}$, which is the according combination of these SA

$$D_{ij}^{\mathrm{MA}} = \begin{Bmatrix} ((\boldsymbol{X}_0, (0,0)), (\boldsymbol{X}_i, (1,0), (\boldsymbol{X}_j, (0,1)), \\ (\boldsymbol{X}_{ij}, (1,1)) \end{Bmatrix}. \tag{4.2}$$

Applying LET on the dataset in (4.2), training data for the MA can be artificially created by finding a function $F(\boldsymbol{X}_0, \boldsymbol{X}_i, \boldsymbol{X}_j)$.

$$D_{ij}^{\mathrm{LET}} = \begin{Bmatrix} ((\boldsymbol{X}_0, (0,0)), (\boldsymbol{X}_i, (1,0), (\boldsymbol{X}_j, (0,1)), \\ (F(\boldsymbol{X}_0, \boldsymbol{X}_i, \boldsymbol{X}_j), (1,1)) \end{Bmatrix} \tag{4.3}$$

Two similar models have been proposed in [NC16] to create such data, which is the single-α model function F_1 (4.4) and the multi-α model function F_m (4.5). The model function names are given by the number of their parameters which are optimized in the approximation of the MA cluster.

$$F_1(\boldsymbol{X}_i, \boldsymbol{X}_j) = \alpha_{ij}\ (\boldsymbol{X}_i + \boldsymbol{X}_j) \tag{4.4}$$

$$F_m(\boldsymbol{X}_i, \boldsymbol{X}_j) = \alpha_{ij}^{i}\ \boldsymbol{X}_i + \alpha_{ij}^{j}\ \boldsymbol{X}_j \tag{4.5}$$

To determining the single α_{ij} for the function in (4.4), a least squares problem is solved in (4.6) where the squared error terms between the true MA cluster and the artificial data set are minimized. The sample means are taken of each dataset for this calculation.

$$\alpha_{ij}^{*} = \underset{\alpha}{argmin} \left\| \bar{\boldsymbol{X}}_{ij} - \alpha(\bar{\boldsymbol{X}}_i + \bar{\boldsymbol{X}}_j) \right\|_2^2 \tag{4.6}$$

The result is the closed form solution of an optimum α_{ij}^*, given by

$$\alpha_{ij}^* = \frac{\bar{\boldsymbol{X}}_{ij}\ (\bar{\boldsymbol{X}}_i + \bar{\boldsymbol{X}}_j)^T}{(\bar{\boldsymbol{X}}_i + \bar{\boldsymbol{X}}_j)\ (\bar{\boldsymbol{X}}_i + \bar{\boldsymbol{X}}_j)^T}. \tag{4.7}$$

The same optimization accounts for the multi-α model, where two parameters instead of one parameter are optimized. The optimum α values are arranged in the solution vector $\boldsymbol{\alpha}_{ij}^*$, where the α-parameters for each SA cluster are arranged in $\boldsymbol{\alpha_{ij}} = \begin{bmatrix}\alpha_{ij}^i & \alpha_{ij}^j\end{bmatrix}$. The SA sample mean clusters are arranged in the matrix $\bar{\boldsymbol{X}}_{[i,j]} = \begin{bmatrix}\bar{\boldsymbol{X}}_i^T & \bar{\boldsymbol{X}}_j^T\end{bmatrix}$.

$$\boldsymbol{\alpha_{ij}^*} = (\bar{\boldsymbol{X}}_{[i,j]}^T\ \bar{\boldsymbol{X}}_{[i,j]})^{-1}\ \bar{\boldsymbol{X}}_{[i,j]}^T\ \bar{\boldsymbol{X}}_{ij}^T, \tag{4.8}$$

In the experiments of [NC16], the additional parameters of the multi-α model did not lead to a better performance in the online case. Therefore, the less complex single-α model has been chosen throughout this work. In the following, the LET method refers to the single-α model only.
Especially for FMG signals, the rest cluster is not located at the origin. A certain offset in each sensor channel is present due to the tightening of the bracelet. This causes a permanent force onto each sensor even at a relaxed muscle state. Therefore, the rest cluster position is accounted in the single-α parameter determination. Basically, each involved cluster center is shifted by the rest cluster center $\bar{\boldsymbol{X}}_0$ to calculate the α parameter relative to the origin, given by

$$\alpha_{ij}^* = \frac{(\bar{\boldsymbol{X}}_{ij} - \bar{\boldsymbol{X}}_0)\ ((\bar{\boldsymbol{X}}_i - \bar{\boldsymbol{X}}_0) + (\bar{\boldsymbol{X}}_j - \bar{\boldsymbol{X}}_0))^T}{((\bar{\boldsymbol{X}}_i - \bar{\boldsymbol{X}}_0) + (\bar{\boldsymbol{X}}_j - \bar{\boldsymbol{X}}_0))\ ((\bar{\boldsymbol{X}}_i - \bar{\boldsymbol{X}}_0) + (\bar{\boldsymbol{X}}_j - \bar{\boldsymbol{X}}_0))^T}. \tag{4.9}$$

4.2.2 Geometrical Interpretation

Figure 4.1 shows the hyperplane in a two dimensional view, which is expanded in the input space between the rest cluster $\boldsymbol{X}_0$ and both SA clusters $\boldsymbol{X}_i$ and $\boldsymbol{X}_j$. The cluster $\boldsymbol{X}_+$ is the cluster summation defined by

$$\boldsymbol{X}_+ = (\boldsymbol{X}_i - \bar{\boldsymbol{X}}_r) + (\boldsymbol{X}_j - \bar{\boldsymbol{X}}_r) + \bar{\boldsymbol{X}}_r = \boldsymbol{X}_i + \boldsymbol{X}_j - \bar{\boldsymbol{X}}_r, \tag{4.10}$$

where each sample is shifted by the mean of the rest cluster. The sample means of the rest cluster are arranged in the matrix $\bar{\boldsymbol{X}}_r = \mathbf{1}_{N_\mathrm{s}}\bar{\boldsymbol{X}}_0$, where $\mathbf{1}_{N_\mathrm{s}}$ is the N_s-dimensional unit vector. The cluster $\boldsymbol{X}_+$ is introduced to represent the diagonal line between rest cluster center and the assumption of where a MA cluster could be located. The cluster $\boldsymbol{X}_+$ is neither used for training nor for creation of the artificial data but provides a basis for the data enhancement process.
The calculation of the LET cluster $\boldsymbol{X}_\mathrm{LET}$ is a projection of the MA cluster $\boldsymbol{X}_{ij}$ onto the diagonal of the parallelogram. It is calculated through a simple scaling of the vectors in $\boldsymbol{X}_+ - \bar{\boldsymbol{X}}_r$, which can be rewritten as $\boldsymbol{X}_i + \boldsymbol{X}_j - 2\bar{\boldsymbol{X}}_r$.

There are two possible reasons for approximation errors of the artificial data, which are intrinsic properties of the single-α model. First, a large deviation of $\boldsymbol{X}_{ij}$ from the previously introduced hyperplane in perpendicular direction. This deviation cannot be further minimized as the projection of the artificial data needs to lie on that hyperplane. The second deviation lies in the same geometric plane of the hyperplane but in perpendicular direction to the diagonal of the parallelogram. This distance is denoted with $\bar{D}$. A further minimization is not possible as the projection needs to lie on the diagonal of the parallelogram.

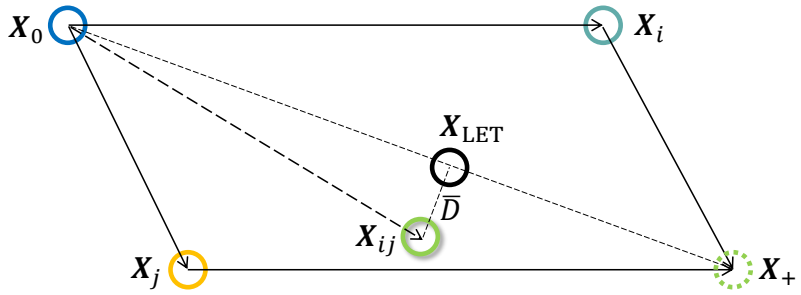

Figure 4.1: Geometrical interpretation of data enhancement based on two SA.

4.2.3 Training Data Enhancement

In this work, LET is adapted towards the different sensor input signals. This means that the LET procedure is applied independently to each sensor modality. Additionally, the rest cluster position is taken into account. Especially for FMG signals, the rest cluster signal values are located differently from the coordinate origin as a permanent force is applied onto the sensors, even if there is no activation executed by the user.
The LET clusters are determined individually for both sensor modalities in (4.11) with individual α-parameters. First, the sum of the SA clusters $\boldsymbol{X}_+$ is shifted to the coordinate origin, then scaled with the α-parameter and then again shifted by the rest cluster sample mean matrix $\bar{\boldsymbol{X}}_r$. The resulting LET cluster is then the composition of the individual LET clusters (4.12).

$$\begin{aligned} \boldsymbol{X}_{\text{LET}}^{\text{sEMG}} &= \alpha_{\text{sEMG}} \left(\boldsymbol{X}_{+}^{\text{sEMG}} - \bar{\boldsymbol{X}}_{r}^{\text{sEMG}} \right) + \bar{\boldsymbol{X}}_{r}^{\text{sEMG}} \\ \boldsymbol{X}_{\text{LET}}^{\text{FMG}} &= \alpha_{\text{FMG}} \left(\boldsymbol{X}_{+}^{\text{FMG}} - \bar{\boldsymbol{X}}_{r}^{\text{FMG}} \right) + \bar{\boldsymbol{X}}_{r}^{\text{FMG}} \end{aligned} \tag{4.11}$$

$$\boldsymbol{X}_{\text{LET}} = \begin{bmatrix} \boldsymbol{X}_{\text{LET}}^{\text{sEMG}} & \boldsymbol{X}_{\text{LET}}^{\text{FMG}} \end{bmatrix} \tag{4.12}$$

4.2.4 Combining Activations

The number of combinations between different actions is given by the binomial coefficient, where n is the number of actions and k is the number of actions to be

used for a single combination. In this work we address the combinations of two single actions only. This limits the approach to a manageable complexity instead of additionally combining even three ore more actions. The number of possible combinations is given by

$$\binom{n}{k} = \prod_{j=1}^{k} \frac{n+1-j}{j} \tag{4.13}$$

and for the case of combining only pairs of different actions ($k = 2$), it simplifies to

$$\frac{n(n-1)}{2}. \tag{4.14}$$

For a set of five SA, a number of 10 MA is obtained. As the wrist flexion and extension lie in opposite directions on the same DOF, a combination of them is not useful. The same holds for the wrist pronation and supination. In general, activations which lie on the same DOF in the target space can be excluded from the set of possible combinations. This leads to a set of eight sensible combinations, namely *fle-pro, fle-sup, fle-gra, ext-pro, ext-sup, ext-gra, pro-gra, sup-gra.*

4.3 Design of the Test Setup

The biosignals sEMG and FMG shall be acquired at defined force levels of the wrist and hand. This is done to make sure that SA as well as MA are trained at a certain force level, where the forces of both MA components are comparable to the SA forces. Therefore, force-torque (F/T) sensors need to be employed to measure the resulting forces and torques. At the same time, the wrist and hand shall be fixated in a constant position. This fixation brings the experiment closer to the amputee case where a real hand and wrist joint is missing and therefore no movement is possible. In such case, there is no visual feedback about the hand state.
A measurement of the human wrist flexion and extension torques as well as simultaneous measurement of the wrist pronation and supination torques is required. Additionally, the simultaneous measurement of the grasp force exerted by the fingers except the thumb is necessary. As the flexion and extension as well as pronation and supination lie on opposed torque directions, each group can be measured with one sensor axis. For the wrist DOFs, a sensor with two torque axis is required, where the human hand is attached to, while the finger movement is unrestricted. Hereby, the wrist adduction and abduction are not in the focus of this experiment, but also measured for future analysis. Further, one independent sensor with a force axis to measure the joint flexion force of the four fingers is required.
To select the right sensors, the maximum occurring wrist and hand torques and forces need to be investigated. After selecting a wrist sensor, which fulfills the limits, a splint need to be designed where the wrist can be fixated to transfer the torques and forces to the sensor. Furthermore, this splint is the mechanical footing

of the grasp sensor, where the four finger tips can be pressed onto the force axis of the grasp sensor. An independent and simultaneous execution of all measured DOF shall be possible. Figure 4.2 shows a schematic draft of the test setup.

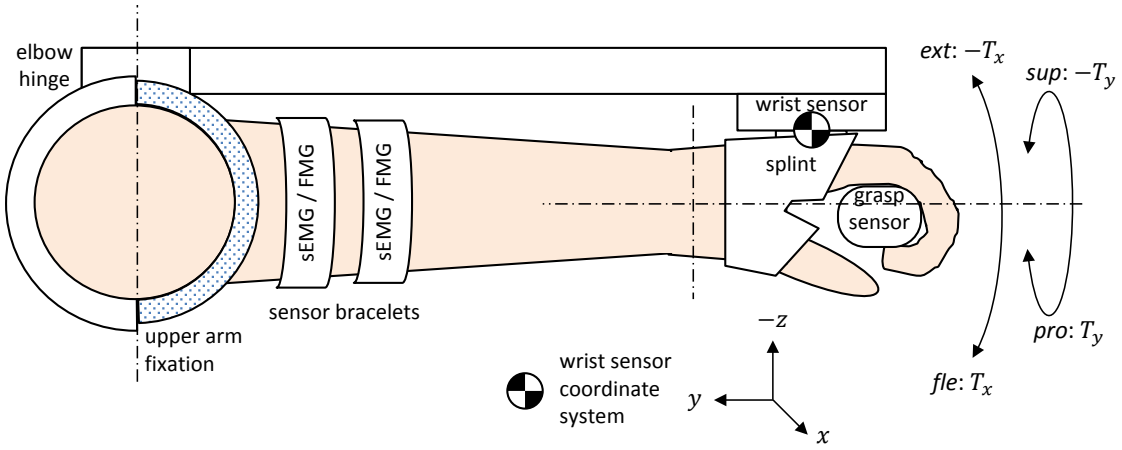

Figure 4.2: Test setup schematic. The setup is fixated at the upper arm with Velcro straps and at the hand using a rigid splint, which is mounted on the wrist sensor. The wrist actions are related to the sensor measurement axis

4.3.1 Mechanical Design

An adaptable length between elbow joint and the dorsal mounting of the hand is required. This is necessary to fit the test setup onto individual forearm lengths. Therefore, a telescope element is embedded in the support structure for the forearm. Further, a free movement of the elbow joint is desired, which prevents the user from introducing undesired forces or torques into the mechanical system. A hinge is used to connect the support structure of the forearm with the support structure of the upper arm. Both rotation axis of the human elbow joint as well as the test setup hinge need to match. The fixation on the upper arm consists of three padded Velcro straps which allow an adaption to different subjects.
When fixating the hand onto the forearm support structure, it is required to allow free finger movements to measure the grasp force independently of other wrist torques. A splint has been formed, using a thermoplastic material. This material can be formed manually when heating it above 65 °C and stays in the desired shape when cooled down. Some subjects were consulted such that a fit of the splint to different hand sizes and shapes is possible. After some iterative shape improvements, a good fit of the splint on different subjects has been achieved.
As the test hardware has a weight around 2 Kg, wearing it would require to strongly actuate the biceps muscle to keep the forearm in a horizontal position. A horizontal position is also desired throughout the experiment. Other muscles would also be actuated other than the forearm and hand muscles to bear the weight of the setup.

This would strongly influence the measurement and induce fatigue in the subject throughout the experiment. Therefore, the hardware need to be weight compensated which can be achieved through the gravity compensation capabilities of a robot.
Beside compensating the weight of the hardware, a free suspension is desirable as it prevents the subject from introducing forces and torques if the setup would be rigidly attached to the environment. In the free suspension case, any linear or angular movement above the elbow hinge should be without effect on the measurements of the wrist and grasp sensors.
Another advantage of using a robot for gravity compensation is the pose measurement obtained from the robot. The position and orientation of the test setup can be measured at any time and later on analyzed. This could reveal a relation between the characteristics of the sensor signals and different arm poses. It is assumed that the sEMG signals at a relaxed forearm change slightly on different upper arm positions and elbow angles. This effect is limited by the allowed movement range the experimenter gives to the subject. The effect of different upper arm positions and elbow angles might be stronger on the FMG signals, as these factors influence the skin to muscle constellation in the forearm, even if there is no muscular contraction. This effect need to be observed during the experiment.

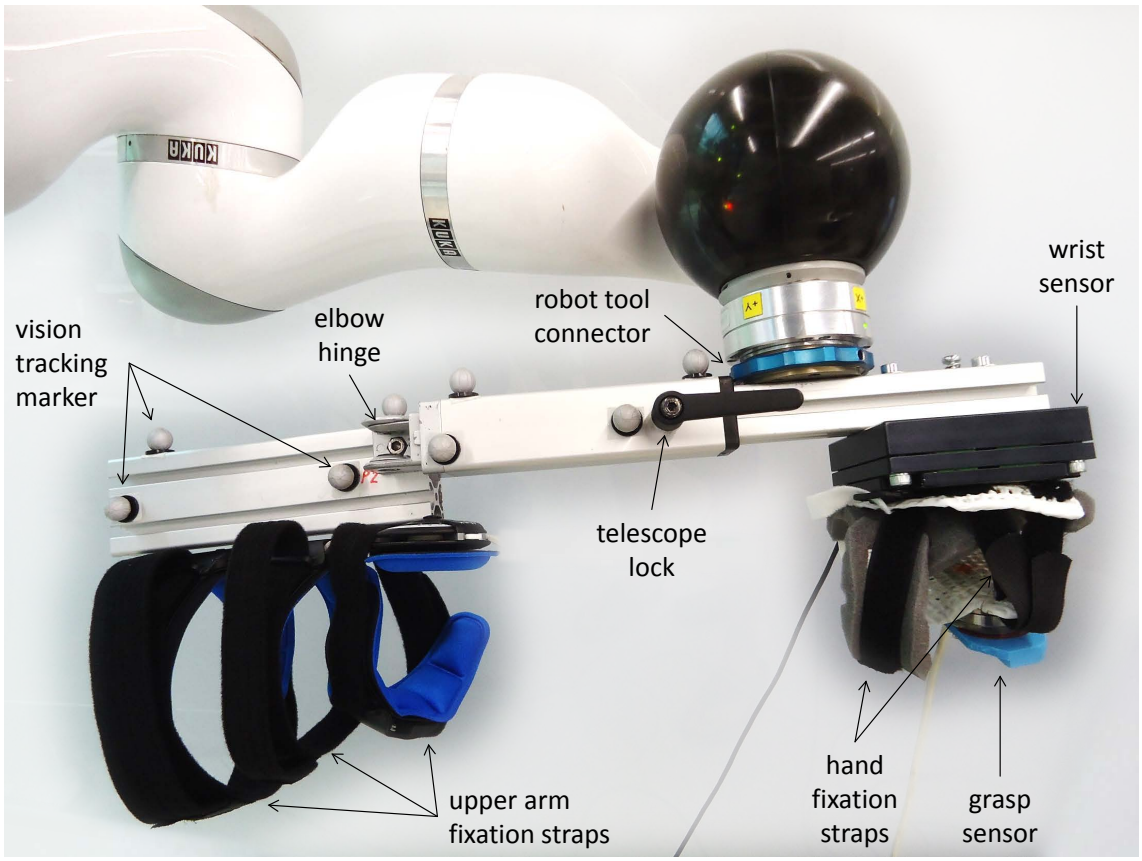

Figure 4.3: Test setup module description

4.3.2 Maximum Forces and Torques

As a basis for the mechanical design and as selection criterion for the F/T sensors, the maximum occurring torques on the human wrist and the grasp force are investigated. Despite the fact that wrist pronation and supination are performed by a rotation of the *Ulna* around the *Radius* in the forearm, the forces related to this actions are still regarded as wrist forces in this work. The maximum and minimum values among the subjects of different studies found in literature are summarized in Tab. 4.1. Especially the grasp force has a large variation over different subjects and strongly depends on the kind of grasp and the geometry of the grasped object. In this application, the four fingers are used to press against the object towards the palm. The thumb force can be used only marginally in this situation. Two tubular grasps are found in literature with differing grasp object diameter, taking the maximum value as a benchmark for the sensor selection.

Table 4.1: Maximum and minimum exerted force/torque at maximum voluntary contraction (MVC) on the human wrist. *max./min. over 10 healthy subjects, $^{+}$mean over 20 healthy subjects.

Action	Max.	Min.	Ref.
wrist flexion	11.9 Nm	8.0 Nm	[YYK^{+}15]
wrist extension	5.5 Nm	4.6 Nm	[YYK^{+}15]
wrist pronation	13.5 Nm	9.0 Nm	[OG02]
wrist supination	16.2 Nm	10.9 Nm	[OG02]
tubular grasp*	1047.95 N	101.12 N	[NCWA12]
tubular grasp^{+}	251.0 N @ 50 mm tube	73.3 N @ 110 mm tube	[RN93]

4.3.3 Sensor Selection

The selected force/torque sensors need to provide at least a measurement range which cannot be exceeded by the strongest subject but must not be too insensitive. Table 4.2 summarizes the data of the selected sensors, further termed as grasp sensor and wrist sensor.

Table 4.2: Sensors properties of the grasp sensor (ATI Mini45) and the wrist sensor (Space Control OFTS).

Property	ATI Mini45	Space Control OFTS
Sensor technique	strain gauge	optical
Interface	analog 0..5 V via NI-DAQ	serial (RS232)
Resolution	$F = 0.125$ N	$F = 0.1$ N, $T = 0.01$ Nm
Sample Rate	50 Hz	50 Hz
Used DOF	1 force (F)	1 force (F), 2 torque (T)
Maximum Values	$F_z = \pm 580$ N	$F_{x,y,z} = \pm 400$ N, $T_{x,y,z} = \pm 20$ Nm

The grasp sensor is small enough in its diameter and height to fit it into the palm area of the splint. When the fingers are flexed, this area is restricted even more. The sensor height is limited, such that a finger flexion of 180 ° relative to the palm surface is possible. To properly actuate the sensor on its force axis, a support block for the fingers has been designed (Fig. 4.4). This block is mounted on top of the grasp sensor and has a indentation for the fingers. On the other side of the sensor, a Velcro strap is attached. The counterpart of the Velcro strap is glued onto the palm area of the hand splint. This allows an adaption of the sensor position relative to the splint, which is required for different finger lengths.

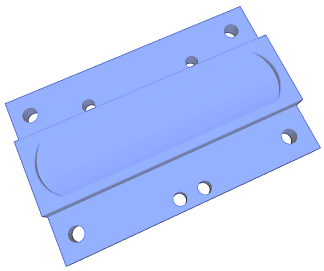

Figure 4.4: Finger block for grasp sensor.

The wrist sensor comes with 6 DOF F/T axis. It need to be clarified that measuring the forces and torques of the required actions is just an approximation. This is mainly caused by the geometrical properties of the setup design. For instance, the wrist flexion and extension are measured as a torque, where the measured torque axis is defined by the coordinate origin of the F/T sensor. The anatomical center of rotation of these actions is in the wrist joint. This leads to a deviation in the measured torque. The same accounts for pronation and supination, where the anatomical center of rotation lies not in the sensor coordinate origin but somewhere in parallel and in between the forearm bones *Radius* and *Ulna*. Therefore, the measured torques must not be treated as accurate anatomical values but as a reference for the data acquisition process.

4.4 Force Related Data Acquisition

The purpose of this experiment is a sEMG and FMG data acquisition at a force level of 40% of the maximum voluntary contraction (MVC) while the wrist of the subject is fixed in the test setup. Data of SA and MA is recorded while a free movement of the forearm, the upper arm and the elbow is possible to some extend.

4.4.1 Definition of Force Levels

Each action is related to a channel of one of the two sensors, stated in Tab. 4.3.

Table 4.3: Mapping between actions and F/T sensor channels.

Action	Sensor	DOF	Symbol
fle	Space Control OFTS	T_x	F_1
ext	Space Control OFTS	$-T_x$	F_2
pro	Space Control OFTS	T_y	F_3
sup	Space Control OFTS	$-T_y$	F_4
gra	ATI Mini45	$-F_z$	F_5

In the following and for the sake of simplification, all forces or torques are termed as forces. In the beginning, the MVC forces are required to obtain a reference force for the training.
First, the maximum force of each SA is recorded where the subject is instructed to apply the MVC of the required action. After the subject signalizes to be in this state, the force is captured. The required SA are again *fle, ext, pro, sup, gra*. These maximum values are termed $\hat{F}_i$ for each action $i \in A = \{1, 2, ..., 5\}$ from Tab. 4.3. The normalized force of activation i is obtained by

$$\tilde{F}_i = \frac{F_i}{\hat{F}_i}. \tag{4.15}$$

In the next stage, the maximum force of each MA needs to be determined. Three approaches were tested in a preliminary experiment to capture and visualize the MA force levels to the subject and the experimenter.
The first approach uses only the maximum forces of the SA to use a common normalization for SA and MA. Hereby, all available force levels were shown to the subject, as shown in Fig. 4.5 a). This approach has two disadvantages: First, displaying all six force levels at once leads to increased mental demand and raises the error probability during the data acquisition. This has also been confirmed by the test persons using this kind of force display. Second, the physical properties of the combined muscle activation may lead to a different perceived MVC, compared to the MVC of both SA.
The second approach displays a single force level for either a SA or a MA, shown in Fig. 4.5 b) on the left. Hereby, the subject applies the MVC in the MA and the maximum forces of both involved SA are captured independently, denoted as $\hat{F}_{[i],j}$ and $\hat{F}_{i,[j]}$. The subscripts $i \in A$ and $j \in A$ refer to both involved actions of the combination and the square brackets indicate what action the force is related to. Now, the sum of both normalized forces is denoted as

$$\tilde{F}_{i+j} = \frac{1}{2} \cdot \left(\frac{F_{[i],j}}{\hat{F}_{[i],j}} + \frac{F_{i,[j]}}{\hat{F}_{i,[j]}} \right). \tag{4.16}$$

Further, a second force indicator is used to display the sum of all unwanted forces caused by unwanted activations (UA), shown in Fig. 4.5 b) on the right. An unwanted force is each force from the considered DOF in Tab. 4.3, which is not related

to a specific SA or MA. The respective force i for SA or i, j for MA are excluded to obtain a set of unwanted forces. Furthermore, all actions which lie on the opposite side of the DOF as the required actions also need to be excluded. Otherwise, their negative force values caused by the opposite activation on the DOF would contribute to the UA. The opposite action is given with $o \in A$. If the performed action has no opposite action as for example *gra*, the opposite action o is an empty value. The level of the unwanted forces is then defined by the mean over all normalized unwanted forces during the acquisition of a SA (4.17) or a MA (4.18), where $|...|$ denotes the cardinality of a set.

$$\tilde{F}_i^{\mathrm{UA}} = \frac{1}{|A \setminus \{i, o\}|} \sum_{n \in A \setminus \{i,o\}} \tilde{F}_n \tag{4.17}$$

$$\tilde{F}_{i,j}^{\mathrm{UA}} = \frac{1}{|A \setminus \{i, j, o\}|} \sum_{n \in A \setminus \{i,j,o\}} \tilde{F}_n \tag{4.18}$$

The advantage of this approach is that the MVC related forces are directly drawn at the execution of the MA instead of using the maximum forces captured for both of the related SA. For a subject, it is easy to observe only two force levels at one time but it lacks the information about the independent forces of the involved DOFs. The test datasets recorded with this force display showed larger scattering of the sensor data among the repetitions of a certain action. This leads to the assumption that the subjects were unsure about their MVC for MA.

For the third approach, the advantages of both previous approaches were fused. The GUI in Fig. 4.5 c) adapts to each case if a SA or a MA needs to be captured. The MVC of the SA are captured and only the actual force level is displayed. The MVC forces of MA are captured during execution of the MA but their SA components are shown independently at the bars MA_1 and MA_2. The normalized values after capturing the MVC for each component i and j of the MA are calculated as

$$\tilde{F}_{[i],j} = \frac{F_i}{\hat{F}_{[i],j}} \; ; \qquad \tilde{F}_{i,[j]} = \frac{F_j}{\hat{F}_{i,[j]}}. \tag{4.19}$$

The bar at the far right in Fig. 4.5 c) shows again the UA. After testing this approach in a preliminary experiment, a trade off between mental demand and the quality of the acquired data has been found. Therefore, approach three is further used throughout the experiment.

After capturing the MVC force of all SA and MA, all force level bars can be normalized to 1. In the following training stage, the subject can perform all of the activations at a desired level of 40% of the MVC. This level is marked by the dashed line in Fig. 4.5. The force level of the UA helps the subjects to avoid unwanted activations as they can try to minimize it before the data acquisition of each activation.

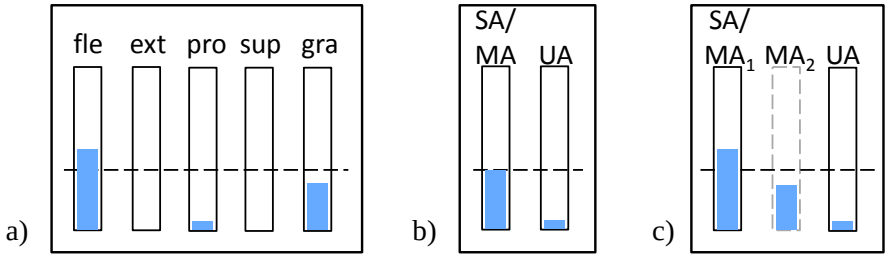

Figure 4.5: GUI drafts for force capturing and display with dashed line to mark 40% of MVC. Example shows MA *fle-gra*. a) approach one with individual force levels. b) approach two with a force level bar for SA or MA and another bar for UA. c) approach three with one bar for SA or two bars for MA depending on purpose and one bar for UA.

4.4.2 Preliminary Cluster Analysis

A preliminary test has been conducted to analyze the training data captured with the novel test setup. Three repetitions of all activations have been recorded while the test setup was mounted on a tripod. The cluster variances and the separability between the clusters has been inspected, using principal component analysis (PCA). Both sEMG and FMG data is stacked into the same input space for the PCA. The first three plotted principal components explain 90% of the normalized variance of the 20 sensor channels. See Fig. 4.6 on the left for all labeled samples of each activation and on the right all cluster centers. A MA cluster on the right can be found through the connection lines to both SA clusters.

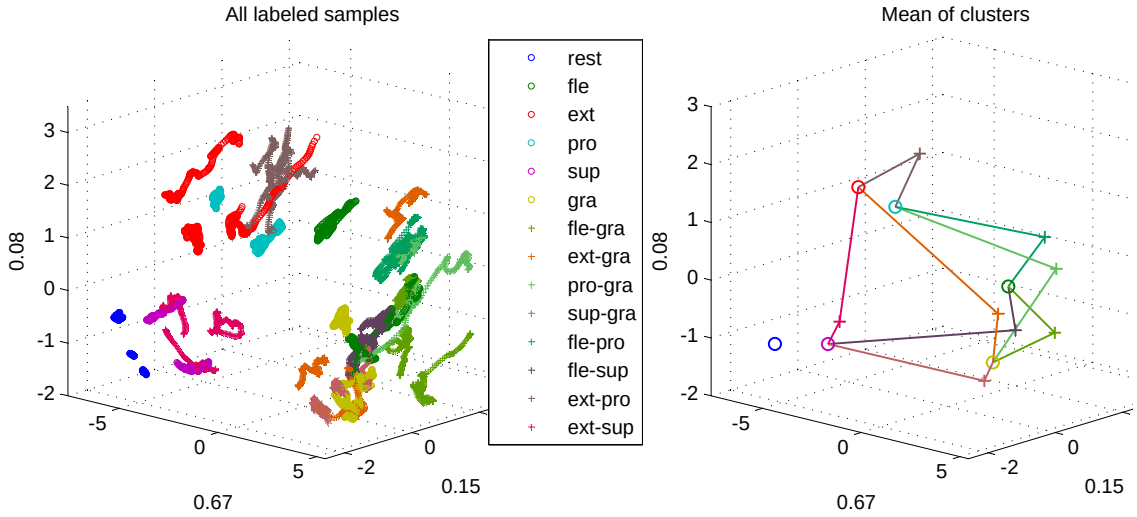

Figure 4.6: Preliminary Cluster Analysis. Left: PCA of all labeled samples. Right: PCA of all cluster centers, where each MA is connected with lines to both related SA

The performance of the regression model depends on the separability of the different clusters, which prevent cross-activations of unwanted DOF during the prediction. For some activations the repetitions show a large spreading. In such cases the subject could have been unsure with the required training activation and hence shows poor repeatability. If the cluster variances are high, the subject may have had problems holding the required activation. The use of the force levels may have been challenging for the user. This effect is further influenced by the sEMG signal characteristics, where further motor units are recruited during the isometric contraction at the same force level [MAB+10]. As a result, the sEMG signal envelope decreases.
On the right side of both plots, all SA and MA clusters related to *gra* are placed close to this action, which shows bad cluster separability and could influence the model negatively. The effect of such cluster constellation needs to be assessed in an online experiment.
In conclusion, the test setup shall be used for a data acquisition experiment at desired force levels. The cluster means of MA are approximately located in the angle space between both related SA cluster means. These are explainable locations of the MA clusters in the input space as their training data is built of both related SA.

4.4.3 Experiment Description

Each subject received an oral explanation and a written consent form. As the experiment requires an interaction between a human and a robot, safety instructions were made. The system is equipped with two independent emergency switches. One realized as a push button, held by the experimenter during the experiment. Another realized as a foot switch with spring mechanism, which need to be pressed permanently to enable the control of the robot.
The provided robotic system is used as a haptic input device for teleoperation, called *HUG* [SHH+16]. It is equipped with a chair for the user and two light weight robot (LWR) arms. These arms can be attached to the operators hands and enable force feedback while the user can freely move these arms in space. In this experiment, the functionality of only one arm is used. The main task of the arm is to bear the weight of the test setup while the gravitational force of the connected system is compensated. This allows free movement of the test setup in six DOFs with minimal muscular forces. If the user leans against the test setup, it drifts away. This behavior reduces the transfer of external forces and torques into the test setup, which are undesired during the data acquisition. The system configured for this experiment is shown in Fig. 4.7.
Further benefits of the *HUG* system are the information about the six DOF Cartesian pose of the test setup and the optical tracking system, located on a frame on top of the *HUG*. This tracking system is used to obtain the poses of both segments of the test setup, and subsequently to compute the angle between the forearm and upper arm. This angle is directly related to the elbow angle of the subject. Using

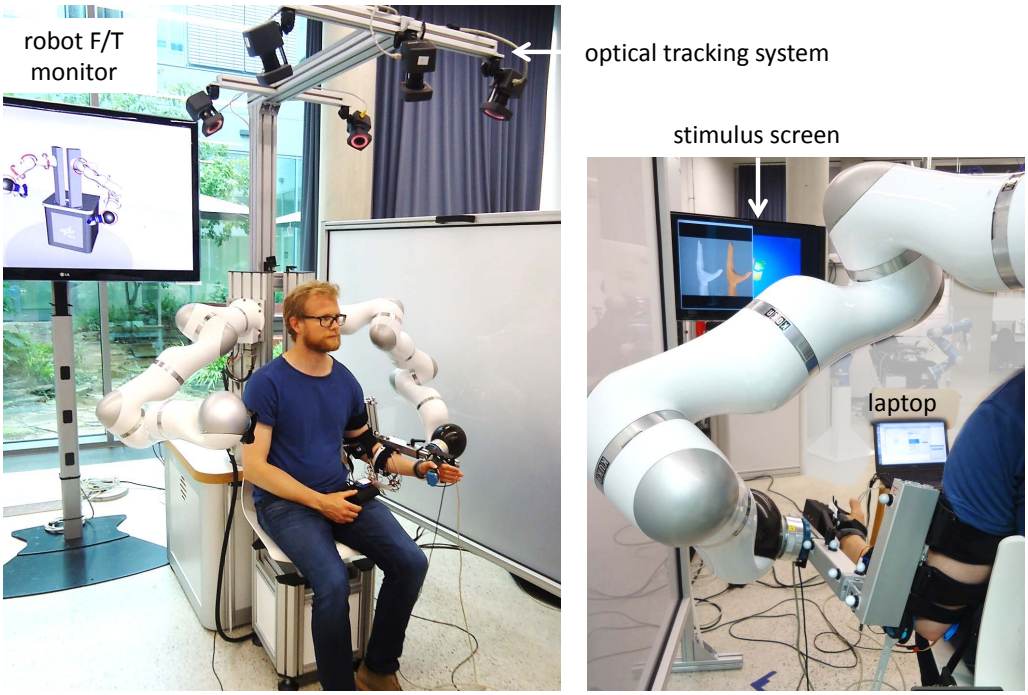

Figure 4.7: The HUG system configured for the experiment. Left: system overview. Right: view over the left shoulder of the subject onto the stimulus screen.

the poses and the elbow angle information, future analysis become possible, e.g. how this properties influence the training data. An overview of the system modules can be found in Fig. 4.8, where the software *interactiveMyocontrol* is used to process all data during the experiment.
In the beginning of the experiment, the subject sits on the chair between the robot arms, as in Fig. 4.7. The subject's arm is held in place by the Velcro attachments of the upper limb structure. The straps are tightened such that a comfortable fit is achieved and the axis of the elbow joint is located at the foam pad at the elbow hinge. The wrist is inserted into the wrist fixation and tightened with three Velcro straps. The position of the grasp sensor is adjusted to the subject's finger poses to enable a proper grasp onto the sensor plane.
The sensor positions are shifted on both bracelets such that they are equidistantly distributed on the circumference of the subject's forearm. The fixation and tightening characteristics are taken from the previous experiments. Same accounts for the sensor configuration, where a number of 10 sEMG and 10 FMG sensors is used, arranged in an alternating order on both bracelets.
The subject sits in front of a screen, which shows a stimulus of the required activation and the previously described force level GUI. At the start of the data acquisition, the subject steps on the emergency foot switch to bring the robot into gravity compensation mode. First, the *maximum force stage* is entered, where the maximum forces of all activations are recorded. Second, the *training stage* is entered in which

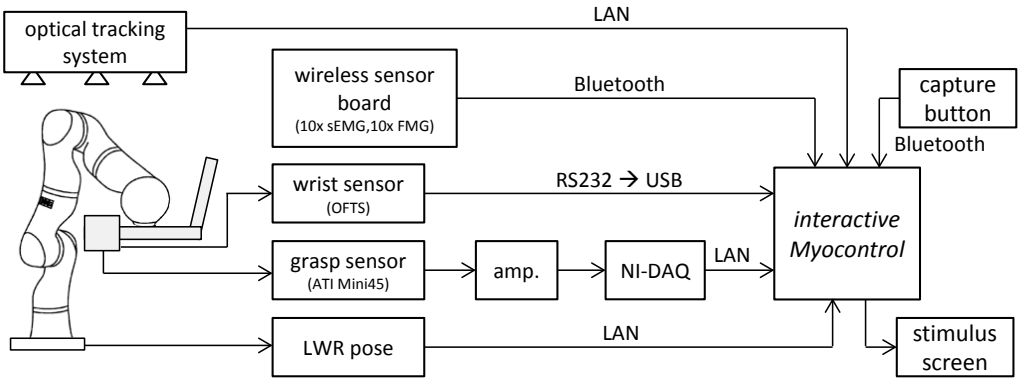

Figure 4.8: Experiment system block diagram (robot image source [BGK+11]).

the subject trains all activations with five repetitions at 40 % of the MVC. The subject gives a command to the experimenter to capture data whenever she/he feels close to the required force level. The experimenter captures data only if the force levels are in an acceptable range of the required ones. If the force differs strongly from the required level, the experimenter gives further improvement tips. Whenever a required action is unclear to the subject, the experimenter performs the action beside the subject. At the same time, the experimenter can initiate the capturing by using a wireless bluetooth button. A break from the procedure is possible after every repetition set by releasing the foot switch. The duration of the experiment is approximately 1 h. The data acquisition takes 35 min. The rest of the time is required for safety instructions and configuration of the setup for the subject.

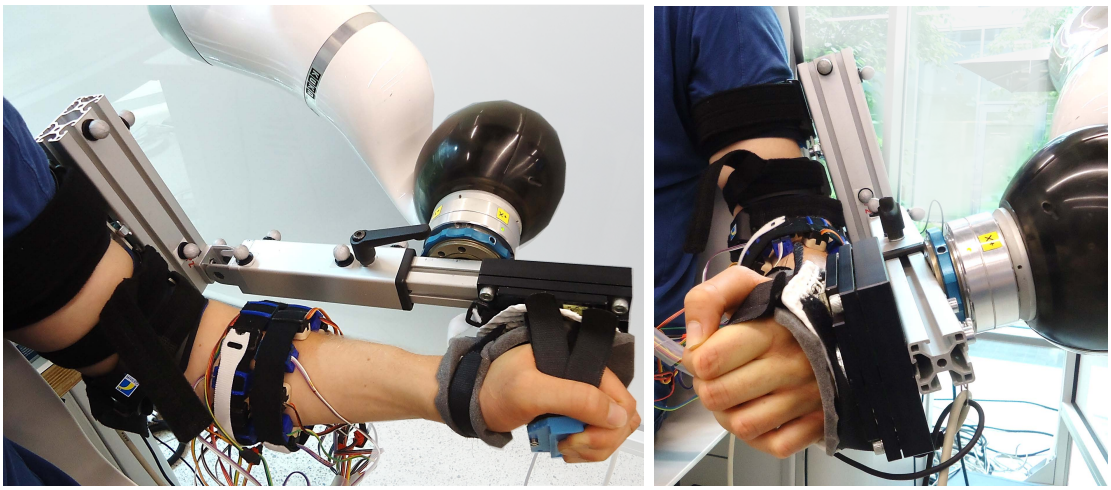

Figure 4.9: Test setup with the left arm of a subject attached to the robot. The subject's forearm is equipped with two sensor bracelets.

4.4.4 Data Analysis

Consistent and Problematic Training Sets

The following plots show one example for a consistent training data set and some example datasets where different problem classes occur. This analysis discusses these problem classes, comparing the data from different subjects and activations. The datasets were picked such that the occurrence of the problem can be seen clearly. Some of these problems could be caused by the subject due to a wrong understanding of the experiment, through inattention or indisposition with the robot. This data analysis shell help to understand which effects influence the training data and hence the cluster constellation.
For each plot, a subject and the training data of a MA with its related SA has been selected. Additionally, the related LET data has been inserted into the training set, using the α-parameter of the specific subject and activation. The LET cluster location and its deviation to the MA cluster shows how well LET approximates the training data. The following plots show, how the problems of the real training data affect the LET cluster.
A principal component analysis (PCA) has been applied to each training set in the 20-dimensional input space of 10 sEMG and 10 FMG sensors. The first two principal components were used for plotting. The normalized explained variance is plotted as axis labels. The clusters are labeled with the related activation. On an additional plot, the cluster centers calculated by the sample mean of each activation and of the LET cluster is shown. It is emphasized that the explained variance of the two dimensional plots gives just a vague impression of the cluster constellation. A poor cluster separability in a 2-D plot can be still a good training set as the data is spread along 20 dimensions in reality.

Consistent Training Set

Figure 4.10 shows a consistent data set in terms of cluster locations and repeatability. The repetitions for each activation lie in dense order and different activations are properly separated. The repetitions of the rest cluster X_0 are quite dense. Both SA clusters X_i and X_j are properly separated. The MA cluster X_{ij} lies between both SA clusters. The LET cluster X_{LET} shows a good approximation of X_{ij}. The distance of all clusters to the rest cluster X_0 is similar. This is not mandatory for good training data but shows that the execution of each SA caused similar signal amplitudes. The angle between the vectors $\overrightarrow{X_0X_i}$ and $\overrightarrow{X_0X_j}$ is distinct.

Scattered Repetitions

In Fig. 4.11, the repetitions of both SA clusters (X_i and X_j) as well as the MA cluster X_{ij} shows a strong scattering over the fife repetitions. This results also in a strong scattering of X_{LET}. Even the rest cluster X_0 shows this behavior. The subject might

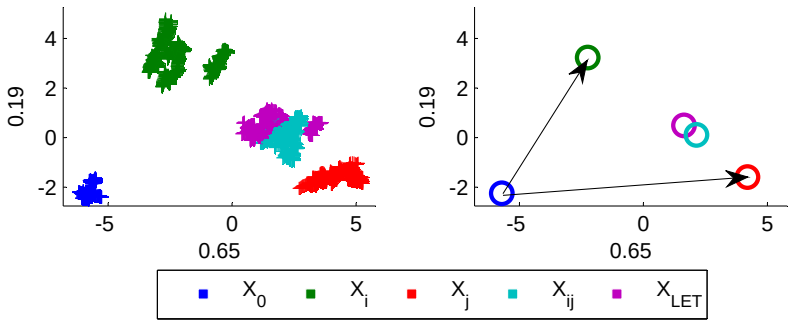

Figure 4.10: Example of a consistent training set (*ext-gra*).

have changed the forearm pose and the elbow angle during the experiment. Looking at the location of the cluster centers, the training data might be still purposeful. In such case, the distribution of the repetitions might even contribute to a better generalization of the regression model for similar input signals around the cluster centers.

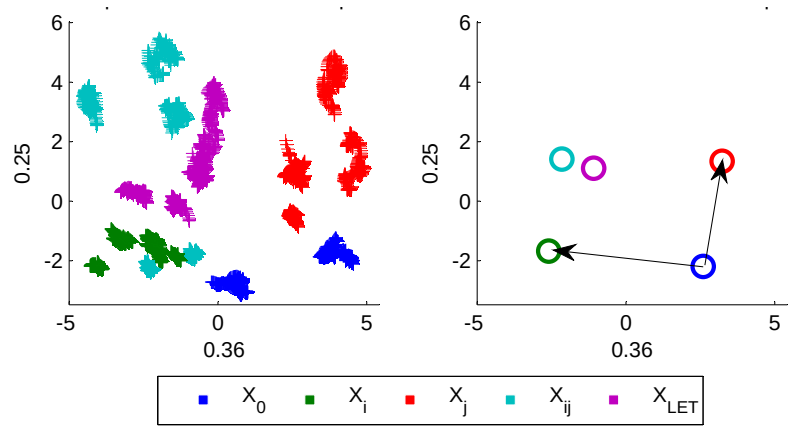

Figure 4.11: Training set with poor repeatability (*ext-sup*).

Cluster Separability

Figure 4.12 shows an example for a poor cluster separability. The dataset is from the activation of *sup-gra*. The cluster for *sup* (X_i) lies almost on top of X_0. On the other hand, the cluster for *gra* is strongly separated from X_0. In this case, the signals for *sup* were so weak that a clear distinction from the rest position is not possible. The regression model will be overly sensitive for signals close to the rest position. This will often result in an unwanted activation of *sup*. This effect might be again caused by the anatomical properties of the muscles relevant for *sup*. The sensed signals of muscles lying deeper beneath the skin are generally weaker.

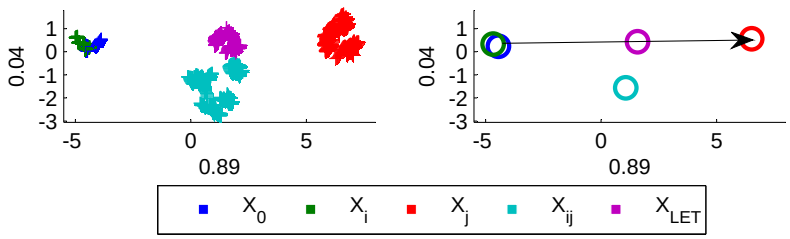

Figure 4.12: Training set with poor cluster separability (*sup-gra*).

Cluster Alignment

Figure 4.13 depicts a dataset, where the SA clusters X_i and X_j are approximately in line with X_0. The dataset shows *ext-sup*, which are the actions i and j respectively. This cluster constellation could lead to interference between i and j. The assumption is that the intermediate signals between rest position X_0 and X_i are approximately produced on a line between those clusters. When proportionally increasing the level of activation for action i, signals will be produced which come close to X_j. This again leads to an unwanted activation of action j in the regression model. This problem affects also X_{LET}, which lies approximately in the same line as described before. Only X_{ij} shows a noticeable distance to this line.

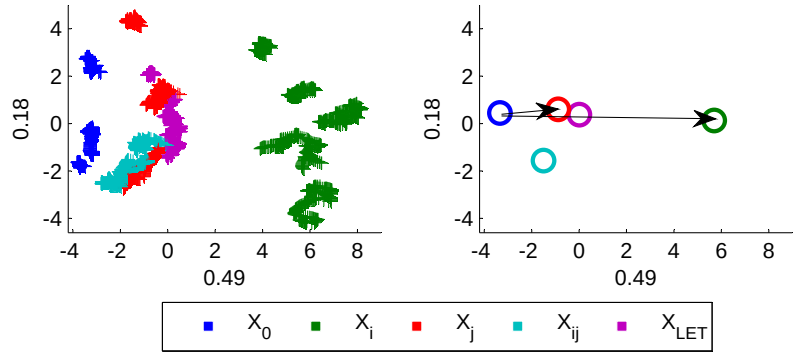

Figure 4.13: Training set with poor cluster alignment (*ext-sup*).

Blurred Clusters

In Fig. 4.14, the cluster X_j is remarkably blurred towards X_0. This has a direct effect on X_{LET} as it is a linear combination of X_i and X_j. This blurring might be caused by a too early or a delayed muscle contraction of the subject during the data recording. The activation needs to be executed during the whole time the stimulus on the screen is shown. The plot indicates that the subject released the activation before the data recording was finished and returned to the rest position. The activation shown here is *ext-gra*. The cluster centers show a good constellation

and separability. As the amount of blurred data is small compared to the whole cluster, the resulting error might be marginal in the regression model.

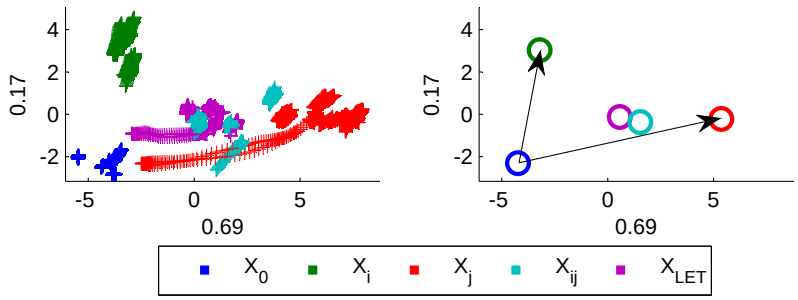

Figure 4.14: Training set with a blurred cluster (*ext-gra*).

Approximation of LET Set

Figure 4.15 shows an example of a bad approximation of the LET set towards X_{ij}. The effect is caused by the location of X_{ij}, which is much closer to X_j than to the middle of both SA clusters. Shown is data of *fle-gra*. This does not imply that the subject trained the MA *fle-gra* wrongly. It just shows that through the natural properties of the LET method, a closer approximation is not possible as the LET cluster is always a linear combination of both SA clusters. For MA clusters, which lie far from this linear combination vector family, it is the best possible approximation using LET. This plot gives an impression that in some cases, LET can correct errors of wrongly trained MA clusters. In other cases, the approximation restrictions of LET cause an additional error compared to the MA cluster. This is mostly dependent on the subject, his/her experience with such data acquisitions and the quality of training data he/she produces.

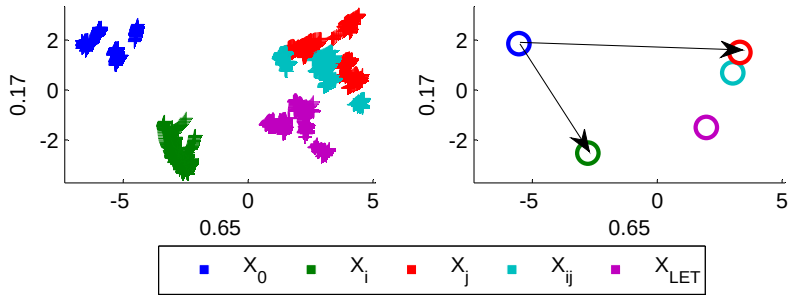

Figure 4.15: Training set with a bad approximation of the LET cluster (*fle-gra*).

In conclusion, it must be emphazized that not the whole information included in the training data can be explained by its variance. As the PCA is based on the variances of the data, it can also give a wrong impression about a dataset. Furthermore, the

variances of each action cluster extend mostly on a line between rest cluster and their full activation. This is caused by the subjects, when they try to hold a constant force level but vary around this point. As other metrics have failed so far to describe the quality of a dataset or of its single clusters, a PCA is still the method of choice to assess a dataset in the input space. How the quality of a dataset influences the prediction is so far only measurable in an online experiment. Further metrics for the dataset assessment in the input space as well as for the model prediction are currently investigated in this research group.

4.4.5 Parameter Selection

Data has been collected from 10 subjects over five repetitions. Some subjects gave the impression that they are unsure about the given stimulus in the first round of the five repetitions. It can be assumed that the rate of misinterpreted to properly interpreted stimuli is higher in the first repetition round than in the following rounds. The confidence of the subject should rise after the first repetition round when the procedure is already known. Therefore, the first round has been excluded from the parameter selection process.

The following data comes from the repetitions two to five. The first repetition is used to "train" the subjects on the system and at the same time improve the sensor fit on the forearm. Again, sweating and sensor displacement influences the sensor signals. Letting the sensor settle for a while is recommended before any data acquisition.

The boxplots in Fig. 4.16 show the calculated α-parameters for three different modes. A common α-parameter for all input dimensions and two independent α-parameters for the input dimensions of sEMG and FMG.

Table 4.4 reports all determined parameters, using the median over the subjects for each MA. The interquartile range (IQR) is reported in parenthesis. The median has been chosen as it is less sensitive to outliers. As the mental demand during the experiment is assessed as high, outliers may easily occur.

Table 4.4: Medians of alpha parameters among 10 subjects with interquartile range (IQR) in parenthesis

MA	common	sEMG	FMG
fle-gra	0.628 (0.097)	0.568 (0.185)	0.745 (0.164)
ext-gra	0.623 (0.221)	0.572 (0.231)	0.783 (0.093)
pro-gra	0.636 (0.130)	0.581 (0.142)	0.780 (0.340)
sup-gra	0.638 (0.321)	0.661 (0.295)	0.700 (0.466)
fle-pro	0.557 (0.157)	0.518 (0.112)	0.614 (0.404)
fle-sup	0.568 (0.280)	0.453 (0.288)	0.698 (0.436)
ext-pro	0.679 (0.736)	0.696 (0.807)	0.477 (0.202)
ext-sup	0.501 (0.449)	0.496 (0.481)	0.548 (0.101)

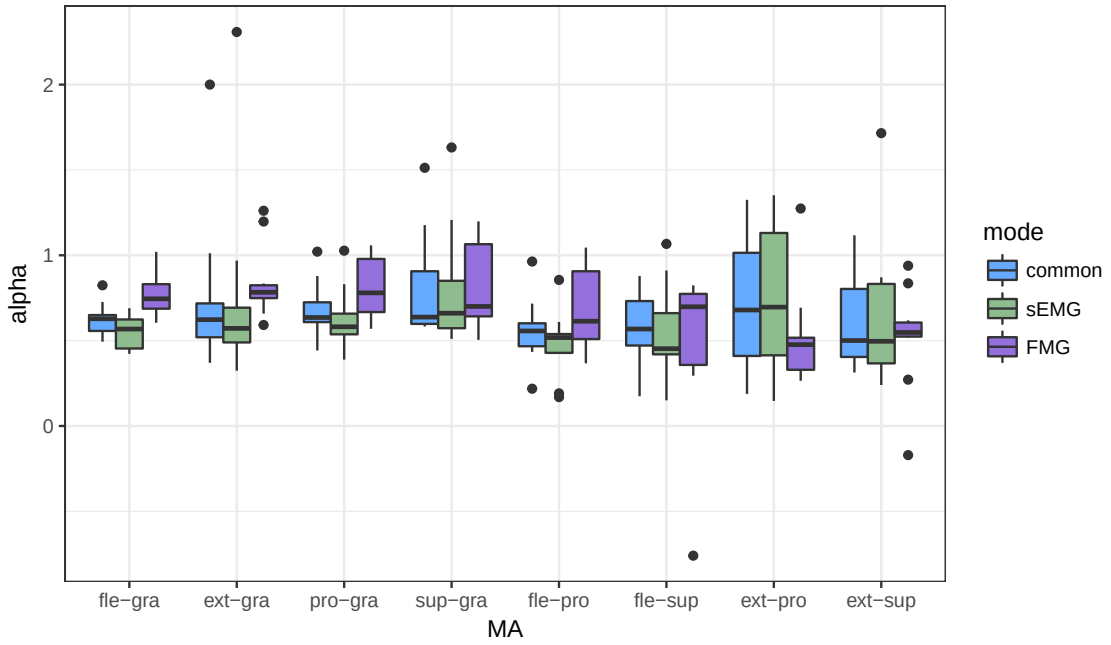

Figure 4.16: Boxplot of alpha parameters for each MA over 10 subjects

On average, the alpha parameters for sEMG are 6.05% smaller and the alpha parameters for FMG are 11.20% higher relative to the common alpha parameters. The alpha parameters for FMG are in average 19.98% higher than the alpha parameters for sEMG. As there is a remarkable difference in the parameter values for sEMG and FMG, it can be beneficial to create the LET data independently for each modality.

4.4.6 Force Ratios between SA and MA

It was unclear how the subjects perceive the MVC forces $\hat{F}_i$ and $\hat{F}_i$ of both SA in comparison with both MVC force components $\hat{F}_{[i],j}$ and $\hat{F}_{i,[j]}$ of the related MA. The symbols are the same as in the definition of force levels in subsection 4.4.1. This ratio influences the α-parameters and is calculated for both components of the MA in

$$r_{[\mathrm{i}],\mathrm{j}} = \frac{\hat{F}_{[i],j}}{\hat{F}_i} \quad ; \qquad r_{\mathrm{i},[\mathrm{j}]} = \frac{\hat{F}_{i,[j]}}{\hat{F}_j} \tag{4.20}$$

The measured absolute MVC forces for both SA and MA are given in Fig. 4.17, averaged over the 10 subjects. Figure 4.18 shows all mean ratios obtained by the 10 subjects. If the ratios tend to be smaller than 1, a higher MVC has been applied at execution of the SA. In the majority of these ratios, the subjects execute a higher MVC force at the SA compared to both MVC forces at the MA.
If a linear relation between force and signal strength is assumed, the mean ratio of both force components would be approximately proportional to the α-parameters.

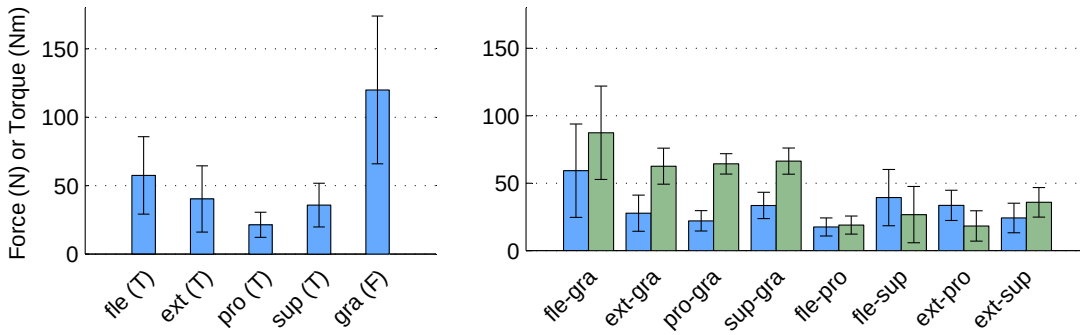

Figure 4.17: Left: MVC forces (F) and torques (T) for SA. Right: MVC forces/torques for MA; blue and green bars represent first and second action in label.

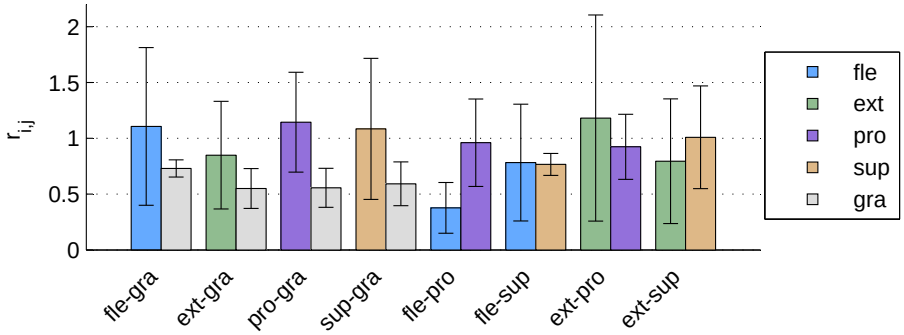

Figure 4.18: Force ratios between MVC forces of MA and SA.

This has been analyzed by the correlation between the MVC force ratios and the alpha parameters. The mean over both MVC force ratios $\bar{r}_{i,j}^{(s)} = \frac{1}{2} \cdot (r_{[i],j}^{(s)} + r_{i,[j]}^{(s)})$ of each MA and each subject s has been taken to correlate it with the respective α-parameters. Figure 4.19 shows this correlation for the sEMG related (left) and FMG related (right) alpha values. The correlation has been determined using *MathWorks MATLAB*'s *corrcoeff* function, which returns a p-value to indicate the significance of each correlation, additionally to the correlation coefficient. A significance level of 5% has been chosen and the coefficient of determination is denoted as R^2. The correlations for sEMG were significant for the MA *ext-gra* ($R^2 = 0.6442, p = 0.0052$), *fle-sup* ($R^2 = 0.5856, p = 0.0010$), *ext-pro* ($R^2 = 0.5907, p = 0.0094$) and *ext-sup* ($R^2 = 0.8404, p = 0.0002$). The correlations for FMG were significant for the MA *fle-gra* ($R^2 = 0.4632, p = 0.0436$), *ext-gra* ($R^2 = 0.7369, p = 0.0031$) and *fle-pro* ($R^2 = 0.4825, p = 0.0378$). In the case of FMG, one outlier (subject 9) has been excluded, which came with two negative alpha values. This might be caused by misinterpreting the stimulus. As in the previous parameter selection, the median has been chosen to get general alpha parameters, the effect of this outlier might be marginal.

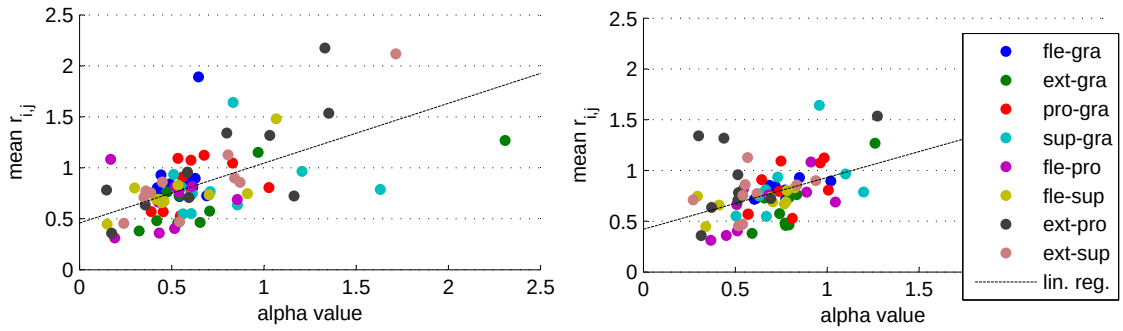

Figure 4.19: Correlation between MVC force ratios and alpha values. Left: sEMG related alphas. Right: FMG related alphas

A correlation analysis over all MA has been also conducted. A vector containing all force ratios from all subjects has been correlated with the respective α-parameters. For both types of α-parameters, the correlation is highly significant (sEMG: $R^2 = 0.341, p < 0.0001$; FMG: $R^2 = 0.193, p < 0.001$). The linear regression line used for this correlation analysis is drawn in each plot.

4.4.7 Cluster Distance between LET and MA

The euclidean distance $\bar{D}$ between the clusters X_{LET} and X_{ij} is marked in Fig. 4.1. The normalized euclidean distance can be used as a measure for the approximation error between the LET cluster and the MA cluster. This measure normalizes the cluster distance $\bar{D}$ by the distance between the rest cluster and the MA cluster, given by

$$\tilde{D}(\bar{X}_{\text{LET}}, \bar{X}_{ij}, \bar{X}_0) = \frac{\left\|\bar{X}_{\text{LET}} - \bar{X}_{ij}\right\|_2}{\left\|\bar{X}_0 - \bar{X}_{ij}\right\|_2} \tag{4.21}$$

For common α-parameters, the mean $\tilde{D}$ over all MA and all subjects is 0.3352. When using the type-related α-parameters for sEMG and FMG, the mean $\tilde{D}$ over all MA and all subjects is 0.2889. This leads to an error reduction of $\frac{0.3352-0.2889}{0.3352} = 13.83\%$ on average, which emphasizes the usage of type-related α-parameters for sEMG and FMG in the following experiment.

4.5 Multiple Activation Online Performance

4.5.1 Experiment Description

In this experiment, three approaches are compared in an online goal reaching task, summarized in Tab. 4.5. In approach *single*, only training data from SA are used. In approach *mult*, training data from both SA and MA are used, which should enable a more precise model for combinations of actions. Approach *LET* uses only SA

data and uses the method LET to add artificial data for combined activations to the training set. Each learning machine is then trained with a different basis of training data, hence showing different performance. The data acquisition system and the hardware are the same as in the previous experiment.
Cross-activations are a major problem in myocontrol. Unwanted activations are triggered by the execution of intended activations. For instance the activation of *sup*, when executing *gra* without any wrist rotation. This cross-activation problem was strongest for the action *sup*, which interferes with all other actions. From a data point of view, the *sup* cluster is often located close to the rest, which easily triggers this action when a subject initialize an activation starting from the rest position. The anatomical point of view could be a deep location of the muscles relevant for *sup*, such that they are hard to detect and hence produce small signal amplitudes on sEMG and FMG sensors. This causes a sensitive behavior of this action in the prediction. As this problem is currently investigated in this research group, it is not targeted in this thesis. To isolate the problem of comparing the performance of *LET* with other approaches from the problem of cross-activations, the following restrictions on the experiment were made.
The SA *sup* and all of its related MA *sup-gra*, *fle-sup* and *ext-sup* were excluded from the experiment. Preliminary online experiments have shown that especially this action causes strong cross-activations and over-sensible behavior of the wrist rotation. To prevent cross-activations during the online performance, the DOF of unwanted activations are locked. For example, when the action *gra* is queried, the DOF of *fle/ext* and *pro/sup* is locked in the prediction. The subject can only actuate *gra* between rest and the full activation. The same accounts for all other SA and MA.

Table 4.5: Approaches for MA online evaluation experiment

Approach	Description of training data	Training set
single	4 × SA data (without *sup*)	$D^{\mathrm{SA}}_{A\setminus\{sup\}}$
mult	4 × SA and 5 × MA data (without *sup*)	$D^{\mathrm{MA}}_{A\setminus\{sup,sup\text{-}gra,fle\text{-}sup,ext\text{-}sup\}}$
LET	4 × SA and 5 × LET data (without *sup*)	$D^{\mathrm{LET}}_{A\setminus\{sup\}}$

It is expected that with *single*, the least number of successful goals can be reached and with *mult*, the largest number of goals is achievable whereas *LET* lies somewhere in between. In an optimal case, *LET* reaches the same or a higher number of successful goals than *mult*, where *LET* would perfectly substitute *mult* as training procedure.
The parameters for each subject, found in the previous experiment are generalized using the median among all subjects, as reported in Tab. 4.4. The median is less outlier sensitive than the mean and regarded as a good choice for the generalization.
The goal reaching task is designed similarly to the previous experiment. A number of four SA and five MA without *sup* and its combinations leads to nine possible actions.

The set of goals is generated for each of the three approaches and at the activation levels of 33%, 66% and 100%, which leads to a number of 81 goals. Each goal is queried twice, resulting in a total number of 162 goals. These goals are permuted as shown in Fig. 4.20. The requirement of the permutation is to equalize the occurrence of the nine actions at three activation levels (a, b, c) and three approaches (A, B, C) over two repetitions (1, 2) in the experiment. The letters a, b, c and A, B, C which represent the activation levels and the approaches are permuted over nine subjects. The order of the nine actions in each activation level is constructed by a 9×9-Latin-square, as it is often used in experimental design [Win62]. An equalized occurrence of the actions and their activation levels throughout the experiment is not guaranteed for a pseudo-random shuffling. This could negatively affect the results as a certain approach could be favored.

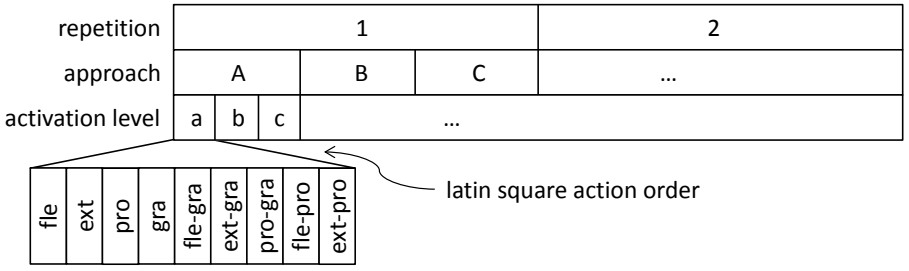

Figure 4.20: Set of targets for the online goal reaching task. Permutations of the approaches, the activation levels and the actions were designed for 9 subjects.

The total number of goals is limited by the time and the physical and mental demand for each subject. The timeout to reach a goal is set to $t_t = 10$ s and the error threshold in all DOFs is set to 0.2. The holding time is again $t_h = 1.5$ s. It is emphasized that these parameters have major influence on the success rate (SR) and the task completion time (TCT) of each subject. They need to be chosen, such that the frustration caused by unreachable goals does not lead to resignation of a subject. For instance, a SR below 50% could cause a drop in motivation where the subject discontinues to reach targets. If the timeout is selected to high, frustration occurs if the subject needs to wait a long period if the goal is unreachable at all. If the parameters are set such that the tasks become too easy, it might be hard to differentiate the performance between the approaches.

4.5.2 Results

The main results are the different SR for each approach and especially the outcome for different sets of goals. The results are separated in three groups in Fig. 4.21. On the left, we can see SR_{all} for all goals including SA and MA, in the middle, SR_{SA} for SA goals and on the right, SR_{MA} for MA activation goals. Horizontal lines without an asterisk on top denote groups in the bar plot, which do not significantly differ

from each other. Horizontal lines with an asterisk on top denote a significant effect between approaches or to an aforementioned group. The significance level is set to be $\alpha = 0.05$.

The SR_{all} shows a significant difference between the approaches. The repeated measures ANOVA results in $F(2, 16) = 36.861$ and $p < 0.0001$. The post-hoc Tuckey-test reveals a significant difference between *single* and both other approaches (both $p < 0.0001$). A significantly better SR_{all} is evident for *mult* and *LET*.

The SR_{SA} for the set of SA goals shows that *single* is significantly worse than *LET* (ANOVA results: $F(2, 16) = 5.925$, $p = 0.0119$). The Tuckey-test shows a value of $p = 0.00183$ between *single* and *LET*. This result is further discussed in section 4.5.3. These results show that the approaches *mult* and *LET* has no negative influence on the training set for performing SA. It is emphasized that the unwanted DOF were locked through the goal reaching of SA.

SR_{MA} is the SR for the set of MA goals. The ANOVA shows a significant difference between the approaches with $F(2, 16) = 34.220$ and $p < 0.0001$. The Tuckey-test reports a significant worse SR for *single* compared to both other approaches (both $p < 0.0001$). As targeted in this experiment, *mult* and *LET* perform significantly better than *single* for MA goals. This shows that *LET* is capable of creating artificial training data for MA, such that there is no significant difference to the approach *mult*, which uses real training data of MA.

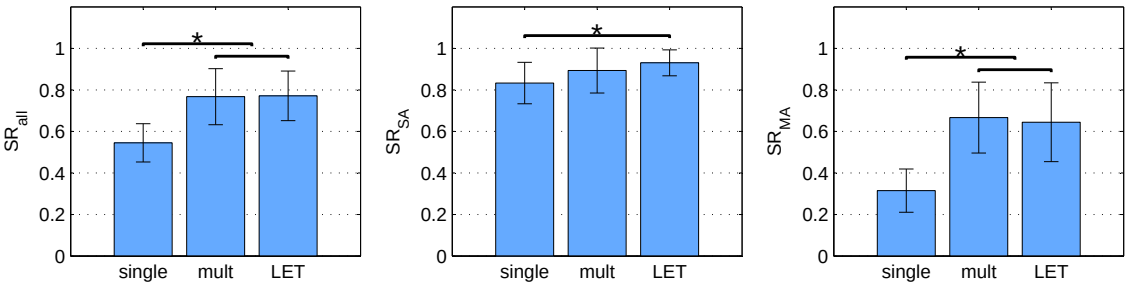

Figure 4.21: Success rates in the multiple activation online performance experiment for all activations (SR_{all}), single activations (SR_{SA}) and multiple activations (SR_{MA}). Comparison of the approaches *single*: trained on SA; *mult*: trained on SA and MA; *LET*: trained on SA and LET data.

Another measure to compare the approaches is the task completion time (TCT), as it was already introduced in the sensor placement experiment in section 2.2. The mean time of reaching all successful goals is shown in Fig. 4.22. For all goals (TCT_{all}), the factor approach is significant for the mean TCT with $F(2, 16) = 36.8619$ and $p < 0.0001$. The Tuckey-test shows that the mean TCT for *single* is significantly smaller than for both other approaches (*single-mult* $p = 0.0002$, *single-LET* $p = 0.0008$). For both other analysis of TCT_{SA} and TCT_{MA}, the factor approach has no significant effect. This difference might be caused as the the analysis is unbalanced

among the approaches, as they achieved different SR. Therefore, the TCT should be always interpreted together with the SR of the approach.

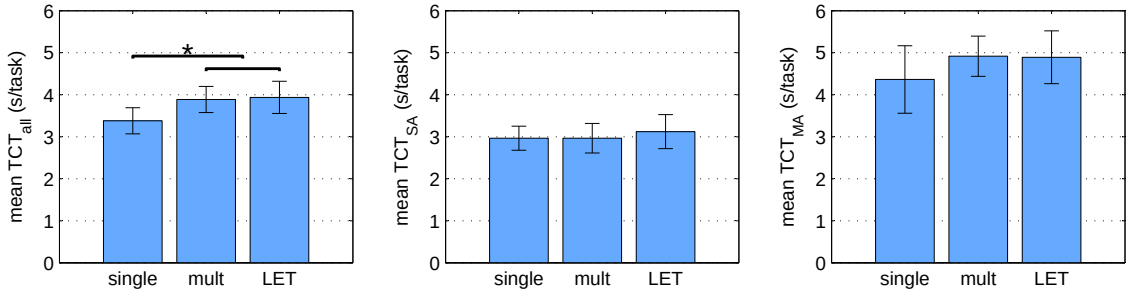

Figure 4.22: Mean task completion time in the online LET experiment for all activations (TCT_{all}), single activations (TCT_{SA}) and multiple activations (TCT_{MA}).

4.5.3 Discussion

Comparing the SR for SA (SR_{SA}), the approach *single* is significantly worse than *LET*. As the *single* LM is trained only on SA, it could be expected that it has a comparable outcome to other approaches, when it is required to reach SA goals. There are two potential explanations why *single* performed worse than *LET*.

First, there is a difference in the probability to trigger the right activation since the unwanted DOF were locked for each specific goal during the goal reaching task. For the four SA (*fle*, *ext*, *pro*, *gra*), there is a probability of $P_{\text{SA}} = \frac{1}{4} = 25\%$ to trigger the right activation for the approach *single*. Adding the fife combined actions (*fle-pro*, *fle-gra*, *ext-pro*, *ext-gra*, *pro-gra*) to the set of SA, a number of 9 actions is obtained. For the approaches *mult* and *LET*, a probability of either $P_{\text{MA,fle,ext}} = \frac{3}{9}$ (for the SA *fle* and *ext*) or a probability of $P_{\text{MA,pro,gra}} = \frac{4}{9}$ (for the SA *pro* and *gra*) is reached. This results in an average probability to trigger the right activation of $P_{\text{MA}} = \frac{1}{4} \cdot (2 \cdot P_{\text{MA,fle,ext}} + 2 \cdot P_{\text{MA,pro,sup}} = \frac{7}{18} = 38.9\%$. If a SA is queried as a goal, the movement in all other DOF is impossible. For the approaches *mult* and *LET*, this can be achieved through execution of either the required SA or any MA, where the required SA is part of. For instance, the goal is to reach *gra*. The subject can perform either *gra*, *fle-gra*, *ext-gra*, *pro-gra* at the required activation level in order to reach *gra*. As the probability is lower for the approach *single*, this could explain a lower SR because the goals can be regarded as more difficult.

As a second explanation, the additional training data of *mult* and *LET* could have a positive influence on the overall regression model. It is possible that a MA cluster related to a SA cluster in the input space solidifies the model prediction for this SA. The adjacent space around the SA cluster is better defined towards the related MA clusters instead of leaving a larger undefined input space in the approach *single*. The undefined areas in the input space between the training clusters get smaller. This

could prevent the regression model from adverse behavior during the prediction for sensor values which lie in these undefined areas.

So far, there is no clear finding why only *LET* has a significantly higher SR than *single* but *mult* has not. The training data acquisition has a strong effect on the SR of the experiment. The experimenter observed that some subjects are not aware of the right execution of the MA to be trained. As a reminder, there occurs training only on the rest position and full activations. When a subject is instructed to execute a certain MA, it is indicated by the visual stimulus on a screen in front of the subject. The experimenter executes the MA again with the left hand after it was shown by the visual stimulus and explains how to actuate both DOF of the required MA. If the subject signalizes the right configuration of her hand, the experimenter captures the training data. Some subjects executed one of the DOF of a MA in the opposite direction because they misinterpreted the visual stimulus. This was observed by the experimenter when looking at the hand of the subject and through the force levels for each DOF. These levels were used just for feedback to the experimenter and configured as in the previous experiment of the force related data acquisition 4.4. If the experimenter was aware of a misinterpretation by the subject, the required MA was shown again by the hand of the experimenter. If the subject insisted on executing the right MA, the experimenter captured the data. This possibly introduces another factor into the experiment, as some subjects are more experienced than others due to their multiple participation in previous sEMG or FMG data acquisition experiments. This factor is so far not analyzed but experienced subjects noted their participation in the pre-experiment questionnaire.

The time saving in the training is one of the two important achievement of LET. In this experimental design, four SA and five MA were trained. For the method *LET*, which makes MA training unnecessary, the training time can be reduced to $\frac{4}{9}$ of the original time, which is an acceleration of 56%.

LET relies only on training data of SA, which is the second important achievement. Since amputees have only a marginal imagination of the simultaneous actuation of more than one DOF in their residual limb, this is a mandatory property.

The same three approaches were also tested outside of the mechanical test setup. The user performed the experiment with the elbow on the table, subsequently called table test. An upright forearm position has been used as in the sensor placement experiment in 2.2. This was done to compare the prediction performance with the original setup. The outcome of this test was similar to the experiment and the prediction was usable. An experimental comparison involving a variety of subjects has not been conducted due to time reasons. The overall performance on the table test might be better as the user can freely move the hand which gives useful visual feedback and maybe a better control experience. Nevertheless, the mechanical test setup might be closer to an amputee scenario with blocked hand and less visual feedback.

4.6 Conclusion

The experimental results have shown that a LM, provided with LET data can compete in the SR as well as in the TCT with a LM, trained on the real MA data. The use of LET comes with three advantages.
First, the training time involving MA can be accelerated by 56% in this case.
Second, a problematic training data acquisition for simultaneous activations can be bypassed. Since the approach *LET* removes the necessity to train MA, it can be quite useful for amputees. They often have only a marginal imagination of how to actuate more than one DOF at a time in their residual limb.
Third, LET approximates MA clusters correctly between SA clusters in the input space and prevents from misinterpreting a MA stimulus. On the other hand, misinterpretations are possible for each MA trained with approach *mult*. The experiment has shown that *LET* performed slightly better in SR_{SA}, which is assumed to be an effect of proper MA cluster placement between the SA clusters in the input space.
Finally, training a LM only with SA results in a significantly worse performance especially in the case of MA goals. This shows that it is possible to improve the prediction for MA goals in simultaneous and proportional (s/p) control with a simple data enhancement method, called LET.

Chapter 5

Discussion

In this work, a comparison between the signal modalities of sEMG and FMG has been performed using the same conditions for each approach. This builds up on the assessment in [CRVC16]. The number of sensors was kept equal for each approach and different sensor placements were compared. The different placements has been evaluated in an offline experiment over 10 subjects where both sEMG and FMG sensor channels have been stacked in the same input space of a LM (*STA*). No significant effect has been found. This is a good basis for the comparison of approaches, where different sensors need to be selected.

In this offline experiment, the performance between each single modality LM of sEMG and FMG has been compared to two multi-modal machine learning approaches. The best performance could be achieved with *STA* and FMG signals. The LM using sEMG performed significantly worse, which is presumably caused by the noise and instability of this signal type.

The comparison of different approaches has been further evaluated in an online experiment with 12 subjects, which extends the work in [NEC17]. Same as in the offline experiment, the best prediction results has been achieved with *STA* and FMG signals whereas the remaining two approaches performed significantly worse. This emphasizes that a combination of the multi-modal sensor signals has the potential to perform better than one single signal type.

As a goal of this work, the multi-modal machine learning has been further exploited. The Kalman filter has been considered to test a probabilistic fusion approach, where different sensor channels or output DOF can have a defined confidence. The filter has been parameterized with confidences based on the previous experiment, derived from the SR on each DOF. The parameterization based on the SR of the previous experiment is only one possible source of information. The filter could be also adapted by e.g. online noise estimation or derived anatomical properties related to the produces sensor signals. Through the restriction that an inverted mapping between sensor input and prediction is not available to design an observation model, a simplified solution to directly fuse the output of two sensor type related LM was further exploited. In a single user study, the SR of the KF compared to *STA* was

lower by 20%. It is assumed that modeling the uncertainty in discrete time domain does not properly relate to the influence from the muscular activity or joint position which are rather time invariant. Despite the worse SR, a probabilistic approach enables a confidence weighting of different signals responsible for the prediction. If changing signal characteristics are detectable online, they could be handled with an adaptive filter design. In contrast, an adaptive behavior of the RR-RFF algorithm is so far not possible except for the incremental update feature of this algorithm.

For the LET related experiments, a test setup has been designed which fixates the wrist joint but allows independent finger movement at the same time. This is different from [YYK+15], where a bar need to be grasped during measurement of wrist forces. The fixated wrist setup creates similarities to a transradial amputated forearm. The movement of muscles in the tissue is minimized since the tendons of the wrist joint allow only restricted movement. As an empirical data acquisition from amputees is hard to achieve since there is only a limited number of test persons, this setup enables the data acquisition of healthy subjects.

The software has been extended to read from both F/T sensor and to receive pose information as well as the end-effector wrench of the employed robot. Further inputs are the pose of both support elements of the test setup as well as the elbow angle of the subject. In the conducted experiments, the elbow angle was unrestricted in a certain range. If the subject was aware of the elbow angle changes, he or she could use this additional DOF to influence the signals on the forearm. Since the elbow angle affects the generation of the training signals and the model prediction, this effect need to be further assessed.

Training data from 10 healthy subjects at 40% of their MVC of each action has been captured to obtain initial data for LET. The LET strategy has been optimized by removing the offset of the rest cluster from the coordinate origin of the sensor input space. Further, LET has been applied to each sensor modality independently. This reduced the approximation error of the LET cluster by 13.83% compared to applying LET on the whole dataset.

The LET parameters have been generalized using the median over all subjects, as the rate of misinterpreted stimuli was assumed to be high due to less experienced subjects. Thereafter, the same parameter set for all future subjects can be used. The subsequent online experiment with nine subjects evaluated LET using these generalized parameters. The LM using LET data performed with similar performance as the LM provided with both SA and MA data. In this experiment, LET could successfully substitute MA training data using a multi-modal sensory input. However, more experienced subjects could cause a lower rate of misinterpretations during training and hence MA data could still outperform LET.

The human factor has a strong influence on the performance of the whole system besides the ML algorithm. This starts with the training data acquisition and later on affects the online control. A big difference in the conducted experiments could be observed between inexperienced subjects, which may participate the first time in such experiments and experienced subjects, which may even work in this research

topic and commonly use the hardware. All of the experiments included a variety of at least nine subjects. The gained experimental results are hence averaged over the experience level of their subjects. It can be assumed that a frequent prosthesis user has a good chance to improve his or her initial control capabilities on such systems.

Chapter 6

Conclusions

6.1 Conclusion

The results of the initial offline experiment enabled a fair comparison of different approaches using the multi-modal sensory input. We have shown that the placement of the two sensor types has no effect on the prediction accuracy which is an important finding for future experiments. Complicated sensor placement strategies can be avoided when placing sEMG and FMG sensors on the forearm.
Using these results enabled a fair online comparison of two different fusion approaches and both signal inputs independently. With the results that a combination of signals in the *STA* approach had the same outcome as using FMG sensors only, a proper fusion of both signals can even lead to a better performance.
In the fusion approach using Kalman filtering, we have shown that a probabilistic approach can be used to fuse the output of two signal type related learning machines. The approach performed with a lower SR than the best regression based fusion approach *STA* but enables the online adaption of the signal fusion and could hence handle changing signals characteristics.
The designed test setup enables the recording of training data at a fixed wrist position with force/torque measurement of the selected DOF. This facilitates the data acquisition from healthy subjects with a strong relation to the signal characteristics of amputees. The strategy of LET could be successfully applied to the multi-modal training set of different subjects using this novel test setup. The online evaluation has shown that the LET parameters could be effectively generalized for several subjects. The performance of LET even reached the outcome of a model, which was provided with the available training data of SA and MA. We showed that LET can fully substitute MA training based on SA training only. With the hand and wrist actions from this experiment, more than half of the training time can be saved. Since the number of possible MA related to SA raises exponentially, the time saving is even greater for an increased number of actions.
A further advantage of LET is that misinterpreted stimuli for MA, which negatively affect the dataset, are completely avoided. Although misinterpretations usually do

not occur at SA training, LET outperformed all other models in the experiment. It is concluded that the proper LET cluster placement positively affects also the regression model for the execution of SA.
Amputees using this strategy can train a simultaneous and proportional control system without the requirement to execute MA during training time. The found LET parameters can be transferred to amputees to evaluate this powerful strategy in further online experiments using a multi-modal input.

6.2 Future Work

Since LET is not related to a specific machine learning method, its usage can be further exploited with other machine learning methods and fusion approaches for the multi-modal input.
The collected data in different setups include elbow angle information and hand pose information in accordance with sEMG and FMG sensor signals at a variety of wrist and hand actions. All this information can be used for future analysis of the elbow angle or forearm pose and their effect on the training data and model prediction.
The current software *interactiveMyocontrol* should be extended by a visual data selection tree, which enables the deletion or repeated recording of certain actions. This helps to exclude data which is evidently wrong, when the stimulus has been misinterpreted or the subject was not focused. Furthermore, mathematical metrics could evaluate the current recording at runtime and signalize, if it fits to previous repetitions or if it has poor quality.
As one focus of LET is to accelerate the training time, the data acquisition process could be further accelerated for daily life situations. Instead of the visual stimulus screen, which is required for inexperienced subjects, a minimized visual stimulus in form of a functional display, an audio stimulus or even a haptic stimulus could be used. With and intuitive operation of the prosthetic device, the user could also self-determine when he or she wants to record a certain action.
The selected hand and wrist actions were chosen based on the previous work at DLR, in accordance to current research interests and possibilities. The two wrist DOF are beneficial in activities of daily life for object approaching and manipulation after using the power grasp. If a more dexterous grasp type is required, the amputee probably executes it anyway with his or her intact hand. Notwithstanding, a more dexterous and responsive control of prostheses need to be achieved to ease this activities. Therefore, an improved hardware capable of these functions needs to be developed.
Problems of unwanted activations of DOF other than the desired one already occurred in the preceding work using only sEMG sensors. This effect is not only caused by the ML model and for instance also occurs with linear regression. The action *sup* has been also not targeted in [NC15] as this action interferes strongest with the other considered actions. So far, the combination of sEMG and FMG in the

evaluated fusion approaches of this work could not prevent this problem. Exploring the problems of unwanted activations in simultaneous and proportional control is aim of future research.

Appendix A

Software

A.1 Device Drivers

The following modules has been implemented as device drivers in the existing software framework of *interactiveMyocontrol*. They interface different sensors, are in charge of data preprocessing or connect to UDP sockets in order to collect data from external systems. All acquired data is dumped to disk to allow further analysis after an experiment.

A.1.1 Robot: UDP Listener

The UDP telegrams come from the left KUKA LWR controller of the HUG platform. They include the Cartesian pose and the force/torque values of the sensors located at the tool center point (TCP).

The UDP telegram listener is implemented in *ddUDPlistener*. The format of a telegram is a number of double values, where each value is defined through blocks of 8 byte. The following table describes the received values.

Pos.	Description
0	[4×3] matrix: affine transformation: TCP → world_frame; consisting of:
⋮	[3×3] rotation matrix
11	[1×3] translation (x,y,z)
12	6 DOF force/torque sensor on TCP; consisting of:
⋮	3 × force (F_x, F_y, F_z)
17	3 × torque (T_x, T_y, T_z)

A.1.2 Visual Tracking System: UDP Listener

The UDP telegrams come from the visual tracking system of the HUG platform. The poses of both segments of the LET test setup and the transformation between these poses are transmitted. Further, the axis-angle representation of the elbow hinge between these segments is obtained. This angle corresponds to the subject's elbow angle.
The UDP telegram listener is implemented in class *ddUDPlistener*. The format of a telegram is a number of double values, where each value is defined through blocks of 8 byte. The following table describes the received values.

Pos.	Description
0	[4×3] matrix: affine transformation: segment_1 → world_frame; consisting of:
⋮	[3×3] rotation matrix
11	[1×3] translation (x,y,z)
12	[4×3] matrix: affine transformation: segment_2 → world_frame; consisting of:
⋮	[3×3] rotation matrix
23	[1×3] translation (x,y,z)
24	[4×3] matrix: affine transformation: segment_1 → segment_2; consisting of:
⋮	[3×3] rotation matrix
35	[1×3] translation (x,y,z)
36	angle between segment_1 and segment_2
37	axis vector related to above angle
⋮	[1×3] unit vector indicating the direction of rotation axis relative to world_frame
39	

A.1.3 ATI Mini45 F/T sensor

The ATI Mini45 force/torque sensor is interfaced through analogue signals, read by a Native Instruments data acquisition card (NI-DAQ). The data is then sent to the computer via an Ethernet connection. The NI-DAQ device driver is implemented in class *addNIDAQ*. The raw sensor signals need to be pre-processed to obtain physical force and torque values, using a calibration matrix delivered with the sensor. The pre-processing is implemented in class *addFTsensor*, provided with this calibration matrix. F denotes a force whereas T denotes a torque around this axis.

A.1.4 Space Control OFTS F/T sensor

This optical 6 DOF force torque sensor is interfaced via RS232, with a simple polling mode implemented in class *spddOFTS*. F denotes a force whereas T denotes a torque around this axis.

Channel	Description
0	F_x
1	F_y
2	F_z
3	T_x
4	T_y
5	T_z

Channel	Description
0	T_x
1	T_y
2	T_z
3	F_x
4	F_y
5	F_z

A.1.5 NI-DAQ for ATI Mini45

The device driver for the Native Instruments data acquisition card is implemented in *addNIDAQ*. The card is configured by the channel string `dev1/ai1:6`, which sets the device name to `dev1` and enables 6 analog inputs related to the 6 DOF of the interfaced F/T sensor. All channel signals come without calibration. The software channels are defined as followed:

Channel	Description
0	raw F_x
1	raw F_y
2	raw F_z
3	raw T_x
4	raw T_y
5	raw T_z

A.2 Configuration File

The configuration file with the ending `*.config` used for the LET evaluation has been extended by the following key-value pairs:

A.3 Machine Learning Parameter File

The files with the ending `*.ml` parametrizes learning machines with their hyper-parameters. In the case of Ride Regression with Random Fourier Features (RR-RFF), the data structure for the parameter σ has been adapted. Previously, only a

Key	Description
`"LETsingleAlphas"`	assigns an alpha parameter to a combination name, e.g. `"LET_wr flexion power,0.595770;LET_wr extension power,0.612140"`
`"signalReaderList"`	a list of signal readers to be activated, e.g. `"wbt nidaq ftsensor ofts"`
`"calibrationMatrix"`	the calibration matrix for the ATI Mini45 sensor which transforms raw sensor readings into forces/torques
`"nidaqChannelString"`	configuration of the Native Instrument data acquisition card (NI-DAQ), e.g `"dev1/ai1:6"`, providing a device name (`dev1`) and the number of analog inputs (`ai1:6`)
`"learningMode`i`"`	configures the learning machine with number i in the following modes: `"single"`: train only on single activations; `"all"`: train on single and multiple activations; `"let"`: train only on single activations and LET data

single hyper-parameter could be defined for the whole input space. Now, a vector of σ values can be defined to relate a value to each sensor, which is then parsed in the class *Learning*. This is used to configure σ values for different sensor types, e.g. sEMG and FMG. Given an example for 5 sEMG and 5 FMG sensors with different σ parameters:

```
<sigma>0.7 0.7 0.7 0.7 0.7 0.5 0.5 0.5 0.5 0.5</sigma>
```

List of Figures

Acronyms and Notations

ANN Artificial Neural Network

DLR Deutsches Zentrum für Luft- und Raumfahrt

DOF Degree of Freedom

DOFs Degrees of Freedom

ELM Etreme Learning Machine

EMG Electro-Myography

ext wrist extension

F/T force-torque

fle wrist flexion

FMG Force-Myography

FSR Force Sensing Resistor

GLR Generalized Linear Regression

gra power grasp

GRNN Generalized Regression Neural Network

HRI Human-Robot Interaction

IGT In-Goal Time

KF Kalman Filter

KRR Kernel Ridge Regression

LDA Linear Discriminant Analysis

LET Linearly Enhanced Training

LR Linear Regression

M. Musculus

MA Multiple Activation

MVC Maximum Voluntary Contraction

NMF Non-negative Matrix Factorization

NN Neural Network

OSELM Online Sequential Extreme Learning Machine

p proportional

pro wrist pronation

RBF Radial Basis Function

res rest position

RR Ridge Regression

RR-RFF Ridge Regression with Random Fourier Features

s/p simultaneous and proportional

s simultaneous

SA Single Activation

sEMG surface Electro-Myography

SG Successful Goals

SGS Strain Gauge Sensor

SR Success Rate

sup wrist supination

SVM Support Vector Machine

SVR Support Vector Regression

SVR Support Vector Regression

TCT Task Completion Time

TDANN Time Delayed Artificial Neural Network

UG Unsuccessful Goals

URG Unsuccessful Reachable Goals

Bibliography

[AGK+15] Manfredo Atzori, Arjan Gijsberts, Ilja Kuzborskij, Simone Elsig, Anne-Gabrielle Mittaz Hager, Olivier Deriaz, Claudio Castellini, Henning Müller, and Barbara Caputo. Characterization of a benchmark database for myoelectric movement classification. *IEEE Transactions on Neural Systems and Rehabilitation Engineering*, 23(1):73–83, 2015.

[BC07a] Elaine Biddiss and Tom Chau. Upper-limb prosthetics: critical factors in device abandonment. *American journal of physical medicine & rehabilitation*, 86(12):977–987, 2007.

[BC07b] Elaine A Biddiss and Tom T Chau. Upper limb prosthesis use and abandonment: a survey of the last 25 years. *Prosthetics and orthotics international*, 31(3):236–257, 2007.

[BC08] Elaine A Biddiss and Tom T Chau. Multivariate prediction of upper limb prosthesis acceptance or rejection. *Disability and Rehabilitation: Assistive Technology*, 3(4):181–192, 2008.

[BGK+11] Rainer Bischoff, Tim Guhl, Johannes Kurth, Günther Schreiber, Herman Bruynicks, and Smits Ruben. Tool handling system and method for manipulating workpieces by means of cooperating manipulators, 2011.

[CBNvdS16] C Castellini, RM Bongers, M Nowak, and CK van der Sluis. Upper-limb prosthetic myocontrol: Two recommendations. *Frontiers in neuroscience*, 9:496, 2016.

[CCM+16] Erina Cho, Richard Chen, Lukas-Karim Merhi, Zhen Xiao, Brittany Pousett, and Carlo Menon. Force myography to control robotic upper extremity prostheses: a feasibility study. *Frontiers in bioengineering and biotechnology*, 4(-):–, 2016.

[CN14] Claudio Castellini and Markus Nowak. Emg-based prediction of multi-dof activations using single-dof training: a preliminary result. In *Proc. of Myoelectric Control Symposium (MEC)*, pages 45–49, 2014.

[CR14] Claudio Castellini and Vikram Ravindra. A wearable low-cost device based upon force-sensing resistors to detect single-finger forces. In *Biomedical Robotics and Biomechatronics (2014 5th IEEE RAS & EMBS International Conference on*, pages 199–203. IEEE, 2014.

[CRVC16] Mathilde Connan, Eduardo Ruiz Ramírez, Bernhard Vodermayer, and Claudio Castellini. Assessment of a wearable force-and electromyography device and comparison of the related signals for myocontrol. *Frontiers in Neurorobotics*, 10(-):–, 2016.

[EP09] N. Jiang *, K. B. Englehart, and P. A. Parker. Extracting simultaneous and proportional neural control information for multiple-dof prostheses from the surface electromyographic signal. *IEEE Transactions on Biomedical Engineering*, 56(4):1070–1080, April 2009. doi:10.1109/TBME.2008.2007967.

[EPPS84] Harry B Evans, Zuzhan Pan, Philip A Parker, and Robert N Scott. Signal processing for proportional myoelectric control. *IEEE transactions on biomedical engineering*, -(2):207–211, 1984.

[EYkA16] A. Ehrampoosh, A. Yousefi-koma, and M. Ayati. Development of myoelectric interface based on pattern recognition and regression based models. In *2016 Artificial Intelligence and Robotics (IRANOPEN)*, pages 145–150, April 2016. doi:10.1109/RIOS.2016.7529505.

[FJM+16] A. Ferrane, X. Jiang, L. Maiolo, A. Pecora, L. Colace, and C. Menon. A fabric-based wearable band for hand gesture recognition based on filament strain sensors: A preliminary investigation. In *2016 IEEE Healthcare Innovation Point-Of-Care Technologies Conference (HI-POCT)*, pages 113–116, Nov 2016. doi:10.1109/HIC.2016.7797710.

[FWS+15] E. Fujiwara, Y. T. Wu, M. F. M. Santos, E. A. Schenkel, and C. K. Suzuki. Development of an optical fiber fmg sensor for the assessment of hand movements and forces. In *2015 IEEE International Conference on Mechatronics (ICM)*, pages 176–181, March 2015. doi:10.1109/ICMECH.2015.7083969.

[GBSG+14] Arjan Gijsberts, Rashida Bohra, David Sierra González, Alexander Werner, Markus Nowak, Barbara Caputo, Maximo Alejandro Roa, and Claudio Castellini. Stable myoelectric control of a hand prosthesis using non-linear incremental learning. *Frontiers in neurorobotics*, 8:8, 2014.

[GKAM15] P. Ghaderi, S. Karimimehr, M. E. Andani, and H. R. Marateb. Hand kinematics estimation to control prosthetic devices: a nonlinear approach for simultaneous and proportional estimation of 15 dofs. In *2015 22nd Iranian Conference on Biomedical Engineering (ICBME)*, pages 233–238, Nov 2015. doi:10.1109/ICBME.2015.7404148.

[GM11] Arjan Gijsberts and Giorgio Metta. Incremental learning of robot dynamics using random features. In *Robotics and Automation (ICRA), 2011 IEEE International Conference on*, pages 951–956. IEEE, 2011.

[HPS93] Bernard Hudgins, Philip Parker, and Robert N Scott. A new strategy for multifunction myoelectric control. *IEEE Transactions on Biomedical Engineering*, 40(1):82–94, 1993.

[JRV+14] N. Jiang, H. Rehbaum, I. Vujaklija, B. Graimann, and D. Farina. Intuitive, online, simultaneous, and proportional myoelectric control over two degrees-of-freedom in upper limb amputees. *IEEE Transactions on Neural Systems and Rehabilitation Engineering*, 22(3):501–510, May 2014. doi:10.1109/TNSRE.2013.2278411.

[JVR+14] N. Jiang, I. Vujaklija, H. Rehbaum, B. Graimann, and D. Farina. Is accurate mapping of emg signals on kinematics needed for precise online myoelectric control? *IEEE Transactions on Neural Systems and Rehabilitation Engineering*, 22(3):549–558, May 2014. doi:10.1109/TNSRE.2013.2287383.

[KJM16] Anita Kadkhodayan, Xianta Jiang, and Carlo Menon. Continuous prediction of finger movements using force myography. *Journal of Medical and Biological Engineering*, 36(4):594–604, 2016. URL: http://dx.doi.org/10.1007/s40846-016-0151-y, doi:10.1007/s40846-016-0151-y.

[KVN15] A. Krasoulis, S. Vijayakumar, and K. Nazarpour. Evaluation of regression methods for the continuous decoding of finger movement from surface emg and accelerometry. In *2015 7th International IEEE/EMBS Conference on Neural Engineering (NER)*, pages 631–634, April 2015. doi:10.1109/NER.2015.7146702.

[MAB+10] Roberto Merletti, Matteo Aventaggiato, Alberto Botter, Ales Holobar, Hamid Marateb, and Taian MM Vieira. Advances in surface emg: recent progress in detection and processing techniques. *Critical Reviews(TM) in Biomedical Engineering*, 38(4), 2010.

[MHH86] SG Millstein, H Heger, and GA Hunter. Prosthetic use in adult upper limb amputees: a comparison of the body powered and elec-

trically powered prostheses. *Prosthetics and orthotics international*, 10(1):27–34, 1986.

[MTM15] J. Ma, N. V. Thakor, and F. Matsuno. Hand and wrist movement control of myoelectric prosthesis based on synergy. *IEEE Transactions on Human-Machine Systems*, 45(1):74–83, Feb 2015. doi:10.1109/THMS.2014.2358634.

[NAC16] Markus Nowak, Beatrice Aretz, and Claudio Castellini. Wrist and grasp myocontrol: Online validation in a goal-reaching task. In *Robot and Human Interactive Communication (RO-MAN), 2016 25th IEEE International Symposium on*, pages 132–137. IEEE, 2016.

[NC15] Markus Nowak and Claudio Castellini. Wrist and grasp myocontrol: Simplifying the training phase. In *2015 IEEE International Conference on Rehabilitation Robotics (ICORR)*, pages 339–344. IEEE, 2015.

[NC16] Markus Nowak and Claudio Castellini. The let procedure for prosthetic myocontrol: Towards multi-dof control using single-dof activations. *PloS one*, 11(9):e0161678, 2016.

[NCWA12] Jon W Nicholas, Russel J Corvese, Charles Woolley, and Thomas J Armstrong. Quantification of hand grasp force using a pressure mapping system. *Work*, 41(Supplement 1):605–612, 2012.

[NEC17] Markus Nowak, Thomas Eiband, and Claudio Castellini. Multimodal myocontrol: testing combined force- and electromyography. In *IEEE International Conference on Rehabilitation Robotics (ICORR)*, 2017.

[NHJ+09] Johnny LG Nielsen, Steffen Holmgaard, Ning Jiang, Kevin Englehart, Dario Farina, and Philip Parker. Enhanced emg signal processing for simultaneous and proportional myoelectric control. In *2009 Annual International Conference of the IEEE Engineering in Medicine and Biology Society*, pages 4335–4338. IEEE, 2009.

[NTIS15] Jimson Ngeo, Tomoya Tamei, Kazushi Ikeda, and Tomohiro Shibata. Modeling dynamic high-dof finger postures from surface emg using nonlinear synergies in latent space representation. In *2015 37th Annual International Conference of the IEEE Engineering in Medicine and Biology Society (EMBC)*, pages 2095–2098. IEEE, 2015.

[OG02] Leonard W O'sullivan and Timothy J Gallwey. Upper-limb surface electro-myography at maximum supination and pronation torques: the effect of elbow and forearm angle. *Journal of Electromyography and Kinesiology*, 12(4):275–285, 2002.

[ØLF+12] Kristin Østlie, Ingrid Marie Lesjø, Rosemary Joy Franklin, Beate Garfelt, Ola Hunsbeth Skjeldal, and Per Magnus. Prosthesis use in adult acquired major upper-limb amputees: patterns of wear, prosthetic skills and the actual use of prostheses in activities of daily life. *Disability and Rehabilitation: Assistive Technology*, 7(6):479–493, 2012.

[PS85] Philip A Parker and Robert N Scott. Myoelectric control of prostheses. *Critical reviews in biomedical engineering*, 13(4):283–310, 1985.

[PSL16] K. H. Park, H. I. Suk, and S. W. Lee. Position-independent decoding of movement intention for proportional myoelectric interfaces. *IEEE Transactions on Neural Systems and Rehabilitation Engineering*, 24(9):928–939, Sept 2016. doi:10.1109/TNSRE.2015.2481461.

[PVdDVL+99] K Postema, V Van der Donk, J Van Limbeek, R AJ Rijken, and MJ Poelma. Prosthesis rejection in children with a unilateral congenital arm defect. *Clinical rehabilitation*, 13(3):243–249, 1999.

[RCCK16] M. Rasouli, K. Chellamuthu, J. J. Cabibihan, and S. L. Kukreja. Towards enhanced control of upper prosthetic limbs: A force-myographic approach. In *2016 6th IEEE International Conference on Biomedical Robotics and Biomechatronics (BioRob)*, pages 232–236, June 2016. doi:10.1109/BIOROB.2016.7523629.

[RGL+15] M. Rasouli, R. Ghosh, W. W. Lee, N. V. Thakor, and S. Kukreja. Stable force-myographic control of a prosthetic hand using incremental learning. In *2015 37th Annual International Conference of the IEEE Engineering in Medicine and Biology Society (EMBC)*, pages 4828–4831, Aug 2015. doi:10.1109/EMBC.2015.7319474.

[RN93] S. Radhakrishnan and M. Nagaravindra. Analysis of hand forces in health and disease during maximum isometric grasping of cylinders. *Medical and Biological Engineering and Computing*, 31(4):372–376, 1993. URL: http://dx.doi.org/10.1007/BF02446690, doi:10.1007/BF02446690.

[RR16] Eduardo Ruiz Ramírez. Control of a hand prosthesis using mixed electromyography and pressure sensing. Master's thesis, Universitat Politècnica de Catalunya, 2016.

[RSE16] Ashkan Radmand, Erik Scheme, and Kevin Englehart. High-density force myography: A possible alternative for upper-limb prosthetic control. *Journal of Rehabilitation Research & Development*, 53(4):443–457, 2016.

[SHH+16] Mikel Sagardia, Thomas Hulin, Katharina Hertkorn, Philipp Kremer, and Simon Schätzle. A platform for bimanual virtual assembly training with haptic feedback in large multi-object environments. In *Proceedings of the 22nd ACM Conference on Virtual Reality Software and Technology*, pages 153–162. ACM, 2016.

[SM16] M. Sakr and C. Menon. On the estimation of isometric wrist/forearm torque about three axes using force myography. In *2016 6th IEEE International Conference on Biomedical Robotics and Biomechatronics (BioRob)*, pages 827–832, June 2016. doi:10.1109/BIOROB.2016.7523730.

[SP88] RN Scott and PA Parker. Myoelectric prostheses: state of the art. *Journal of medical engineering & technology*, 12(4):143–151, 1988.

[SPP15] Joe Sanford, Rita Patterson, and Dan Popa. Surface emg and intrasocket force measurement to control a prosthetic device. In *SPIE Sensing Technology+ Applications*, pages 94940C–94940C. International Society for Optics and Photonics, 2015.

[SSS11] E Schulte, U Schumacher, and M Schünke. Prometheus-allgemeine anatomie und bewegungssystem, 2011.

[Win62] Benjamin J Winer. *Statistical principles in experimental design*, chapter Latin squares and related designs, pages 514–577. McGraw-Hill Book Company, 1962.

[Y+16] Oguz Yetkin et al. *Intuitive Human Robot Interfaces for Upper Limb Prosthetics*. PhD thesis, University of Texas, 2016.

[YMGY16] H. K. Yap, A. Mao, J. C. H. Goh, and C. H. Yeow. Design of a wearable fmg sensing system for user intent detection during hand rehabilitation with a soft robotic glove. In *2016 6th IEEE International Conference on Biomedical Robotics and Biomechatronics (BioRob)*, pages 781–786, June 2016. doi:10.1109/BIOROB.2016.7523722.

[YYK+15] Yuichi Yoshii, Hiroshi Yuine, Ohashi Kazuki, Wen-lin Tung, and Tomoo Ishii. Measurement of wrist flexion and extension torques in different forearm positions. *Biomedical engineering online*, 14(1):115, 2015.

[ZO14] Kevin J Zuo and Jaret L Olson. The evolution of functional hand replacement: From iron prostheses to hand transplantation. *Plastic Surgery*, 22(1):44, 2014.